

**ROCK FRACTURING & MINE TO MILL OPTIMIZATION**

by

**Kwangmin Kim**

---

A Dissertation Submitted to the Faculty of the

**DEPARTMENT OF MINING AND GEOLOGICAL ENGINEERING**

In Partial Fulfillment of the Requirements  
For the Degree of

**DOCTOR OF PHILOSOPHY**

In the Graduate College

**THE UNIVERSITY OF ARIZONA**

**2012**

UMI Number: 3523976

All rights reserved

INFORMATION TO ALL USERS

The quality of this reproduction is dependent on the quality of the copy submitted.

In the unlikely event that the author did not send a complete manuscript and there are missing pages, these will be noted. Also, if material had to be removed, a note will indicate the deletion.



UMI 3523976

Copyright 2012 by ProQuest LLC.

All rights reserved. This edition of the work is protected against unauthorized copying under Title 17, United States Code.



ProQuest LLC.  
789 East Eisenhower Parkway  
P.O. Box 1346  
Ann Arbor, MI 48106 - 1346

THE UNIVERSITY OF ARIZONA  
GRADUATE COLLEGE

As members of the Dissertation Committee, we certify that we have read the dissertation prepared by Kwangmin Kim entitled Rock Fracturing & Mine to Mill Optimization and recommend that it be accepted as fulfilling the dissertation requirement for the Degree of Doctor of Philosophy

\_\_\_\_ Date: 07/17/2012  
John Kemeny

\_\_\_\_ Date: 07/17/2012  
Moe Momayez

\_\_\_\_ Date: 07/17/2012  
Jinhong Zhang

\_\_\_\_ Date: 07/17/2012  
Ted Wilson

Final approval and acceptance of this dissertation is contingent upon the candidate's submission of the final copies of the dissertation to the Graduate College.

I hereby certify that I have read this dissertation prepared under my direction and recommend that it be accepted as fulfilling the dissertation requirement.

\_\_\_\_ Date: 07/17/2012  
Dissertation Director: John Kemeny

#### STATEMENT BY AUTHOR

This dissertation has been submitted in partial fulfillment of requirements for an advanced degree at the University of Arizona and is deposited in the University Library to be made available to borrowers under rules of the Library.

Brief quotations from this dissertation are allowable without special permission, provided that accurate acknowledgment of source is made. Requests for permission for extended quotation from or reproduction of this manuscript in whole or in part may be granted by the author.

SIGNED: Kwangmin Kim

## **ACKNOWLEDGEMENTS**

First, I would like to express my deepest gratitude to my advisor, Dr. John Kemeny, for his excellent guidance, caring, patience, and encouragement during my graduate studies. Dr. Kemeny, I owe you so much. You have given so much of yourself to help me succeed. In my future academic path, I only hope that I can be half the advisor that you have been to me.

I would also like to express my thanks to Mr. Hal Galbraith, the previous mine manager in ASARCO, for his support, great advice, and encouragement. Hal, you have been my mentor and my friend. Thank you again for all of your help and your confidence in me.

I wish to extend thanks to the rest of my dissertation committee, Dr. Jinhong Zhang, Dr. Moe Momayez, and Dr. Ted Wilson, for their valuable advice and comments on the dissertation. In particular, Dr. Jinhong, I appreciate your concern, support and help.

I would also like to thank my parents, my elder brother, and my younger sister. Without your unending support and love from childhood to now, I never would have made it through this process or any of the tough times in my life.

Finally, I thank Yundeok and my wonderful gift from God, Janice. I am grateful to my daughter, Janice, for always giving me great joy and happiness and to my wife, Yundeok, for her support, love, infinite patience, confidence and encouragement in completing my PhD study.

**DEDICATION**

To my wife Yundeok, my daughter Janice  
and my parents

## TABLE OF CONTENTS

<b>LIST OF FIGURES.....</b>	<b>10</b>
<b>LIST OF TABLES.....</b>	<b>13</b>
<b>ABSTRACT.....</b>	<b>15</b>
<b>CHAPTER 1 INTRODUCTION.....</b>	<b>17</b>
<b>1.1 Rock fracturing due to rapid thermal cooling.....</b>	<b>18</b>
<b>1.2 Mine to Mill optimization .....</b>	<b>20</b>
1.2.1 Site specific blasting model for Mine to Mill Optimization .....	21
1.2.2 Utilizing new imaging technologies in rock mass characterization .....	22
1.2.3 Blending effect of mineral ores on flotation recovery in hard rock mines .....	24
<b>1.3 Research objectives and goals .....</b>	<b>26</b>
<b>1.4 Research contributions .....</b>	<b>27</b>
<b>1.5 Format of dissertation.....</b>	<b>28</b>
<b>CHAPTER 2 SUMMARY AND CONCLUSIONS .....</b>	<b>29</b>
<b>2.1 Summary and conclusions .....</b>	<b>30</b>
<b>2.2 Future studies .....</b>	<b>34</b>
<b>REFERENCES .....</b>	<b>36</b>
<b>APPENDIX A: EFFECT OF RAPID THERMAL COOLING ON MECHANICAL ROCK PROPERTIES .....</b>	<b>41</b>
<b>Abstract .....</b>	<b>42</b>

## TABLE OF CONTENTS – Continued

<b>A1. Introduction .....</b>	<b>43</b>
<b>A2. Heat treatment and sample preparation .....</b>	<b>48</b>
<b>A3. Effect of rapid thermal cooling on mode I fracture toughness (<math>K_{IC}</math>) and tensile strength of Coconino sandstone .....</b>	<b>50</b>
A3.1 Preliminary interpretation .....	54
<b>A4. Rapid cooling effect on porosity, seismic velocity and tensile strength in igneous and metamorphic rocks .....</b>	<b>56</b>
A4.1 Rock types that exhibited crack growth after cyclic thermal loading .....	58
A4.2 Rock types that exhibited crack healing after cyclic thermal loading .....	59
<b>A5. Three dimensional transient thermo-mechanical modeling.....</b>	<b>64</b>
<b>A6. Conclusions .....</b>	<b>73</b>
<b>References .....</b>	<b>75</b>
<b>APPENDIX B: SITE SPECIFIC BLASTING MODEL FOR MINE-TO-MILL OPTIMIZATION.....</b>	<b>78</b>
<b>Abstract .....</b>	<b>79</b>
<b>B1. Introduction .....</b>	<b>80</b>
<b>B2. Site-Specific blasting model .....</b>	<b>82</b>
B2.1 In-situ block size (F80) of the bench face.....	82
B2.2 Schmidt hammer hardness (SHH) and tensile strength .....	85
B2.3 Specific explosives energy ( $E_{SE}$ ) .....	88

## **TABLE OF CONTENTS – Continued**

B2.4 Data collection and analysis .....	89
<b>B3. Estimating the complete size distribution curve .....</b>	<b>91</b>
<b>B4. Application of the site-specific blast model .....</b>	<b>96</b>
<b>B5. Conclusions.....</b>	<b>100</b>
<b>References .....</b>	<b>102</b>

## **APPENDIX C: APPLYING RECENT IMAGING TECHNOLOGIES**

<b>TO ROCK MASS CLASSIFICATION .....</b>	<b>104</b>
<b>Abstract .....</b>	<b>105</b>
<b>C1. Introduction .....</b>	<b>106</b>
<b>C2. Bench block size using digital image processing.....</b>	<b>110</b>
C2.1 Average bench block size and 50% passing size (F50) .....	113
<b>C3. Measuring joint waviness and joint orientation by using ground-based LIDAR.....</b>	<b>117</b>
C3.1 Joint surface condition (joint condition factor, $J_C$ ) .....	118
C3.2 Joint Waviness ( $J_W$ ) .....	119
C3.3 Joint orientation: LIDAR scan vs. Manual measurement.....	127
<b>C4. Rock mass classification using ground-based LIDAR and point cloud processing .....</b>	<b>130</b>
C4.1 Manual geological cell mapping (Manual GSI) .....	131

## **TABLE OF CONTENTS – Continued**

C4.2 Automated geological cell mapping by using new technologies (Automated GSI) .....	133
C4.3 Comparison between the manual GSI and the automated GSI.....	136
<b>C5. Conclusion and discussion .....</b>	<b>137</b>
<b>References .....</b>	<b>141</b>
<b>Appendix .....</b>	<b>146</b>

## **APPENDIX D: BLENDING EFFECT OF MINERAL ORES ON FLOTATION RECOVERY IN HARD ROCK MINES.....154**

<b>Abstract .....</b>	<b>155</b>
<b>D1. Introduction .....</b>	<b>156</b>
<b>D2. Sample preparation .....</b>	<b>158</b>
D2.1 Flotation test .....	160
<b>D3. Characterization of ore grindability.....</b>	<b>160</b>
D3.1 Grinding time effect on flotation recovery .....	165
D3.2 Blending effect of minerals .....	168
<b>D4. Discussion and future works .....</b>	<b>173</b>
<b>References .....</b>	<b>176</b>

## LIST OF FIGURES

Fig. A1. The tested samples (left to right side): Skarn, Quartzite, Diabas (upper) and Diabase (with ore veins), KVS, Sierrita Granite (lower) .....	50
Fig. A2. The END (Edge Notched Disc) test for mode I fracture toughness with Sandstone .....	51
Fig. A3. The effect of temperature on Mode I fracture toughness and tensile strength .....	52
Fig. A4. The effect of cyclic thermal shock (100°C) on Mode I fracture toughness and tensile strength .....	54
Fig. A5. The Sketch of Possible Microcrack Mechanisms due to Rapid Cooling .....	56
Fig. A6. The “P” wave velocity change before and after 5 cyclic thermal shocks .....	58
Fig. A7. “P” wave velocity change before and after 5 cyclic thermal shocks in Diabase (no ore veins).....	60
Fig. A8. Average tensile strength change before and after 5 cyclic thermal shocks .....	61
Fig. A9. a) boundary conditions for the ANSYS simulations, b) locations referred to in Figures A11 and A13. .....	65
Fig. A10. Assumed film coefficient for various places around the specimen .....	66
Fig. A11. Temperature (°C) vs. time for various places in the specimen (refer to Figure A9b).....	67
Fig. A12. Distribution of temperature (°C) at 105 seconds .....	68
Fig. A13. Maximum principal stress (MPa) vs. time for various places in the specimen (refer to Figure A9b) .....	69
Fig. A14. Distribution of maximum principal stress (MPa) at 105 seconds .....	70

## LIST OF FIGURES – Continued

Fig. B1. Blasting in a quarry (Kim, 2006) .....	81
Fig. B2. Bench face images in a quarry (left) and in Mission copper mine (right) .....	83
Fig. B3. The example of the analyzed image of the bench face by using Split-Desktop .....	84
Fig. B4. Schmidt hammer hardness (Q) and the tensile strength for Argillite.....	86
Fig. B5. Schmidt hammer hardness (Q) and the tensile strength for Mission rock types .....	87
Fig. B6. Predicted size distribution curves as increasing P80.....	95
Fig. B7. Total production improvement (%) and total cost saving (%) vs. blast energy .....	99
Fig. C1. Quantification of GSI chart.....	109
Fig. C2. (a) Highway rock slope image for counting the joints (left) and (b) the delineated image (right) .....	114
Fig. C3. Images for counting the joints and the delineated image from a mine .....	115
Fig. C4. (a) 3D laser image (upper) and (b) triangular mesh (lower) .....	122
Fig. C5. (a) The found patches in the point cloud (upper) and (b) a generated stereonet (lower) .....	123
Fig. C6. (a) The selected Joint Set 1 in the stereonet (upper) and (b) the point cloud image (lower) .....	124
Fig. C7. Two selected patches in Joint Set 1 .....	125
Fig. C8. Two cross-sections of the selected patches in Joint Set 1 .....	125

**LIST OF FIGURES – Continued**

Fig. C9. LIDAR scan (upper) and manual measurement (lower) .....	128
Fig. C10. Manual GSI and automated GSI .....	136
Fig. D1. Six different ore samples.....	158
Fig. D2. The prepared ore samples in 1 kg bag for laboratory flotation tests.....	159
Fig. D3. Cumulative size distribution of six ore samples .....	161
Fig. D4. Grindability tests at each ore type.....	163
Fig. D5. The flotation recovery as changing grinding time and ore blending mixture	167
Fig. D6. The blends of hard and soft ores .....	171

## LIST OF TABLES

Table A1. Average porosity change before and after thermal shock .....	59
Table A2. Average porosity change before and after thermal shock .....	61
Table A3. Average tensile strength before and after thermal shock .....	62
Table A4. Average P wave velocity change before and after saturation .....	63
Table A5. The thermal and mechanical properties used in the Analysis simulations....	65
Table B1. Data collection from five shots in the Super Pit.....	89
Table B2. P50 and P80 in the Super Pit in ASARCO Mission.....	93
Table B3. P50 and P80 in quarries.....	93
Table B4. Xc calculation by using predicted P80 .....	95
Table B5. Predicted P80, total cost saving, and production increase as increasing the blast energy .....	100
Table C1. Measuring the bench block size by counting the joints.....	114
Table C2. Calculating the average block size .....	116
Table C3. Joint Waviness Description .....	120
Table C4. Joint Waviness Measurement by using LIDAR scan .....	126
Table C5. Joint Sets Orientation Information .....	130
Table C6. Rock Mass Classification (Q-system) by manual cell mapping.....	132
Table C7. Various correlations among the rock mass classifications .....	133
Table C8. GSI values by using 3D laser image and image processing software .....	134
Table D1. Metal analysis of six ore samples from a copper mine .....	159

**LIST OF TABLES – Continued**

Table D2. Base line flotation test results.....	164
Table D3. Flotation recovery of the blend of the hard and the soft ores at different grinding time .....	166
Table D4. Blending effect of classified ores on the flotation recovery .....	168
Table D5. Blending two of six ores without considering hardness and grindability ...	169
Table D6. Recovery changes without blending, with blending and with blending strategically .....	169
Table D7. The recovery of arithmetic mean and the actual recovery using blending effect.....	173

## ABSTRACT

The research presented in this dissertation consists of four topics. The first of these topics is an experimental study of rock fracturing due to rapid thermal cooling, and the other three topics are related to mine-to-optimization. This includes the development and testing of a site-specific model for blast fragmentation, the development of a technique for utilizing digital image processing and ground-based LIDAR for rock mass characterization, and an experimental study of the effects of ore blending on mineral recovery. All four topics are related through the subject of rock fracturing and rock fragmentation. One way to view mining is that it is chiefly composed of rock breaking and comminution steps, starting with drilling and blasting, then hauling (which results in size reduction), and then the comminution steps in the mill which include primary and secondary crushing and coarse and fine grinding. The final step of mineral liberation is wholly dependent on achieving the proper rock fracturing in the rock breaking and comminution steps, and cost and throughput optimization can be realized by optimizing the mine-to-mill rock fracturing processes.

The results from this research are important and can be used to improve engineering design associated with rock excavation and rock fragmentation. First of all, a successful set of laboratory experiments and 3D numerical modeling was conducted, looking at the effects of rapid thermal cooling on rock mechanical properties. The results gave the unexpected finding that depending on the rock type and the thermal conditions, rapid cooling can result in either overall crack growth or crack closing. Secondly, a site-specific model for predicting blast fragmentation was developed and tested at an open-pit

copper mine in Arizona. The results provide a practical technique for developing a calibrated blasting model using digital images and digital image processing software to estimate in-situ block size, and a calibrated Schmidt hammer to estimate intact tensile strength. Thirdly, a new technique was developed to conduct cell mapping in open-pit mines using the new technologies of digital image processing and ground-based LIDAR. The results show that the use of these new technologies provide an increased accuracy and the ability for more sophisticated slope stability analyses with no increase in field time only a moderate increase in data processing time. Finally, a successful set of laboratory experiments was conducted looking at the effects of ore blending and grinding times on mineral recovery from a set of six ore from a copper mine in Arizona. The results gave the unexpected finding that for a fixed grinding time, the mineral recovery of the blended ores exceeded the average of the individual recoveries of the same ores unblended.

## **CHAPTER 1**

### **INTRODUCTION**

Rock mechanics and rock engineering are important subjects in the fields of mining, civil, geological, and petroleum engineering [1,2]. Rock fracturing concerns the propagation of cracks and fractures in rocks and the resulting fragmentation and failure, and rock fracturing is a central topic in most rock mechanics and rock engineering applications [3-8]. In mining for example, rock fracturing is involved in all steps in mining, including drilling, blasting, hauling, crushing, grinding and mineral liberation. Rock fracturing research includes lab testing, numerical modeling, and field characterization and testing. Optimization is another aspect of rock fracturing that is very important in most engineering applications. In mining, for example, the daily mineral production rate can be maximized and the overall mining cost can be minimized by optimizing the fracturing that occurs during blasting and comminution. Mine-to-mill optimization is the term used for this type of optimization in the mining industry, and even though rock fracturing is not in the term, it is central to almost all aspects of this important area of study.

The research presented in this dissertation consists of four topics. The first of these topics is an experimental study of rock fracturing due to rapid thermal cooling, and the other three topics are related to mine-to-optimization. This includes the development and testing of a site-specific model for blast fragmentation, the development of a technique

for utilizing digital image processing and ground-based LIDAR for rock mass characterization, and an experimental study of the effects of ore blending on mineral recovery. Each of these topics is discussed in the next two sections, Sections 1.1 and 1.2. Objectives and goals of the research presented in this dissertation are given in Section 1.3, and the primary research contributions are given in Section 1.4. The format for this dissertation is in the form of four journal manuscripts, and this format is discussed in Section 1.5.

### **1.1 Rock fracturing due to rapid thermal cooling**

There are many important engineering applications in which rock is subjected to thermal loading. These include deep drilling and deep underground mining, underground storage of high-level nuclear waste, and geothermal energy extraction. It also includes the daily and seasonal temperature fluctuations of rock along highways, railways, and dam and bridge foundations. In some of these applications, the occurrence of high thermal stresses and associated rock fracturing is due to the large, slow changes in temperature. In this case thermal stresses are generated by geometric constraints (rock unable to expand freely) or the heterogeneous distribution of rock properties. In underground nuclear waste storage, for example, the heating of underground drifts to over 150°C can generate compressive tangential stresses as high as 60 MPa at the boundary of the excavations [8]. Also, experiments have shown that when hard rocks such as granite and quartzite are slowly heated to temperatures over 250°C, tensile

cracking occurs due to the mismatch in elastic and thermal properties between grains and phase transitions in the individual minerals [9,10]. In other applications, high thermal stresses and associated cracking are due to smaller but rapid changes in temperature. In this case thermal stresses are generated by the transient distribution of temperatures in the rock. The historic method of rock excavation by heating up the rock with a fire and then dousing the rock with cold water is an example of this type of thermal loading. More modern examples include the sudden flow of cold air due to ventilation in a deep underground excavation, and the solar heating and cooling of rock slopes [11-14]. In general, the applications involving slow heating or cooling are analyzed using steady state heat flow, while applications involving rapid heating or cooling must be analyzed with transient heat flow.

Many researchers have investigated the effects of thermal loading on mechanical rock properties [11-14]. Most of this research has involved large but gradual changes in temperature, with temperature changes over 300°C in most cases. The research in this dissertation focuses on the effects of rapid thermal cooling over small to moderate changes in temperature, cooling from 100-300°C to room temperature. This is a subject with very little previous work but with important practical applications in deep mining, deep drilling and geothermal energy extraction. Many modern mines are now at depths below 1500 meters, and ventilation in these mines will result in a fairly rapid cooling from an in-situ temperature in many cases over 75°C to a working temperature around 25°C. Similarly, moderate changes in temperature can occur in deep drilling for petroleum and hot rock drilling for geothermal energy extraction.

The work presented in this dissertation involves laboratory tests and three-dimensional numerical modeling. Laboratory tests have been conducted to investigate the effect of rapid cooling on samples of igneous, sedimentary, and metamorphic rocks. In the laboratory, samples were first slowly heated to a desired temperature and then rapidly cooled back to room temperature using a fan. Experimentation included Edge Notched Disk (END) tests to determine the Mode I fracture toughness [15], Brazilian Disc tests to determine tensile strength, seismic tests to determine P wave velocity, and porosity tests. The results from the rapid thermal cooling tests were very interesting and showed that crack growth occurred in some rock types subjected to rapid thermal cooling while crack closing and healing occurred in other rock types. To understand the results, the experiments were simulated using a 3D finite element numerical model along with some time-dependent fracture mechanics analysis. The results of this study are presented in Appendix A.

## **1.2 Mine to Mill Optimization**

Hard rock mining is traditionally thought of as two independent stages, mining (drilling, blasting, hauling) and mineral processing (comminution and mineral liberation). Even though the two stages are intimately connected, they are often treated as stand-alone processes with separately trained engineers and workers. In the study presented in this dissertation, energy efficiency in the comminution process of an actual open-pit copper mine was improved by considering the two stages together as a whole process, referred to

as the concept of Mine to Mill optimization [16-18]. In particular, this study focused on optimizing blasting fragmentation, which is one of the key considerations for Mine to Mill optimization because it can generate increased production, energy saving, and total expense reduction, although the specific conditions at each mine need to be carefully considered [19,20]. Recent studies have shown that the energy consumption in comminution processes can be decreased by increasing the powder factor; increased explosive energy can result in finer fragmentation and increased rock damage (microcracking), which has a significant impact on the downstream costs associated with loading, hauling, crushing, and even grinding [19,21,22]. The blasting optimization study presented in this dissertation was conducted at a copper mine in southern Arizona, with the remarkable result of a 6% increase of throughput and an estimated additional profit of nearly 40M dollars (at \$4.0 per pound of copper) annually.

For the optimized blasting, there are two main research subjects: one is “controlling blast fragmentation,” which involves being able to control the fragmentation based on the rock conditions and the blasting design. The other is “finding the target blast fragmentation”, which involves being able to determine the target fragmentation size based on optimizing comminution and mineral liberation through the mill. These subjects are described below.

### 1.2.1 Site specific blasting model for Mine to Mill Optimization

For controlling blast fragmentation, the Kuz-Ram empirical fragmentation model, suggested by Cunningham, is the most popular blast fragmentation prediction model, and

has been used by many researchers and engineers [23,24]. However, due to the complexity of rock properties and geological structures, a universally applicable blast fragmentation model may not exist. In addition, it is difficult to obtain reliable data for the model, which includes in-situ block size, intact rock strength, and post-blast fragmentation. It is important to note that, although tensile failure is the most common failure mode in rock fracturing, tensile strength is not considered in the current blasting models [24-27]. Thus, to control blast fragmentation (as part of the study of optimized blasting), it is recognized that blast fragmentation models must have parameters that can be adjusted for a specific rock type or area within a mine, and it must be possible to obtain the parameters easily, quickly, and consistently for applicability in active mining operations.

The site-specific blast model developed in this research is adjustable for different areas in a mine and relates the specific explosive energy (ESE), blast fragmentation (P80), bench face block size (F80), and intact rock tensile strength (To). There are two main innovations in the model and its use: one is the use of the image processing technology to obtain in-situ block size, and the other is the utilization of the Schmidt Hammer Hardness (SHH) to estimate tensile strength. The results of this study are presented in Appendix B.

#### 1.2.2 Utilizing new imaging technologies in rock mass characterization

Estimating rock mass strength in hard rock mines is one of the main considerations in reducing slope stability problems and in optimizing stripping ratios (reducing waste

extraction by manipulating the slope angle). However, in hard rock mines, estimating rock mass strength is generally very difficult and challenging because of the heterogeneity and complexity of rock masses.

As part of mine-to-mill optimization, blast fragmentation is optimized, and often a finer fragmentation achieved by increasing the powder factor will result in improved comminution and mineral liberation at an overall reduced cost. However, as part of a target blast fragmentation (target P80, which is the 80% passing size from the muckpile after blasting) value for a given mine, slope stability must also be carefully considered. An increased powder factor can result in increased blast vibrations and blast-damaged slopes. Both of these factors could result in slope instability in the form of rockfall, bench-scale slope instability and large-scale slope failure. The cost of a slope instability in terms of lost production or personnel injury can far outweigh any advantages in comminution and mineral liberation. Thus target blast fragmentation values based only on mill optimization are not always achievable. For example, consider a target P80 for a mine of 6 inches, which was determined by considering the whole comminution and liberation processes. The required blast energy for that fragmentation is 400 Kcal/ton, which was determined by considering the rock type, bench structure, and rock properties. However, 400 Kcal/ton of blast energy may not be acceptable, and it can induce a significant impact (due to high blast vibration) on the slope stability. Therefore, deciding the optimum blast energy must include a consideration of slope stability, and one of the main challenges in slope stability studies is an estimation of rock mass strength. Due to practical mining considerations such as the high rate and volume of mining that occurs in

large open pit mines, the rock mass strength needs to be determined quickly, easily, and consistently. However, traditional rock mass characterization of large open-pit mines requires significant data collection, which is time-consuming and involves safety hazards and human bias.

Hence, improving the technologies used for rock mass characterization is important not only for slope stability studies but also in deciding the target blast fragmentation. In addition, if rock mass strength can be estimated quickly and consistently, then rock mass strength can be directly utilized in the blast fragmentation prediction model.

Line and cell mapping are the traditional field techniques for collecting rock mass characterization information [28-31]. The replacement of standard line and cell mapping with recent technologies has been investigated in the studies described in this dissertation, specifically the following techniques: (1) utilizing digital image processing for the bench block size characterization, (2) measuring joint waviness and joint orientation by using ground-based LIDAR, and (3) determining rock mass classification (GSI) using ground-based LIDAR and point cloud processing. The details are presented in Appendix C.

### 1.2.3 Blending effect of mineral ores on flotation recovery in hard rock mines

In Mine-to-Mill optimization, the target blast fragmentation for each rock type can be determined by considering all downstream processes as a whole: loading, hauling, crushing, grinding and mineral liberation. However, in actual hard rock mining, rock types from different areas are often blended to provide a consistent ore grade for the mill.

Thus, the effect of blending rock types needs to be investigated as part of the work of finding the target blast fragmentation for each rock type. It has been shown that blasting can be helpful in reducing the effect of mineral hardness on combined mineral grinding [19,20].

This dissertation describes a blending study that was conducted to improve mill performance at a copper mine in Arizona. Initially, based on Yusupov [32], a blending strategy was proposed to improve flotation by classifying the ore into two types, hard ores and soft ores. It was expected that doing so would either decrease or, perhaps, totally eliminate the problems of sliming (overgrinding of soft ores) and incomplete liberation that are usually observed in the grinding circuits. However, the actual test results were unexpected. There are two main findings described in this dissertation: one is the effect of grinding time on the flotation recovery of mixed ores, and the other is the effect of the blending of different ore minerals on flotation recovery. A remarkable result from the research is that an average increase of flotation recovery of 5.7% was observed (the maximum increase could be as high as 12.3 %.) when the ores were blended, compared with the same grinding time for the ores unblended. In a medium size copper mine (with an ore production rate of 50,000 t/day), a 1% increase in flotation recovery results in an additional profit of 8.0M dollars annually (at \$4.0 per pound of copper). Therefore, although more studies are needed in applying the blending effect in the actual mineral process, it is believed that the study of blending may result in huge potential profits, 46M dollars per year (5.7% increase in flotation recovery), making further investigation worthwhile. The detailed results of the study are shown in Appendix D.

### **1.3 Research Objectives and Goals**

The primary goal of the research presented in this dissertation is “Safe Production,” which involves improving both mine safety and productivity in hard rock mines. Specific objectives and goals of the research in this dissertation are given below.

- 1) In deep underground hard rock mines, rapid cooling by as much as 60°C can be caused by ventilation and this rapid cooling could impact the stability of underground drifts. The first goal was to conduct laboratory tests with actual rock specimens from a deep underground mine, under experimental conditions that closely match actual field conditions. As part of this goal, the results would be analyzed using modern 3D numerical modeling tools.
- 2) Rock mass characterization is very important to mine slope stability and worker safety, and the traditional method of manual cell mapping has issues of safety, access, human bias and timeliness. The second goal was to develop more automated techniques for cell mapping that utilize new imaging technologies such as digital images and ground-based LIDAR that are very high resolution and also allow data to be collected at a distance from the rock faces. As part of this goal, the new techniques would be compared with traditional cell mapping at an actual mine.
- 3) Blast fragmentation prediction models are often utilized to optimize the blast design for a mine-to-mill strategy. However, existing models are imprecise and impractical to use. The third goal was to develop a new approach to blast fragmentation modeling that is, first of all, site-specific for a given rock type and rock conditions, and secondly,

utilizes new technologies and tools that are accurate, easy to use, and allow data collection from a distance. As part of the goal, the model would be validated at an actual mine.

4) A typical mine is comprised of many different rock types, and the blending of ore types in the mill must be considered in a mine-to-mill strategy. The fourth goal was to conduct an experimental blending study using rock types from an actual mine. As part of this goal, both the effects of grinding time and blending strategy would be considered.

“Safe Production” (increasing productivity safely) is the ultimate goal in the mining industry. Although the research presented in this dissertation consists of various research topics, the goal of all the research is to increase mine safety and productivity.

#### **1.4 Research Contributions**

Several unique research contributions were made as part of the research described in this dissertation, as listed below. Along with each of these contributions is a journal manuscript that was either already submitted or will be submitted in the near future.

- 1) A successful set of laboratory experiments and 3D numerical modeling was conducted, looking at the effects of rapid thermal cooling on mechanical properties (journal manuscript in Appendix A).
- 2) A site-specific model for predicting blast fragmentation was developed and tested at an open-pit copper mine in Arizona (journal manuscript in Appendix B, already in print)

- 3) A new technique was developed to conduct cell mapping in open-pit mines using the new technologies of digital image processing and ground-based LIDAR, and tested at an actual open pit copper mine (journal manuscript in Appendix C).
- 4) A successful set of laboratory experiments was conducted looking at the effects of ore blending and grinding times on mineral recovery (journal manuscript in Appendix D, submitted).

## **1.5 Format of Dissertation**

The results of the research presented in this dissertation have been put in the format of four journal manuscripts, and these four journal manuscripts are presented in Appendices A through D. The four journal manuscripts are: (A) Effect of rapid thermal cooling on mechanical rock properties, (B) Site specific blasting model for Mine-to-Mill Optimization, (C) Applying recent imaging technologies to rock mass classification, and (D) Blending effect of mineral ores on flotation recovery in hard rock mines. Each paper is complete, with introduction, conclusions and references. Overall conclusions and future work from these papers is given in the next section (Section 2).

## **CHAPTER 2**

### **SUMMARY AND CONCLUSIONS**

The results of the research presented in this dissertation have been formatted as four journal manuscripts, as presented in Appendices A through D. The first of these papers is on the topic of rock fracturing due to rapid thermal cooling (Appendix A), and the other three papers are on various topics related to mine-to-optimization. This includes a paper on a site-specific model for blast fragmentation (Appendix B), a paper on the use of digital image processing and ground-based LIDAR for rock mass characterization (Appendix C), and a paper on the effects of ore blending on mineral recovery (Appendix D). All four papers are related through the important topic of rock fracturing and rock fragmentation. One way to view mining is that it is chiefly composed of rock breaking and comminution steps, starting with drilling and blasting, then hauling (which results in size reduction), and then the comminution steps in the mill which include primary and secondary crushing and coarse and fine grinding. The final step of mineral liberation is wholly dependent on achieving the proper rock fracturing in the rock breaking and comminution steps, and cost savings can be realized by optimizing rock breaking and fragmentation in the whole process from mine to mill.

The following are the summary and conclusions and proposed future studies of the research contained in this dissertation.

## 2.1 Summary and Conclusions

1) A successful set of laboratory experiments and 3D numerical modeling was conducted, looking at the effects of rapid thermal cooling on mechanical properties. Rapid thermal cooling occurs in several important mining and geotechnical engineering applications, including the ventilation of mines at deep depth and deep drilling. Tests were conducted by slowly heating samples of granite, sandstone and other rocks in an oven, followed by rapid cooling with a fan. Samples were cooled from oven temperatures of 100, 200 and 300°C, and testing to evaluate the changes in mechanical properties included END tests to determine the fracture toughness [15], Brazilian disc tests to determine the tensile strength, and P-wave velocity and porosity tests. The results were very interesting and demonstrated that rapid cooling from low to moderate temperature changes can result in significant changes in mechanical properties. The rapid cooling results from 100°C were unexpected and showed two very different types of behavior depending on the rock type. In some of the rock types that were tested, the 100 °C rapid cooling results were consistent with microcrack initiation and propagation. This includes a decrease in P wave velocity, a decrease in tensile strength, and an increase in porosity. In other rock types that were tested, the 100 °C rapid cooling results were consistent with microcrack closing and crack healing. This includes an increase in P wave velocity, increase in tensile strength, and decrease in porosity. The results were explained by conducting 3D thermo-mechanical modeling using the ANSYS finite element program [33]. The ANSYS results indicated that within the first five minutes of rapid cooling,

there is a thin (less than 5 mm) region near the outside of the sample where large tensile stresses occur and microcracking would be expected. During the same short time period, there is a large area in the middle of the sample where lower magnitude compressional stresses occur and crack closure would be expected. In the more heterogeneous and course grained rocks that were tested, it was shown that time-dependent crack growth could occur on the outside of the sample and dominate any closure occurring on the inside of the sample, resulting in an overall increase in porosity, decrease in P wave velocity, etc. In the less heterogeneous and fine-grained rocks that were tested, it was shown that tension cracking on the outside could not occur, while crack closure on the inside could still occur, resulting in an overall decrease in porosity, increase in P wave velocity, etc.

2) A site-specific model for predicting blast fragmentation was developed and tested at an open-pit copper mine in Arizona. The model was developed to be an integral part of a mine-to-mill scheme for open-pit hard rock mines. It is expected that different types of ore will occur in different parts of a mine. These different ores will have different hardnesses and grades, as well as different propensities for slope instability. Based on various min-to-mill studies, the target fragmentation values for the different parts of the mine can be determined. The site-specific blasting model is then used to determine the burden, spacing and powder factor to achieve that fragmentation [34]. The blasting model is simple and contains four parameters: the in-situ block size ( $F_{80}$ ), the post-blast fragmentation ( $P_{80}$ ), the intact tensile strength ( $T_o$ ), and the specific blast energy ( $E_{SE}$ ).

To validate the model, five test blasts were conducted in one ore type (argellite) at a copper mine in Arizona, where the blast energy ( $E_{SE}$ ) was varied and the resulting fragmentation (P80) was measured. In addition, the in-situ block size (F80) and the tensile strength ( $T_0$ ) were determined using two innovations, digital image processing software to estimate the block size and a Schmidt hammer calibrated to each ore type to estimate the tensile strength. The calibrated blasting model gave a very good correlation with the results from the test shots, and as a demonstration the calibrated model was used to estimate the optimal burden, spacing and powder factor to optimize total mine-to-mill cost and throughput.

3) A new technique was developed to conduct cell mapping in open-pit mines using the new technologies of digital image processing and ground-based LIDAR. Slope stability is an integral part of mine-to-mill optimization. The target fragmentation for a section of a mine depends on the consideration of total cost, mineral recovery, and ensuring the stability of the slopes. Causes for slope instability could be inadequate blasting, resulting in damaged slopes, or excess ground vibrations resulting in the sliding and toppling of rock blocks. As part of mine-to-mill optimization, therefore, rock mass characterization must be carried out and utilized in the determination of target fragmentation. Traditional techniques for rock mass characterization include cell mapping and scanline surveying. In an effort to address issues of safety, access, human bias and timeliness, traditional cell mapping was compared with rock mass characterization utilizing two new technologies, digital image processing and ground-

based LIDAR. A case study was conducted at an open-pit copper mine in Arizona, where eight 10 m x 10 m cells were characterized using both using the traditional and the new technologies. Using both methods, the GSI rock mass classification number was estimated in each cell [35], as well as a stereonet pole plot of joint orientations. The results show a fair correlation between the traditional and the new techniques for estimating GSI and joint orientations. This is to be expected, since manual cell mapping is a technique for quickly obtaining data in the field, and only very limited measurements are made, and with limited access. The new technologies generate a large database of information on each cell, which will result in increased accuracy as well as the ability to process the data in many different ways. The amount of time spent in the field is about the same between the traditional cell mapping and the collection of data using digital images and ground-based LIDAR (20-30 minutes per cell). Processing the data from the new technologies requires several additional hours of analysis per cell.

4) A successful set of laboratory experiments was conducted looking at the effects of ore blending and grinding times on mineral recovery. Ore blending and grinding time are integral parts of mine-to-mill optimization, and are used as part of the information to determine target fragmentation and comminution values for blasting, crushing and grinding. The blending study was conducted using six rock types from a copper mine in Arizona: argillite, siltstone, garnet tactite (GTT), diopside tactite (DTT), marble, and green garnet. Grindability tests were conducted to decide the proper grinding times for the laboratory flotation tests and to investigate the grindability (hardness) of each rock

type. The rock samples were classified as ‘hard ores’ (argillite, siltstone and GTT) and ‘soft ores’ (DTT, marble, and green garnet), and the grinding time was set at 35% retained 100 mesh. Initially, the grinding time effect on the flotation recovery of the mixture of two ores (soft and hard ores) was investigated. Test results showed that using the hard ore grinding time showed better recovery than other grinding times when hard and soft ores were mixed. Thus it was concluded that “incomplete liberation” of hard ores rather than “overgrinding” of soft ores had a significant impact on the decrease of flotation recovery. In addition, further studies were conducted to observe the “blending effect” and the harmony of ores. The results showed that although there might be the effect of either “incomplete liberation” or “overgrinding” in processing mixed ores (hard and soft ores), the average recovery after blending was 5.7% higher (increase after blending) than before blending, and the maximum possible increase of the recovery was 12.3% from mixing ores and considering the best harmony of two ores. In particular, it was also found that all the recoveries of physically blending two ores were higher than the arithmetic mean recovery. This positive impact on the flotation recovery was referred to as the “blending effect” in this study.

## 2.2 Future Studies

- 1) In the study of the effect of rapid thermal cooling on rock properties, additional experiments (such as Atomic Force Microscopy) would be desirable to verify where

crack density changes occurred and why certain rock types show crack healing or crack growth.

- 2) In the site-specific blast model, more field blasting tests would be desirable to further validate the usefulness of the model. In particular the effect of tensile strength on the specific explosives energy ( $E_{SE}$ ) could be investigated by testing in rocks with different Schmidt hammer hardness (SHH). In addition, more studies on finding the optimum blast energy at each rock type in a hard rock mine could be conducted.
- 3) The technique of cell mapping and GSI determination using the technologies of digital image processing and ground-based LIDAR should be integrated into the site-specific blast model. Also more field studies should be conducted to further validate the automated cell mapping technique. Finally, techniques should be developed to extract the joint smoothness ( $J_s$ ) and the joint alteration ( $J_a$ ) from either digital images or LIDAR point clouds.
- 4) The “blending effect” can be used to obtain better flotation recovery for problematic ores, and additional studies are needed in this area. In addition, further investigations are needed to apply the blending effect into actual mineral processing plants. Such a study could result in significant increases in actual mineral recoveries at an operating plant.

## REFERENCES

- [1] Spe-Isrm International Conference Eurock 1994 Rock Mechanics in Petroleum Engineering, *Taylor & Francis, 1<sup>st</sup> ed.*.
- [2] Fjar, Erling, Holt, R. M., Raaen, A. M., Risnes, R., Horsrud, P. 2002 Petroleum Related Rock Mechanics, *Elsevier Science, 2<sup>nd</sup> ed.*.
- [3] Martin, R. J. 1972. Time-dependent crack growth in quartz and its application to the creep of rocks. *J Geophys Res*, 77(8):1,405-1,409
- [4] Swain, M. V., Williams, J. S., Lawn, B. R. and Beek, J. J. H. 1973. A comparative study of the fracture of various silica modifications using Hertzian test, *J Mater Sci*, 8(8): 1,153-1,164
- [5] Atkinson, B. K., 1979 A fracture mechanics study of subcritical tensile cracking of quartz in wet environments. *Pure Appl Geophys*, 117(5):1,011-1,024
- [6] Costin, L. S., 1987 Time-dependent deformation and failure, In: *Fracture mechanics of rock. London: Orlando: Academic Press*, pp 167-215
- [7] Swanson, P.L. 1984 Subcritical crack growth and other time- and environment-dependent behavior in crustal rocks. *J. Geophys Res*, 89(B6):4,137-4,162
- [8] Kemeny, J. 2005. Time dependent drift degradation due to the progressive failure of rock bridges along discontinuities, *Int. J. Rock Mech. Min. Sci.*, Vol 42, pp 35-46.
- [9] Yavuz, H., Altindag, R., Sarac, S., Ugur, I., Sengun, N.. 2006. Estimating the index properties of deteriorated carbonate rocks due to freeze-thaw and thermal shock weathering, *Int. J. Rock Mech. Min. Sci.*, Vol. 43, pp 767-775

- [10] Kingery, W. D. 1955. Factors affecting thermal stress resistance of ceramic materials, *Journal of The American Ceramic Society, Vol. 38, No 1.*
- [11] Zomeni, Zomenia 1997. Thermally induced microfracturing in Quartzite, *Masters of Science dissertation, Mining and Geological Engineering, the University of Arizona, Tucson, 1997.*
- [12] Meredith, P.G. and Atkinson, B.K. 1985. Fracture toughness and subcritical crack growth during high-temperature tensile deformation of Westerly granite and Black gabbro, *Physics of the Earth and Planetary Interiors, Vol.39*, pp 33-51.
- [13] Glamheden, R., Lindblom, U. 2002. Thermal and mechanical behavior of refrigerated caverns in hard rock, *Tunnelling and Underground Space Technology, Vol. 17, Issue 4*, pp.341-353
- [14] Bellopede, R., Ferrero, A.M., Manfredotti, L., Marini, P., Migliazza, M., 2006. The effect of thermal stresses on the mechanical behavior of natural building stones, *Fracture and Failure of Natural Building Stones, Part II*, pp. 397-425
- [15] Donovan, J. G., 2006, Fracture toughness based models for the prediction of power consumption, product size, and capacity of jaw crushers, *Doctor of Philosophy dissertation, Mining and Mineral Engineering, Virginia Tech, Blacksburg.*
- [16] Kim, K. M., 2006, Blasting design using fracture toughness and image analysis of the bench face and muckpile, *Master of Science thesis, Mining and Mineral Engineering, Virginia Tech, Blacksburg*

- [17] Kim, K.M. and Kemeny, John, 2011, Site Specific Blasting Model Using Schmidt Tensile Strength and Image Analysis, *International Society of Explosives Engineers (ISEE), San Diego*
- [18] Kim, K.M. and Kemeny, John, 2011, Site Specific Blasting Model for Mine-to-Mill Optimization, *Transactions of the Society for Mining, Metallurgy and Engineering*, Vol.330. PP. 543-548
- [19] Nielsen, K., Malvik, T., 1999, Grindability enhancement by blast-induced microcracks, *Powder Technology 105*, pp 52-56.
- [20] Kim, S. J., 2010, An Experimental Investigation of the Effect of Blasting on the Impact Breakage of Rocks, *Master of Applied Science thesis, The Robert M. Buchan Department of Mining, Queen's University, Kingston, Canada*
- [21] JKMRC, 1996, Open Pit Blast Design: analysis and optimization *The University of Queensland.*
- [22] Nielsen, K., Lownds, 1997, Enhancement of Taconite Crushing and Grinding Through Primary Blasting, *Int. J. Rock Mech. Min. Sci.*, Vol 34:3-4, paper No. 226
- [23] Spathis, A.T., 2004, A Correction relating to the Analysis of the Original Kuz-Ram Model, *Fragblast*, Vol.8, No 4, pp 201-205
- [24] Kuznetsov, V.M., 1973, The mean Diameter of the Fragments Formed by Blasting Rock, *Soviet Min. Sci. Vol. 9*, pp 144-148
- [25] Chung, S. H. & Katsabanis, P.D. 2000, Fragmentation prediction using improved engineering formulae. *Fragblast*, vol. 4, No. 3-4, pp 198-207.

- [26] Cunningham, C. 1983, The Kuz-Ram Model for the Prediction of Fragmentation from Blasting, *Proceedings of the international Symposium on Rock Fragmentation and Blasting, Lulea, Sweden.*
- [27] Cunningham, C. 1987, Fragmentation Estimations and the Kuz-Ram Model – Four years on, *Proceedings of the second international Symposium on Rock Fragmentation and Blasting, Keystone, Colorado.*
- [28] Krauland, N.; Söder, P.; Agmalm, G., 1989, Determination of rock mass strength by rock mass classification-some experience and questions from Boliden mines, *Int. J Rock Mech. Min. Sci* 26(1):115-123
- [29] Bieniawski, Z. T., 1976, Engineering classification in rock engineering. In: *Proeddings of the Symposium on Exploration for Rock Engineering, Johannesburg*, 97-106
- [30] Hoek, E. and Brown, E. T., 1997, Practical estimates of rock mass strength. *Int. J. Rock. Mech. Min.*, 34 (8), 1165-1186
- [31] Barton N, Lien NR, Lunde J., 1974, Engineering classification of rock masses for the design of tunnel support. *Rock Mech* 6(4): 189-236
- [32] Yusupov, T.S., Kirillova, E.A., and Shumskaya, 2007, Mineral Hardness Effect on The Combined Mineral Grinding, *Journal of Mining Science*, Vol. 43, No. 4
- [33] Srinivas, Paleti; Sambana, Krishna Chaitanya; Datti, Rajesh Kumar 2010. Finite element analysis using ANSYS 11.0, *PHI Learning Private Limited, New Delhi.*
- [34] Rustan, Agne, 1998, Rock Blasting Terms and Symbols *A.A. Balkema, Rotterdam, Brookfield*

[35] Cai, M.; Kaiser, P.K.; Uno, H.; Tasaka, Y.; Minami M., 2004, Estimation of rock mass deformation modulus and strength of jointed hard rock masses using the GSI system, *Int. J Rock Mech Min Sci* 41:3-19

## **APPENDIX A: EFFECT OF RAPID THERMAL COOLING ON MECHANICAL ROCK PROPERTIES**

**Kwangmin Kim, John Kemeny, and Mark Nickerson**

*The University of Arizona, Tucson, AZ, U.S.A.*

WILL BE SUBMITTED TO ROCK MECHANICS AND ROCK  
ENGINEERING (2012).

## **Effect of Rapid Thermal Cooling on Mechanical Rock Properties**

**Kwangmin Kim, John Kemeny, and Mark Nickerson**  
*The University of Arizona, Tucson, AZ, U.S.A.*

### **ABSTRACT**

Laboratory tests have been conducted to investigate the effects of rapid thermal cooling on various rock samples including igneous, sedimentary, and metamorphic rocks. At first, various types of thermal loading were conducted: heating up to 100°C, 200°C, and 300°C, followed by rapid cooling with a fan. In addition, multiple cyclic thermal cooling (10, 15 and 20 cycles) with a maximum temperature of only 100°C was conducted. Experimentation included Edge Notched Disk (END) Tests to determine the Mode I fracture toughness, Brazillian Disc Tests to determine tensile strength, seismic tests to determine P wave velocity, and porosity tests leading to meaningful results. Even though only small changes of temperature (rapid cooling from 100°C to room temperature) were applied, the results showed that crack growth occurred in some rock types (Granite, Diabase with ore veins, and KVS ) while crack healing occurred in other rock types (Diabase without ore veins, Quartzite, and Skarn). To better understand the results, 3D transient thermo-mechanical analysis was conducted using the ANSYS program. The results indicated that there was a thin region near the outside of the sample where large tensile stress occur and microcracking would be expected, and that there was a large area in the middle of the sample where lower magnitude compressional stresses occur and

crack closure would be expected. It was found that the more heterogeneous and more course grained rock types are more likely to exhibit *crack growth*, while less heterogeneous and more fine-grained rocks are more likely to exhibit *crack healing*.

## A1. INTRODUCTION

There are many important engineering applications in which rock is subjected to thermal loading. These include deep drilling and deep underground mining, underground storage of high-level nuclear waste, and geothermal energy extraction. It also includes the daily and seasonal temperature fluctuations of rock along highways, railways, and dam and bridge foundations. In some of these applications, the occurrence of high thermal stresses and associated rock fracturing is due to the large, slow changes in temperature. In this case thermal stresses are generated by geometric constraints (rock unable to expand freely) or the heterogeneous distribution of rock properties. In underground nuclear waste storage, for example, the heating of underground drifts to over 150°C can generate compressive tangential stresses as high as 60 MPa at the boundary of the excavations [1]. Also, experiments have shown that when hard rocks such as granite and quartzite are slowly heated to temperatures over 250°C, tensile cracking occurs due to the mismatch in elastic and thermal properties between grains and phase transitions in the individual minerals [2,3]. In other applications, high thermal stresses and associated cracking are due to smaller but rapid changes in temperature. In this case thermal stresses are generated by the transient distribution of temperatures in the rock. The historic method of rock excavation by heating up the rock with a fire and then dousing

the rock with cold water is an example of this type of thermal loading. More modern examples include the sudden flow of cold air due to ventilation in a deep underground excavation, and the solar heating and cooling of rock slopes [4-7]. In general, the applications involving slow heating or cooling are analyzed using steady state heat flow, while applications involving rapid heating or cooling must be analyzed with transient heat flow.

Rapid heating or cooling of rock is generally accompanied by regions of both tension and compression. For example, if a cold temperature is suddenly applied to a warm or hot rock volume, a tensional tangential stress is generated at the surface of the rock where the cold temperature is applied, accompanied by compressional stresses behind the tension region. With time, as steady state conditions prevail, the tensional and compressional stresses decrease to zero. In theory, a maximum thermal stress of  $E\alpha\Delta T/(1-v)$  could be generated (where E is Young's modulus,  $\alpha$  is the coefficient of thermal expansion,  $\Delta T$  is the change in temperature, and  $v$  is Poisson's ratio). For example, for a rock at a depth of 2000 meters at a temperature of 80 °C, and the rapid application of a cooler temperature of 25 °C, a maximum tensile stress at the boundary of the excavation of about 14 MPa could be generated (assuming  $E=50\text{GPa}$  and  $\alpha=5\times10^{-6}/^\circ\text{C}$ ). This is sufficient to result in tensile cracking. The convective heat transfer coefficient (also referred to as the film coefficient) dictates the speed or efficiency of heat transfer [8]. For very rapid cooling of a hot rock sample by dropping into cold water, for example, the heat transfer coefficient

could be above 2000 W/m<sup>2</sup>K. For moving air, the heat transfer coefficient ranges from 100 - 500 W/m<sup>2</sup>K.

This paper describes a series of experiments that were conducted on samples of igneous, sedimentary, and metamorphic rocks. Samples were slowly heated to temperatures of 100, 200 and 300 °C, followed by rapid cooling with a fan blowing room temperature air. Experiments conducted on samples with and without the slow heating / rapid cooling cycle include the Edged Notched Disk (END) test to determine the mode I fracture toughness, Brazilian disc tests to determine tensile strength, seismic tests to determine P wave velocity, and porosity tests. Rock types tested include Coconino sandstone from northern Arizona, Sierrita and South Mountain Granite from southern Arizona, and a number of rock types from the mining district near Superior, Arizona. These include diabase, quartzite, KVS (Cretaceous Volcanic Sediments) and Skarn. Some of the diabase samples that were tested contained very prominent pyrite-quartz veins (referred to as ore veins), and other samples did not. In some of the tests, a single cycle of slow heating followed by rapid cooling was conducted at temperatures of 100, 200 and 300 °C. In other tests, multiple thermal cycles (10, 15 and 20 cycles) with a maximum temperature of only 100 °C were conducted. The low temperature, multiple cycle tests are relevant to some important rock engineering applications where rapid small to moderate changes in temperature are repeatedly applied to a rock surface, such as in deep underground mining and deep drilling for petroleum or geothermal resources.

The experimental results are important and show that rapid cooling can result in significant changes in rock properties. Not surprisingly, rapid cooling from 300 °C to room temperature resulted in significant reductions in both the fracture toughness and the tensile strength. More importantly and more surprisingly, the results showed that rapid cooling from 100 °C to room temperature also resulted in significant changes in rock properties, with two very different types of behavior depending on the rock type. In some of the rock types that were tested, the 100 °C rapid cooling results were consistent with microcrack initiation and propagation. This includes a decrease in P wave velocity, a decrease in tensile strength, and an increase in porosity. In other rock types that were tested, the 100 °C rapid cooling results were consistent with microcrack closing and crack healing. This includes an increase in P wave velocity, increase in tensile strength, and decrease in porosity. In general, the sedimentary and more heterogeneous igneous rocks showed crack growth, which included sandstone, granite, KVS and the diabase samples that contained ore veins. The metamorphic and the less heterogeneous igneous rocks showed crack closing/healing, which included skarn, quartzite and the diabase samples that did not contain ore veins.

To better understand some of the complex behavior that was exhibited, a 3D transient thermo-mechanical analysis of the experiments was conducted using the ANSYS finite element program. The rapid cooling of a 2-inch (50.8 mm) diameter disk due to blowing air was simulated, and the results give the distribution of temperature and the induced thermal stresses with time. The results indicate that within the first five minutes of rapid

cooling, there is a thin (less than 5 mm) region near the outside of the sample where large tensile stresses occur and microcracking would be expected. During the same short time period, there is a large area in the middle of the sample where lower magnitude compressional stresses occur and crack closure would be expected. Thus in some rock types, the effects of tensional cracking on the outside of the sample may be greater than the effect of compression on the inside, resulting in an overall increase in porosity, decrease in P wave velocity, etc. In other rock types, the effects of tensional cracking on the outside may be less than the effects of compression on the inside, resulting in an overall decrease in porosity, increase in P wave velocity, etc. It is reasonable to assume that the more heterogeneous and more coarse grained rock types like granite and sandstone are more likely to exhibit the first type of behavior, since coarse grained and heterogeneous rocks would contain an initial population of microcracks with larger crack lengths. On the other hand, less heterogeneous and more fine-grained rocks such as quartzite and diabase without ore veins are more likely to exhibit the second type of behavior, since the initial microcracks will be smaller.

The next section of the paper (Section A2) describes the rock sample preparation and the various thermal loading cycles that were conducted on the different rock types. Section A3 describes fracture toughness and tensile strength results of Coconino sandstone slowly heated and rapidly cooled from 100, 200 and 300 °C. Section A4 describes single and multiple thermal cycle results of testing of the remaining rock types. Section A5

describes the 3D ANSYS finite element modeling. Finally, Section A6 gives conclusions on the study.

## **A2. HEAT TREATMENT AND SAMPLE PREPARATION**

All testing utilized cylindrical discs cut from cylindrical core. In the case of samples of Coconino sandstone, Sierrita granite and South Mountain granite, 50.8 mm cylinders were first produced from rock blocks using a diamond core drill at the University of Arizona lab, followed by sawing of the samples to the desired thickness. In the case of samples of diabase, quartzite, KVS and skarn, rock core was obtained from the mining client and cut to the desired thickness at the University of Arizona. The specific dimensions (diameter and thickness) for each test are given in the table of results in the sections that follow.

A small electric furnace was used for heating the samples, which included a fully programmable digital electronic controller and display unit. The temperature inside the furnace was raised and maintained within +/- 0.1°C to minimize cracking caused by a temperature gradient [9]. The heating rate inside the furnace was maintained at 1-2 °C/min for the slow heating portion of the thermal cycle. Following the slow heating, samples were quickly transferred to a metal table and a small portable fan was used to blow room temperature air at a velocity of approximately 10 m/s. In general, rock samples were heated up to 100, 200 or 300 °C for about 2~3 hours and rapidly cooled with a fan for about 2~3 hours. Thus, one cycle of thermal loading took about 4~6 hours and the rock properties were investigated before and after thermal loading.

Initially Coconino sandstone was tested due to its relatively homogeneous rock properties.  $50.8 \times 25.4$  mm (diameter  $\times$  thickness) samples of Coconino sandstone were prepared, and two types of tests were conducted on the samples before and after thermal loading. END (Edge Notched Disc) tests were conducted on some samples to determine the mode I fracture toughness  $K_{IC}$  [10], and Brazilian disc tests were conducted on other samples to determine the tensile strength,  $T_o$ . Details on the number and type of tests conducted on Coconino sandstone are provided in the various tables in Section A3. Figure A2 shows a picture of an END test being conducted on Coconino sandstone. The results of the testing of the Coconino sandstone are described in Section A3.

Additional studies were conducted with Diabase, Quartzite, KVS (Cretaceous Volcanic Sediments, a crystal tuff) and Skarn cores taken from depths of  $1,000 \sim 2,000$  meters. These samples were tested to investigate the possible effects of rapid cooling due to mining ventilation on the stability of underground drifts. Based on a mining depth of 2000 meters, samples were slowly heated to  $100^{\circ}\text{C}$  and rapidly cooled with a fan. Due to a shortage of samples available for testing from the mining client, additional thermal testing with samples of Sierrita Granite and South Mountain Granite from Arizona were used. Three types of tests were conducted before and after the  $100^{\circ}\text{C}$  thermal loading cycles, Brazilian disc tests to determine the tensile strength, seismic velocity tests to determine the P wave velocity, and porosity tests. Details on the number and type of tests conducted on diabase, quartzite, KVS, skarn, and Sierrita and South Mountain granite are provided in the various tables in Section A4. Pictures of these different rock types are

shown in Figure A1. The results of the testing of these rock types are described in Section A4.

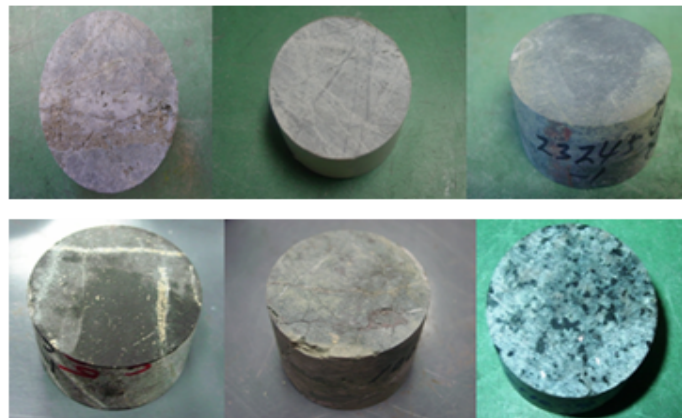


**Fig. A1.** The tested samples (left to right side): Skarn, Quartzite, Diabas (upper) and Diabase (with ore veins), KVS, Sierrita Granite (lower).

### A3. EFFECT OF RAPID THERMAL COOLING ON MODE I FRACTURE TOUGHNESS ( $K_{IC}$ ) AND TENSILE STRENGTH OF COCONINO SANDSTONE

This section describes the results of samples of Coconino sandstone subjected to rapid thermal cooling. Samples are heated to 100°C, 200°C, and 300°C at a slow heating rate of 1-2 °C/min, followed by rapid cooling to room temperature using a fan. The results show three distinct types of behavior, referred to as compaction, blunting, and expansion, as will be described.

There are many methods for determining the mode I fracture toughness,  $K_{IC}$ , and there is not a single standardized test method for mode I fracture toughness. In this study, the END (Edge Notched Disc) test was used to investigate  $K_{IC}$  as a function of thermal

loading [10]. The advantage of this test is that it is a fast and easy method using core based samples. Since the primary focus of this study is to look at changes in rock properties due to thermal loading, the END test is appropriate. Figure A2 shows an END test being conducted on a sample of Coconino sandstone. Brazilian disc testing was also conducted on some samples to determine the tensile strength. Details on the number of samples tested at each temperature are given in the tables that follow.

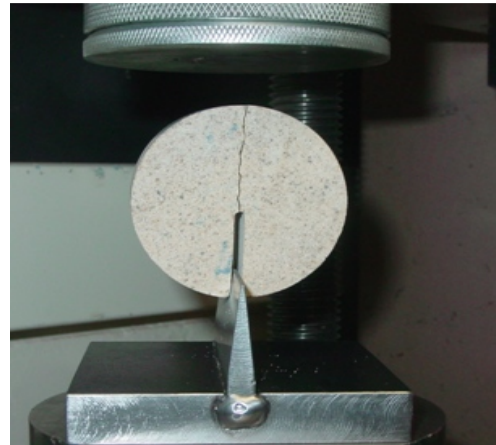


**Fig. A2. The END (Edge Notched Disc) test for mode I fracture toughness with Sandstone [10].**

Figure A3 shows the results of tests where each sample was subjected to one cycle of slow heating and rapid cooling prior to either fracture toughness or tensile strength testing. Samples were heated to either 0, 100, 200 or 300 °C (0 refers to unheated samples). 10~13 END tests were conducted at each temperature to determine  $K_{IC}$ , and 5 Brazilian samples were tested at each temperature to determine the tensile strength.

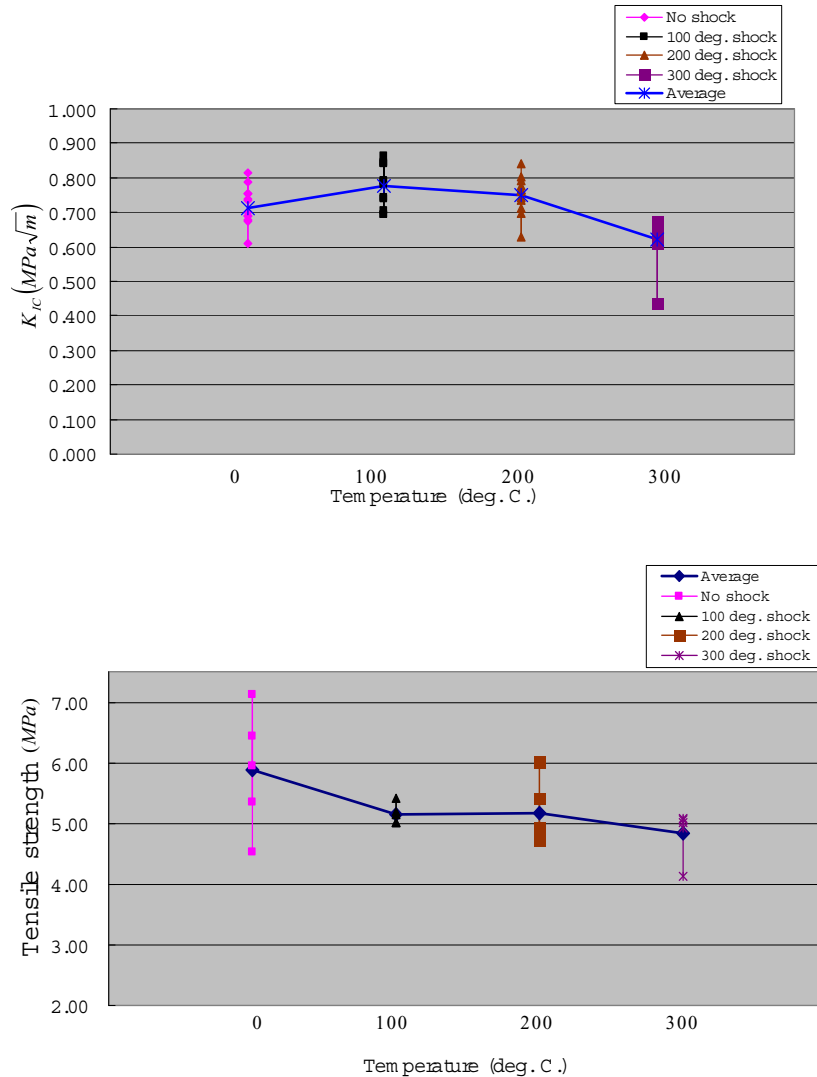


**Fig. A3. The effect of temperature on Mode I fracture toughness and tensile strength.**

The  $K_{IC}$  and tensile strength results are consistent in showing a significant drop at 300°C. The fracture toughness decreases from an unheated value of about 0.7 MPa $\sqrt{m}$  to about 0.6 MPa $\sqrt{m}$  when heated to 300 °C. The tensile strength decreases from an unheated value of about 6 MPa to a little less than 5 MPa when heated to 300 °C. However, the

$K_{IC}$  results indicate a slight increase in toughness at 100°C and 200°C, while the tensile strength results indicate a drop at 100 °C and 200°C. A preliminary interpretation of these results in terms of microcracking is given in Section A3.1. A more detailed analysis looking at the thermally induced stresses from a 3D finite element model is given in Section A5.

Additional work was carried out looking at the effects of multiple cycles of slow heating/rapid cooling of Coconino samples to just 100 °C. These results are of interest in several rock engineering applications, including the effect of mining ventilation in deep mines, and the effect of daily and seasonal temperature variations in surface rock slopes and foundations. Cyclic thermal loading was repeated 10, 15 and 20 times, and the results of  $K_{IC}$  and Brazilian testing are shown in Figure A4. At each step of cyclic thermal loading, 12 and 5 samples were tested to investigate the fracture toughness and the tensile strength, respectively. Figure A4 shows that the fracture toughness remained constant after 10 and 15 cycles but then increased after 20 cycles. The tensile strength, on the other hand, showed a slight increase after 10 cycles, followed by a moderate decrease at 15 and 20 cycles.

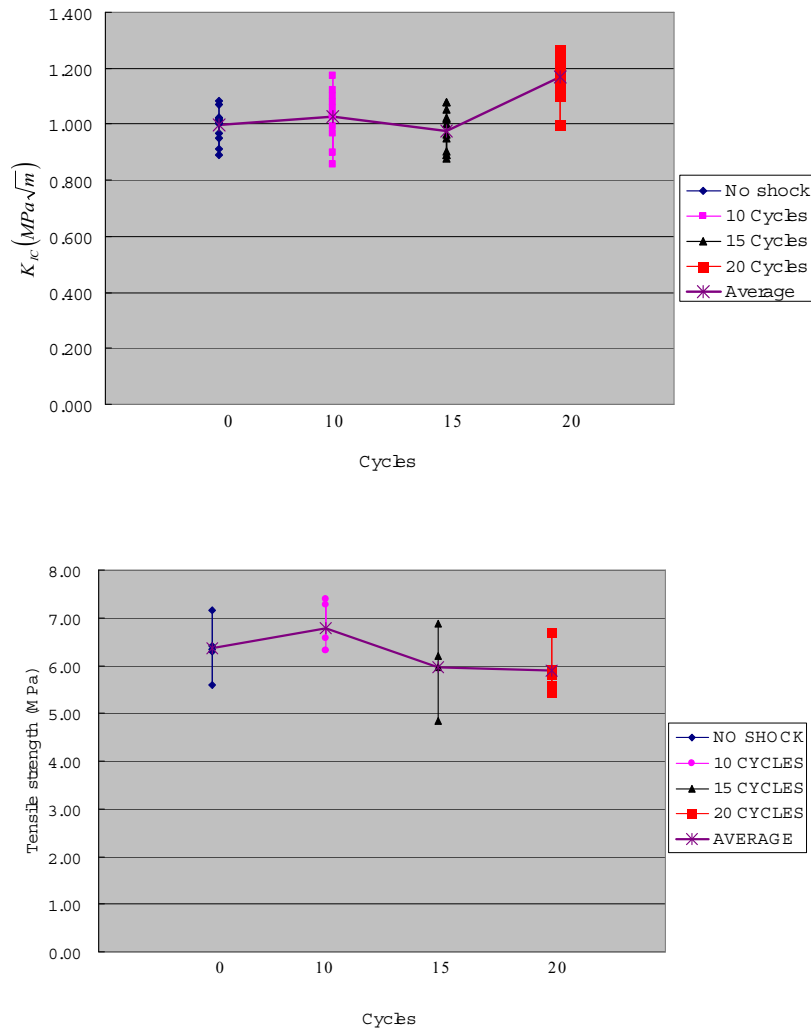


**Fig. A4. The effect of cyclic thermal shock (100°C) on Mode I fracture toughness and tensile strength**

### A3.1 Preliminary Interpretation

We consider two types of microcrack mechanisms that are occurring due to thermal loading, and the effects that these two mechanisms might have on both fracture toughness and tensile strength. The first mechanism is what we call “expansion” which is an increase in crack density or crack volume. This could occur due to the residual opening

of pre-existing cracks, or the growth or initiation of new cracks. The second mechanism is what we call “compaction” which is a reduction in crack density. Other investigators have shown that heating can result in a residual thermal strain that can occupy the crack space and thereby reduce the overall porosity [2]. Compaction could also occur due to regions of compression occurring in parts of the sample during transient heat flow, resulting in the closing of previously open cracks.

For the fracture toughness, the results suggest that a small increase in crack density might actually increase the fracture toughness while a large increase in crack density will decrease the toughness. This is supported by other investigators that have shown that microcracks can “blunt” a macrocrack tip, and increase the fracture toughness [3,11,12,13,14]. The macrocrack in this case is the precut notch in the END sample. Thus at 100°C, the effect of multiple cycles is to generate a small increase in crack density and blunt the macrocrack tip, while at 300°C, the large increase in crack density decreases  $K_{IC}$ . This can explain most of the results in Figure A3 and A4.

The tensile strength results, on the other hand, suggest that both a small and large increase in crack density can decrease the tensile strength. This is reasonable, since the Brazilian disc samples do not have a precut notch and therefore crack blunting is not possible. Thus, assuming the crack density increases, the tensile strength would always decrease because the “starter” crack would be bigger or the stress intensity factor would be larger due to the interaction with other cracks. In a similar fashion, a decrease of crack

density (compaction) could cause an increase in tensile strength and fracture toughness. This may explain the increase in tensile strength and fracture toughness at 10 cycles in Figure A4. The sketch of possible microcrack mechanisms is shown in Figure A5. These interpretations of the test results will be further analyzed along with the 3D finite element simulations of the thermal stresses given in Section A5.

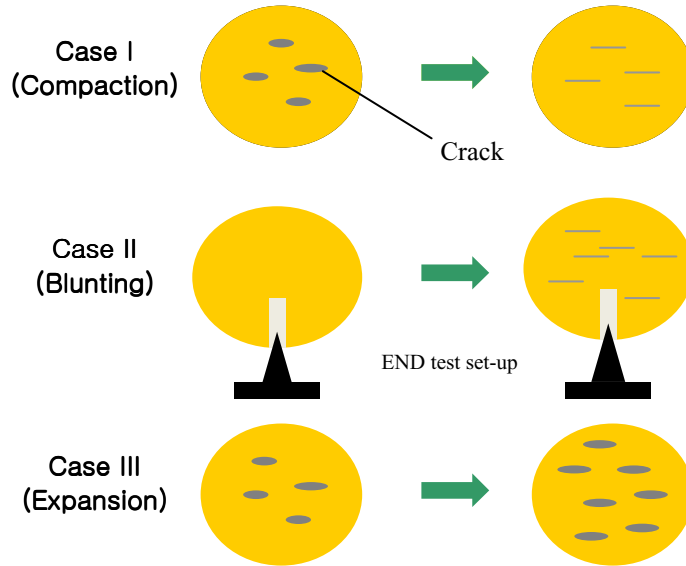


**Fig. A5. The Sketch of Possible Microcrack Mechanisms due to Rapid Cooling**

#### A4. RAPID COOLING EFFECT ON POROSITY, SEISMIC VELOCITY AND TENSILE STRENGTH IN IGNEOUS AND METAMORPHIC ROCKS

This section describes the results of thermal tests conducted with diabase, quartzite, KVS (Cretaceous Volcanic Sediments, a crystal tuff) and skarn cores taken from depths of 1,000 ~ 2,000 meters. These samples were tested to investigate the possible effects of rapid cooling due to mining ventilation on the stability of underground drifts. Based on a

mining depth of 2000 meters with an expected rock temperature between 80 and 90 °C, samples were slowly heated to 100 °C and rapidly cooled to room temperature (about 22 °C) with a fan. Due to a shortage of samples available for testing, additional thermal testing with samples of Sierrita Granite and South Mountain Granite from Arizona were used. Three types of tests were conducted before and after the 100 °C thermal loading cycles, Brazilian disc tests to determine the tensile strength, seismic velocity tests to determine the P wave velocity, and porosity tests. Fracture toughness tests were not conducted on these samples. Pictures of these different rock types are shown in Figure A1, and details on the number and dimensions of samples tested are given in the tables in this section.

The results are very interesting and revealed two distinct types of behavior. In some of the rock types that were tested, the results after slow heating / rapid cooling cycles are consistent with microcrack initiation and propagation. This includes a decrease in the P wave velocity, a decrease in the tensile strength, and an increase in the porosity. The rock types that exhibited this behavior included granite, KVS, and the subset of the diabase samples that contained ore veins. Detailed results on these rock types are given in Section A4.1. In other rock types that were tested the results after thermal loading are consistent with crack closing or healing. This included an increase in the P wave velocity, an increase in the tensile strength, and a decrease in porosity. The rock types that exhibited this behavior included quartzite, skarn and the subset of the diabase

samples that did not include ore veins. Detailed results on these rock types are given in Section A4.2.

**A4.1 Rock types that exhibited crack growth (expansion) after cyclic thermal loading**  
 Porosity and seismic testing results using Granite, Diabase (with ore veins), and KVS samples showed an increase in crack density after 5 cycles of slow heating / rapid cooling from 100°C.

Sierrita Granite samples (14 samples /  $50.8 \times 38.1$  mm) were used for the seismic tests to investigate P wave velocity change. Due to the shortage of samples, the seismic tests were not conducted with KVS and Diabase. The seismic test results are shown in Figure A6.

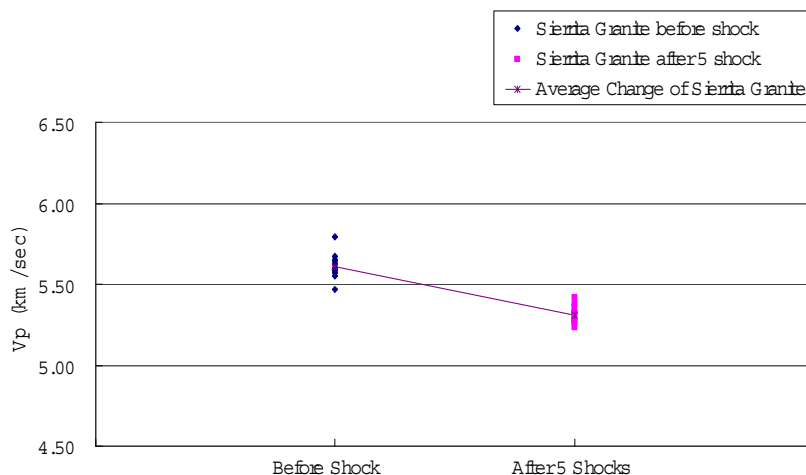


**Fig. A6. "P" wave velocity change before and after 5 cyclic thermal shocks**

The average P wave velocity decreased from 5.61 km/sec to 5.31 km/sec, a 5.3% decrease of P wave velocity and an indication that the crack density has increased. This

increase of crack density was also observed in the porosity tests shown in Table A3. Porosity results for Sierrita Granite, Diabase (with ore vein) and KVS are shown in Table A1.

**Table A1. Average porosity change before and after thermal shock**

Rock type	Porosity before shock	Porosity after 5 shocks	Increase percentage
Sierrita Granite / 5 samples (50.8 × 50.8)	0.19%	0.32%	68%
Diabase (ore vein) / 5 samples (50.8 × 50.8)	0.97%	1.56%	61%
KVS / 3 samples (50.8 × 50.8)	2.64%	3.68%	39%

Porosity results show increases of 68%, 61% and 39% for the Granite, Diabase and KVS respectively. The porosity results in Table A1 agree with the seismic results in Figure A6 indicating an increase in crack density due to rapid thermal cooling for Sierrita Granite.

A4.2 Rock types that exhibited crack healing (compaction) after cyclic thermal loading  
 Crack healing, or a decrease in crack density, was observed in some of the test results due to cyclic thermal loading. A decrease in crack density could occur due to a residual closing of cracks when subjected to compressive stresses, or a residual thermal strain that can occupy the crack space and thereby reduce the overall crack porosity [2,15]. Diabase (without ore veins), Quartzite and Skarn showed a decrease of crack density after the thermal shock in the seismic, porosity and tensile strength tests. Seismic tests were conducted with only Diabase due to the shortage of the samples, and it shows the increase of average P wave velocity in all but one sample (very top points in Figure A7). The

overall results are shown in Figure A7, showing an average increase in P wave velocity of about 6%.

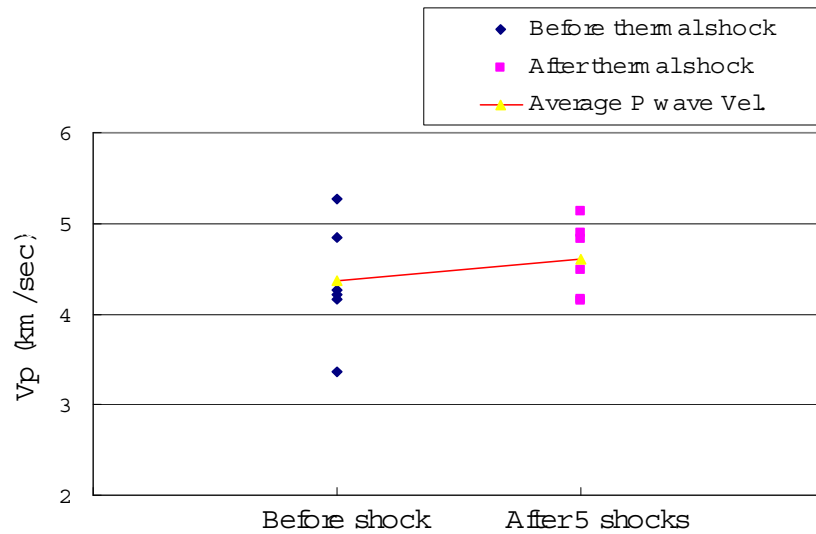


**Fig. A7. "P" wave velocity change before and after 5 cyclic thermal shocks in Diabase (no ore veins)**

It is noted that diabase samples containing prominent ore veins have shown crack growth after rapid cooling as discussed in section A4.1, but the diabase samples used in the results shown in Figure A7 do not contain ore veins. Thus, we see a characteristic difference depending on whether or not the diabase samples contain ore veins.

Crack healing was observed in the porosity tests of diabase as well as Skarn and Quartzite. Table A2 shows the test results. It is noted that Diabase samples in the porosity test are from the same cores which were used in the above seismic tests.

**Table A2. Average porosity change before and after thermal shock**

Rock type	Before thermal shock	After 5 thermal shocks	Decrease percentage
Diabase / 3 samples (63.5 × 50.8)	0.29%	0.25%	13.8%
Skarn (ore vein) / 3 samples (63.5 × 50.8)	5.82%	4.10%	25.7%
Quartzite / 3 samples (63.5 × 50.8)	1.58%	1.57%	0.6%

All samples showed a consistent decrease of porosity and Table A2 shows average porosity decreases of 13.8%, 25.7% and 0.6% for diabase, skarn and quartzite respectively. An interesting result in the table is that skarn containing ore veins shows the biggest decrease in porosity.

Standard Brazilian Disc tests were also conducted to determine the tensile strength with the same samples used for the porosity tests. The average tensile strength change of each rock type is shown in Figure A8.

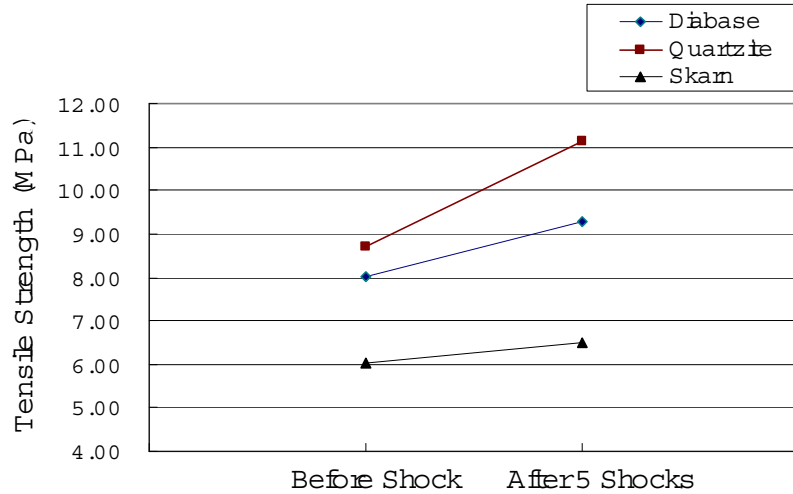
**Fig. A8. Average tensile strength change before and after 5 cyclic thermal shocks**

Figure A8 shows that the tensile strength increases by 8~28% in the tests with diabase, quartzite and skarn after 5 cyclic thermal loading, and the degree of increase is proportional to the rock strength. The summarized tensile strength test results are shown in Table A3.

From the results shown in this section we see that three kinds of tests (seismic, porosity, and tensile tests) consistently show crack closing or healing in the three rock types.

**Table A3. Average tensile strength before and after thermal shock**

Rock Type	Average Tensile Strength		Increase percentage
	Before shock	After 5 shocks	
Diabase 10 samples (50.8 × 25.4)	8.02 MPa	9.30 MPa	16%
Quartzite 11 samples (50.8 × 25.4)	8.70 MPa	11.12 MPa	28%
Skarn 9 samples (50.8 × 25.4)	6.04 MPa	6.51 MPa	8%

Crack growth during thermal loading is the usual mechanism that has been reported by many investigators [2,4,5,6,16]. Crack healing due to transient thermal loading is not commonly observed. There are several possible reasons for this due to areas of compression occurring during rapid cooling, as discussed in section A5. Another possibility is that changes in water saturation due to the thermal loading may be causing changes in the mechanical properties. In other words, the water content could have decreased due to the thermal loading, and this could result in the changes in p-wave

velocity, tensile strength and porosity. To investigate this possibility, additional testing was conducted where samples of diabase, skarn, quartzite, Coconino sandstone and Sierrita granite were fully saturated and the p-wave velocity was measured before and after saturation. The average P wave velocities before and after full saturation of the samples are shown in Table A4. Due to the shortage of samples from some rock types, only 2~3 samples are used for diabase, skarn and quartzite whereas 10~14 samples are used for Coconino sandstone and Sierrita granite.

**Table A4. Average P wave velocity change before and after saturation**

Rock Type	Before Saturation	After Saturation
Diabase / 3 samples (63.5 × 38.1)	3.81 km/sec	4.52 km/sec
Skarn / 3 samples (63.5 × 38.1)	4.26 km/sec	4.32 km/sec
Quartzite / 2 samples (63.5 × 38.1)	4.10 km/sec	4.60 km/sec
Sandstone / 10 samples (50.8 × 50.8)	3.10 km/sec	3.64 km/sec
Sierrita Granite / 14 samples (50.8 × 25.4)	5.60 km/sec	5.89 km/sec

The results in Table A4 are very consistent in showing increases in P wave velocity for all rock types due to saturation. This is also in agreement with other researchers [16]. Thus, based on the results shown in Table A4, the possible loss of saturation during the thermal tests cannot explain the apparent crack healing (velocity increase) that is

observed, since loss of saturation after heat treatment would cause P wave velocities to decrease, not increase.

#### **A5. THREE DIMENSIONAL TRANSIENT THERMO-MECHANICAL MODELING**

This section describes the simulation of the rapid cooling experiments using the ANSYS 3D finite element program [17]. A three-dimensional finite element mesh of a 2-inch diameter by 2-inch thick sample has been created and subjected to the boundary conditions shown in Figure A9a. At time  $t=0$  the sample is assumed to be at a uniform temperature of 100 °C. To simulate rapid cooling after the sample is removed from the oven and placed on the steel table, air-flow convection boundary conditions are applied to the sides and top of the sample and conduction is applied to the bottom of the sample, as shown in Figure A9a. Air flow traveling from the left to the right of the sample with a velocity of 10 m/s is assumed, resulting in a convective film coefficient that varies with position around the sides and top of the sample, as shown in Figure A10. The thermal and mechanical properties for a hard rock such as granite have been assumed, as given in Table A5. It is noted that the air velocity in Table A5 was used to estimate the Reynolds number and the Nusselt number, and the variable film coefficient shown in Figure A10 uses a basis value of  $100\text{W/m}^2\cdot\text{K}$  (multiplier = 1).

**Table A5.** The thermal and mechanical properties used in the ANSYS simulations

Properties	Values
Air Velocity (m/s)	10
Diameter (m)	0.0508
Height (m)	0.058
Elastic Modulus (Mpa)	55
Poisson's Ratio	0.25
CTE (Coefficient of Thermal Expansion)	3.57E-06
Conductivity (W/m.K)	0.972
Specific Heat (J/Kg.K)	1058
Density (Kg/m <sup>3</sup> )	2700
Ambient Temp. (deg. C. )	25
Initial Rock Temp. (deg. C.)	100

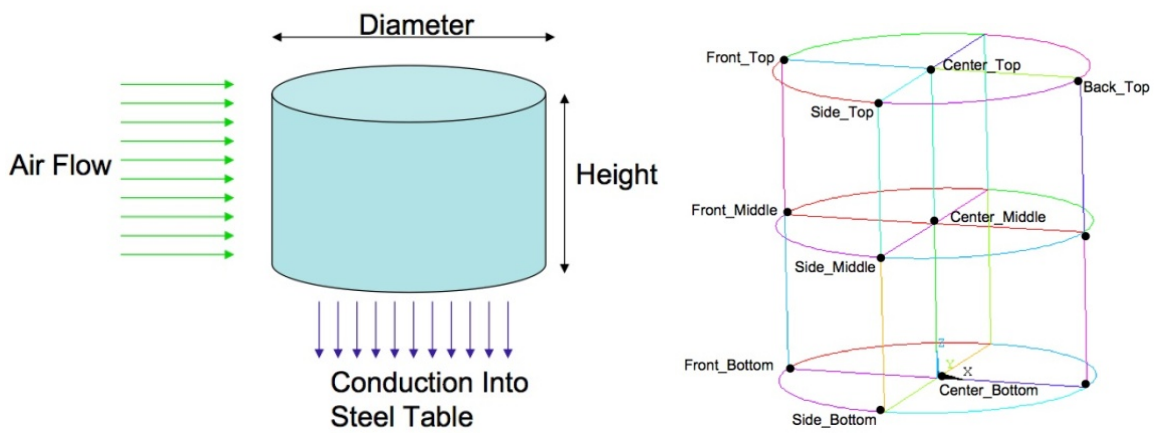


**Fig. A9.** a) boundary conditions for the ANSYS simulations, b) locations referred to in Figures A11 and A13.

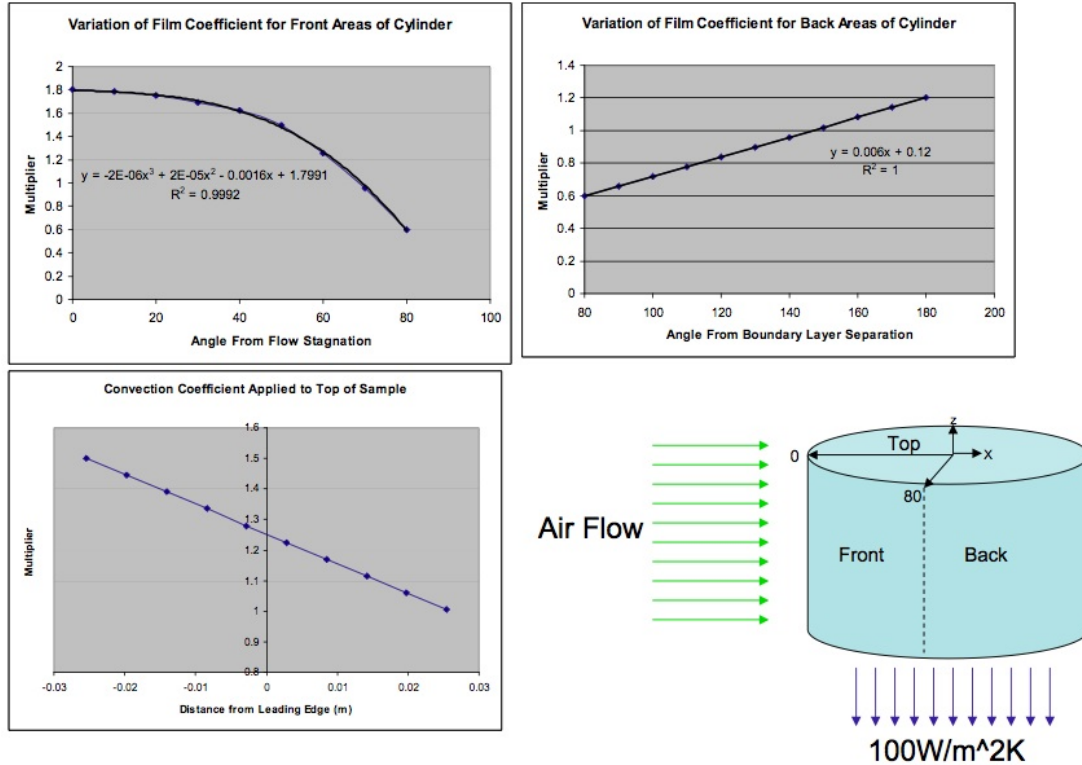


**Fig. A10.** Assumed film coefficient for various places around the specimen

The results for temperature vs. time are shown in Figures A11 and A12. Figure A11 shows plots of temperature vs. time at a number of different locations around and inside the three-dimensional sample (refer to Figure A9b for the location of the different lines on the graphs). Figure A11 shows that the most rapid cooling occurs at the “front-bottom” and “front-top” locations, and the least rapid cooling occurs at the “center-middle” location, as expected. The generation of thermal stresses is driven by the transient distribution of temperatures within the sample, and Figure A11a shows that the largest temperature change, and thus the largest thermal stresses, occurs at around 100 seconds. At 100 seconds the temperature at the center of the specimen is still above 98 °C while the temperature at the front-bottom has cooled to about 42 °C. Figure A12 shows the

three-dimensional temperature distribution at 105 seconds. It shows rapid cooling at the side and top boundaries, particularly the top and bottom corners of the sample.

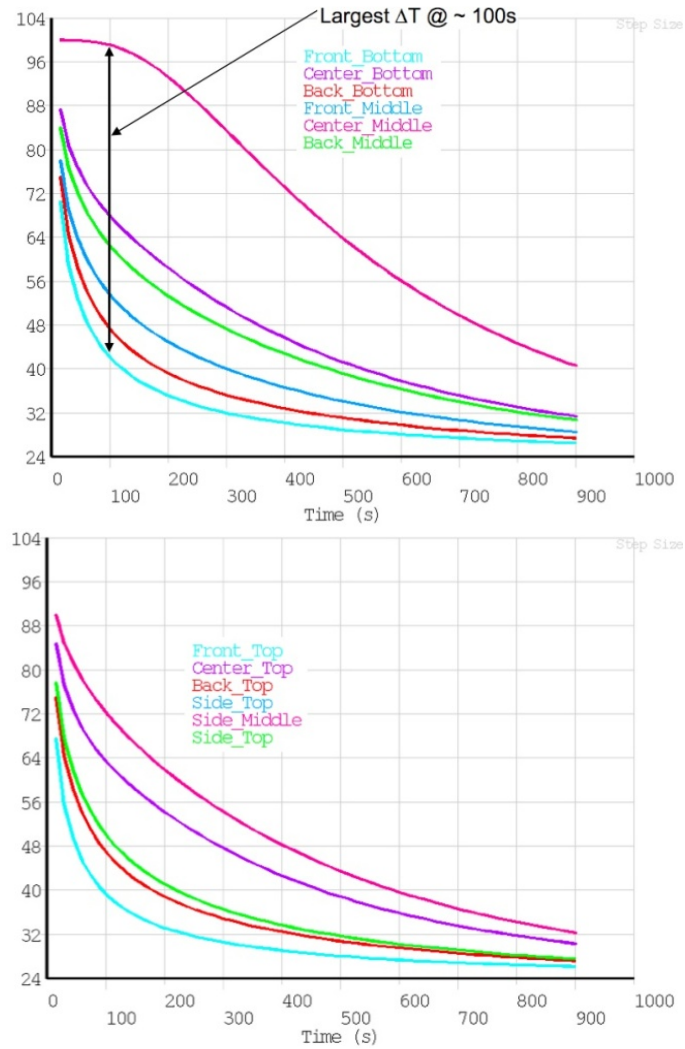


**Fig. A11.** Temperature (°C) vs. time for various places in the specimen (refer to Figure A9b).

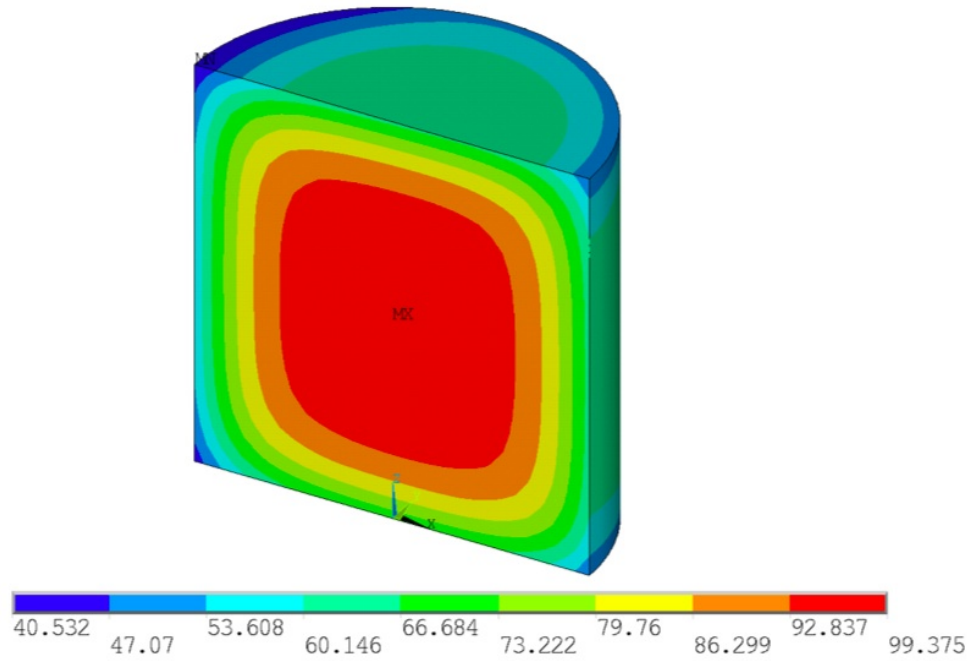


**Fig. A12. Distribution of temperature (°C) at 105 seconds.**

The results for maximum principal stress vs. time are shown in Figures A13 and A14. Figure A13 shows plots of maximum principal stress vs. time at a number of different locations around and inside the three-dimensional sample (refer to Figure A9b for the location of the different lines on the graphs). Figure A13 shows that tensional stresses are occurring on the outside of the sample and compressional stresses are occurring in the center of the sample. The maximum tensional stresses are occurring at around 100 seconds, and Figure A13 shows that at two locations, the front-middle and back-middle locations, the tension at 100 seconds exceeds 7 MPa. Figure A14 shows the three-dimensional distribution of maximum principal stresses at 105 seconds. It shows that at 105 seconds, the zone of tension is a thin skin with a thickness of 0.2-0.3 inches (5.1-7.6

mm). The zone of tension that exceeds 5 MPa is very thin, with a thickness of 5 mm or less.

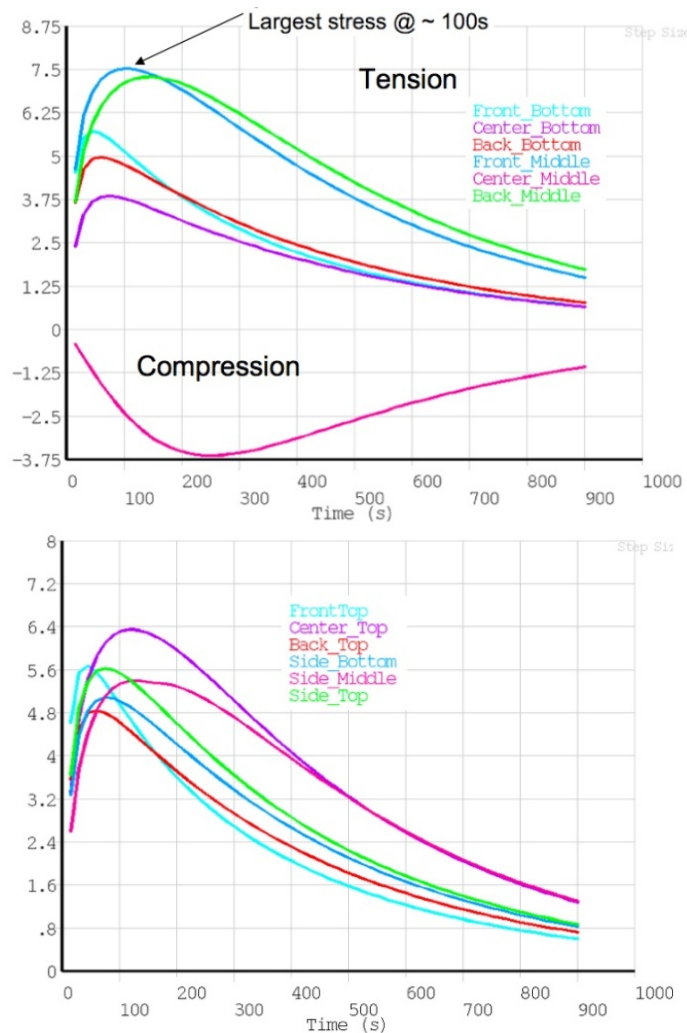


**Fig. A13. Maximum principal stress (MPa) vs. time for various places in the specimen (refer to Figure A9b).**

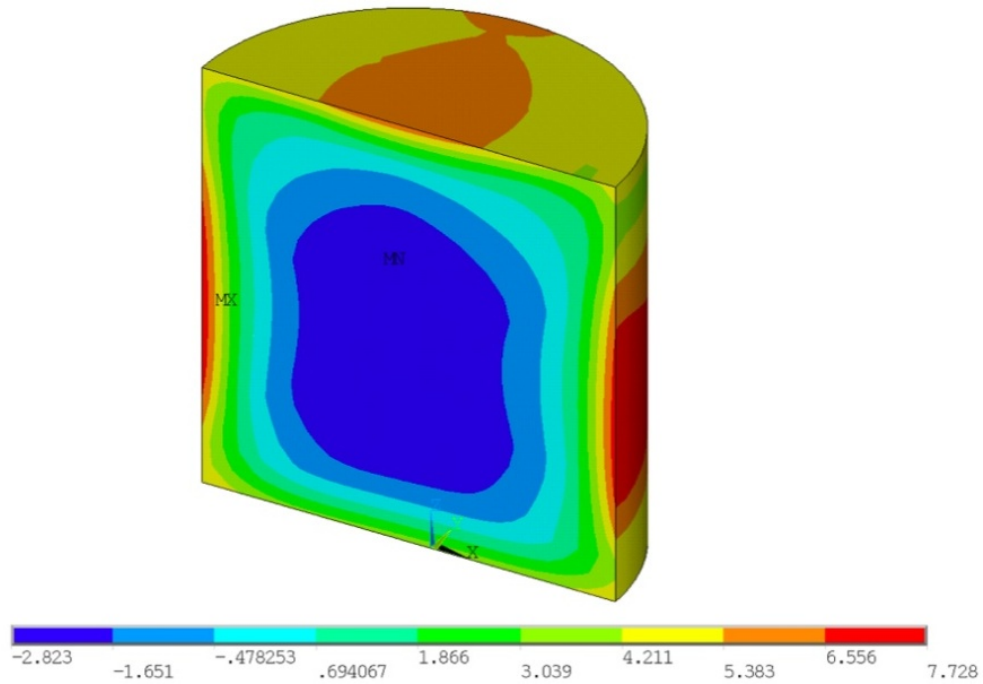


**Fig. A14. Distribution of maximum principal stress (MPa) at 105 seconds.**

The thermal stress results presented in Figures A13-A14 support the experimental results.

In general the ANSYS results show that in the first five minutes or so of rapid cooling, a thin zone of high tensional stresses are occurring on the outside of the sample, and a core of compression is occurring near in the center portion of the sample. Figure A13 shows that tensional stresses above 6 MPa are occurring in some locations for five minutes. Based on fracture mechanics, for a crack of length  $2a$  subjected to a tensional stress  $\sigma$ , the mode I stress intensity factor is given by [18]:

$$K_I = \sigma \sqrt{\pi a}$$

and the crack velocity due to subcritical crack growth is given by:

$$\text{crack velocity} = A \left[ \frac{K_I}{K_{IC}} \right]^n$$

where  $K_{IC}$  is the fracture toughness and A and n are subcritical crack growth properties. For Coconino sandstone, using the  $K_{IC}$  value of 0.7 MP $\sqrt{\text{m}}$  from Figure A3 and A and n values of 0.018 m/s and 36 from Ko and Kemeny (2011) [19], and assuming a tension stress of 6.5 MPa is applied to a 4 mm crack for 5 minutes, the equation above predicts an increase in crack length of about 4.4%. Even though this is small, the results indicate that some tensional cracking at the outside of the sample could occur in rocks that contain microcracks with lengths on the order of millimeters, as would be expected in granite, sandstone and other similar rocks. For fined grained volcanic or igneous rocks with microcracks on the order of 0.1 mm, crack growth would not be expected. For example, using the same properties but considering a 0.4 mm rather than a 4 mm crack length, the increase in crack length predicted from subcritical crack growth is only  $4 \times 10^{-17}\%$ .

The compressive stresses in the center of the sample are expected to result in crack closure. From fracture mechanics, the closure at the center of a crack of length 2a under a compressional stress  $\sigma$  is given by [18]:

$$\text{crack closure} = \frac{4\sigma a}{E}$$

Figure A14 shows that compressive stresseses on the order of 2.5 MPa are occurring in the center of the sample. Assuming a 4 mm crack under a stress of 2.5 MPa and using

the E for Coconino sandstone from Ko and Kemeny (2011) of 24 GPa [19], the equation above predicts a crack closure of about  $8 \times 10^{-7}$  m. Again, even though this is a very small displacement, it represents about 0.04% of the crack length and is expected to result in some crack healing based on [20] and others.

It is interesting to examine at the results of specific tests after thermal loading, in light of the results presented above. The general interpretation would be that in the case of sedimentary and coarser grained igneous rocks, there is a thin zone of microcracking on the outside of the sample and thick zone of crack closure at the center of the sample. In the case of fine-grained rocks, the zone of microcracking would not exist. The P wave velocity tests measure wave propagation from the top to the bottom of the sample, and thus the wave speed is a measure of the average effective elastic properties through both the regions subjected to tension and compression. Similarly, the porosity tests measure the average porosity through the sample, including the sections subjected to tensional and compressional stresses. The Brazilian and END tests are more complicated to interpret. Crack growth in the Brazilian test normally initiates near the center of the circular disk and propagates towards the ends. The center of the disk is complex mixture of the region subjected to tension on the outside and the region subjected to compression on the inside. Similarly, in the END test, the fracture toughness is related to the stress to initiate crack growth at the notch tip, which is located near the center of the disk, which is again a complicated mixture of the region on the outside that was subjected to tension and the region on the inside subjected to compression. Thus the discussion of crack blunting

given in Section A3 is relevant to the part of the crack tip on the outside but not the part of the crack tip in the compressive region. A final issue has to do with the slow heating part of the thermal cycle. In the tests heated to 200 and 300 degrees C it is possible that some microcracking occurred, particularly in the course grain igneous rocks such as granite.

## A6. CONCLUSIONS

A set of laboratory experiments and 3D numerical modeling was conducted, looking at the effects of rapid thermal cooling on mechanical properties. Rapid thermal cooling occurs in several important mining and geotechnical engineering applications, including the ventilation of mines at deep depth and deep drilling. Tests were conducted by slowly heating samples of granite, sandstone and other rocks in an oven, followed by rapid cooling with a fan. Samples were cooled from oven temperatures of 100, 200 and 300°C, and testing to evaluate the changes in mechanical properties included END tests to determine the fracture toughness, Brazilian disc tests to determine the tensile strength, and P-wave velocity and porosity tests. The results were very interesting and demonstrated that rapid cooling from low to moderate temperature changes can result in significant changes in mechanical properties. The rapid cooling results from 100°C were unexpected and showed two very different types of behavior depending on the rock type. In some of the rock types that were tested, the 100 °C rapid cooling results were consistent with microcrack initiation and propagation. This includes a decrease in P wave velocity, a decrease in tensile strength, and an increase in porosity. In other rock

types that were tested, the 100 °C rapid cooling results were consistent with microcrack closing and crack healing. This includes an increase in P wave velocity, increase in tensile strength, and decrease in porosity. The results were explained by conducting 3D thermo-mechanical modeling using the ANSYS finite element program. The ANSYS results indicated that within the first five minutes of rapid cooling, there is a thin (less than 5 mm) region near the outside of the sample where large tensile stresses occur and microcracking would be expected. During the same short time period, there is a large area in the middle of the sample where lower magnitude compressional stresses occur and crack closure would be expected. In the more heterogeneous and coarse grained rocks that were tested, it was shown that time-dependent crack growth could occur on the outside of the sample and dominate any closure occurring on the inside of the sample, resulting in an overall increase in porosity, decrease in P wave velocity, etc. In the less heterogeneous and fine-grained rocks that were tested, it was shown that tension cracking on the outside could not occur, while crack closure on the inside could still occur, resulting in an overall decrease in porosity, increase in P wave velocity, etc.

#### ACKNOWLEDGEMENTS

This work is supported by Rio Tinto's Resolution Copper Company.

## References

- [1] Kemeny, J., Apted, M., and Martin, D. 2006. Rockfall at Yucca Mountain due to thermal, seismic, and time-dependence. *In Proceedings of International High Level Radioactive Waste Management Conference, Las Vegas, NV, 2006.*
- [2] Zomeni, Zomenia 1997. Thermally induced microfracturing in Quartzite, *Masters of Science dissertation, Mining and Geological Engineering, the University of Arizona, Tucson, 1997.*
- [3] Meredith, P.G. and Atkinson, B.K. 1985. Fracture toughness and subcritical crack growth during high-temperature tensile deformation of Westerly granite and Black gabbro, *Physics of the Earth and Planetary Interiors*, Vol.39, pp 33-51.
- [4] Glamheden, R., Lindblom, U. 2002. Thermal and mechanical behavior of refrigerated caverns in hard rock, *Tunnelling and Underground Space Technology*, Vol. 17, Issue 4, pp.341-353
- [5] Bellopede, R., Ferrero, A.M., Manfredotti, L., Marini, P., Migliazza, M., 2006. The effect of thermal stresses on the mechanical behavior of natural building stones, *Fracture and Failure of Natural Building Stones*, Part II, pp. 397-425
- [6] Yavuz, H., Altindag, R., Sarac, S., Ugur, I., Sengun, N.. 2006. Estimating the index properties of deteriorated carbonate rocks due to freeze-thaw and thermal shock weathering, *Int. J. Rock Mech. Min. Sci.*, Vol. 43, pp 767-775
- [7] Kingery, W. D. 1955. Factors affecting thermal stress resistance of ceramic materials, *Journal of The American Ceramic Society, Vol. 38, No 1.*

- [8] Wikipedia
- [9] Boley, B. A., Weiner, J. H. 1960. Theory of Thermal Stresses, *John Wiley & Sons, Inc.*
- [10] Donovan, J. G. 2006. Fracture toughness based models for the prediction of power consumption, product size, and capacity of jaw crushers, *Doctor of philosophy dissertation, Mining and Mineral Engineering, Virginia Tech, Blacksburg, 2006.*
- [11] Balme, M.R., Rocchi, V., Jones, C., Sammonds, P.R., Meredith, P.G., Boon, S. 2004. Fracture toughness measurements on igneous rocks using a high-pressure, high-temperature rock fracture mechanics cell, *Journal of Volcanology and Geothermal Research*, Vol 132, pp 159-172.
- [12] Nasseri, M.H.B., Schubnel, A., Young, R.P. 2007. Coupled evolutions of fracture toughness and elastic wave velocities at high crack density in thermally treated Westerly granite, *Int. J. Rock Mech. Min. Sci.*, Vol 44, pp 601-616.
- [13] Darot, M., Gueguen, Y., Benchemam, Z., Gaboriaud, R. 1985. Ductile-brittle transition investigated by micro-indentation: Results for quartz and olivine. *Physics of the Earth and Planetary Interiors*, Vol.40, pp 180-186.
- [14] Gordon, J.E., 1976. The New Science of Strong Materials. 2<sup>nd</sup> ed. *Penguin, Harmondsworth*, pp 287.
- [15] Kim, K. M. and Kemeny, J. 2008. Effect of thermal loading on compressional wave velocity, mode I fracture toughness and tensile strength, *In proceedings of American Rock Mechanics Association Conference, San Francisco, CA*
- [16] Schell, J. H. 1996. Physical properties of rocks - Fundamentals and principles of petrophysics, *Handbook of geophysical exploration*, Vol. 18, Elsevier Science Inc.

- [17] Srinivas, Paleti; Sambana, Krishna Chaitanya; Datti, Rajesh Kumar 2010. Finite element analysis using ANSYS 11.0, *PHI Learning Private Limited, New Delhi*.
- [18] T. Kundu, 2008, Fundamentals of fracture mechanics, *CRC press*
- [19] Ko, T. Y., and J. Kemeny. 2011. Subcritical crack growth in rocks under shear loading, *J. Geophys. Res.*, 116, B01407, 25 PP.
- [20] Meglis, I. L., Greenfield, R. J., Engelder, T., and Graham, E. K., 1996, Pressure dependence of velocity and attenuation and its relationship to crack closure in crystalline rocks: *J. Geophys. Res.*, 101, 17 523–17 533.

## APPENDIX B: SITE-SPECIFIC BLASTING MODEL FOR MINE-TO-MILL OPTIMIZATION

Kim, K. M.<sup>a,b</sup> and Kemeny, J.<sup>b</sup>

<sup>a</sup>*ASARCO (Gropo Mexico) LLC, Tucson, AZ, U.S.A.*

<sup>b</sup>*The University of Arizona, Tucson, AZ, U.S.A.*

2011 TRANSACTIONS OF THE SOCIETY OF MINING,  
METALLURGY, AND ENGINEERING, Vol. 330, pp. 543-548

# SITE-SPECIFIC BLASTING MODEL FOR MINE-TO-MILL OPTIMIZATION

**Kim, K. M.<sup>a,b</sup> and Kemeny, J.<sup>b</sup>**

<sup>a</sup>*ASARCO (Gropo Mexico) LLC, Tucson, AZ, U.S.A.*

<sup>b</sup>*The University of Arizona, Tucson, AZ, U.S.A.*

## Abstract

A site-specific blasting model has been developed for the Asarco Mission mine. The main inputs to the model are the in-situ block size (F80), the post-blast fragmentation (P80) and the intact tensile strength (To). The output from the model is the specific blast energy ( $E_{SE}$ ). Modern techniques are being used to obtain the input parameters for the site-specific blast fragmentation model. In particular, image processing software is used to obtain both the in-situ block size and the post-blast fragmentation, and the Schmidt hammer is used to obtain the tensile strength at numerous locations throughout the rock mass.

An initial model was developed using five test shots in one area of the mine that contains Argillite and is relatively homogeneous. This also included calibrating Schmidt hammer readings against actual Brazilian tensile measurements. The model for Argillite will be updated as more tests are conducted, and the model will be extended to the other four primary rock types at the Asarco Mission mine.

## B1. Introduction

Blast fragmentation models play an important role in modern mining operations. Today blast fragmentation is optimized not only for material haulage but for comminution and mineral processing as well. Also, it is now recognized that in order to achieve highly accurate predictions, blast fragmentation models must be “tuned-up” for a specific rock type or area within a mine. Finally, in modern blast fragmentation modeling, the parameters must be easily attained at numerous locations throughout the rock mass.

In this paper the authors describe a blast fragmentation modeling approach that is being incorporated into mine-to-mill optimization at the ASARCO Mission mine complex in Southern Arizona. In this approach, site-specific empirical models are developed for the main rock types in the mine. The main inputs to the model are the in-situ block size (F80), the post-blast fragmentation (P80) and the intact tensile strength ( $T_0$ ). F80 refers to the 80% passing size in rock mass block size prior to blasting, and P80 refers to the 80% passing size of the post-blast fragmentation. F80 and P80 are assumed to be representative values for the in-situ block size and the post-blast fragmentation, respectively. The output from the model is the specific blast energy ( $E_{SE}$ ). The importance of the in-situ block size can be seen in Fig. B1.



**Figure B1. Blasting in a quarry (Kim, 2006)**

Fig. B1 shows that most rock fragmentation occurs due to movement and breakage along the in-situ blocks, which involves cracking and sliding along preexisting discontinuities, and the failure of intact rock between discontinuities. Also, recent studies by Donovan (2006) and Kim (2006) show the importance of tensile or mode I breakage rather than compressive breakage in the blasting process. The tensile strength rather than the mode I fracture toughness is used in the model because it can be obtained in the field without laboratory testing (Donovan, 2006; Whittaker, Singh, and Sun, 1992; Zhang, 2002).

Modern techniques are being used to obtain the input parameters for the site-specific blast fragmentation model. In particular, image processing software is used to obtain both the in-situ block size and the post-blast fragmentation, and the Schmidt hammer is used to obtain the tensile strength at numerous locations throughout the rock mass.

This study is the part of an on-going mine-to-mill optimization project at the ASARCO Mission mine. The Super Pit in the ASARCO Mission mine is selected for initial testing due to its relatively homogeneous rock type. Eventually the models will be refined and applied to all rock types at the Mission mine.

## **B2. Site-Specific Blasting Model**

The site-specific blast model is obtained for a specific area in the mine and relates the specific explosive energy ( $E_{SE}$ ), blast fragmentation (P80), bench face block size (F80), and intact rock tensile strength ( $T_o$ ). Each of these parameters is described in the following sections.

### B2.1 In-situ Block Size (F80) of the Bench Face

One of the innovations is to use image analysis software that is normally used for post-blast fragmentation to estimate the in-situ block size. This had been studied previously by Kim (2006) using the Split-Desktop program in a hard rock quarry. Fig. B2 shows freshly blasted bench faces in a hard rock quarry and in the Mission copper mine.



**Figure B2. Bench face images in a quarry (left) and in Mission copper mine (right)**

The rock mass in the quarry image is high strength diabase containing numerous discontinuity sets. The rock mass in the Mission copper mine image is a medium strength Argillite and also contains numerous discontinuity sets. In both cases the discontinuity sets control the post-blast fragmentation. Even though the appearance is different, it was found that the Split-Desktop program (Split Engineering, 2010) does a good job of delineating the rock blocks in both cases. Fig. B3 shows an example of in-situ rock block delineation using the Split-Desktop program.

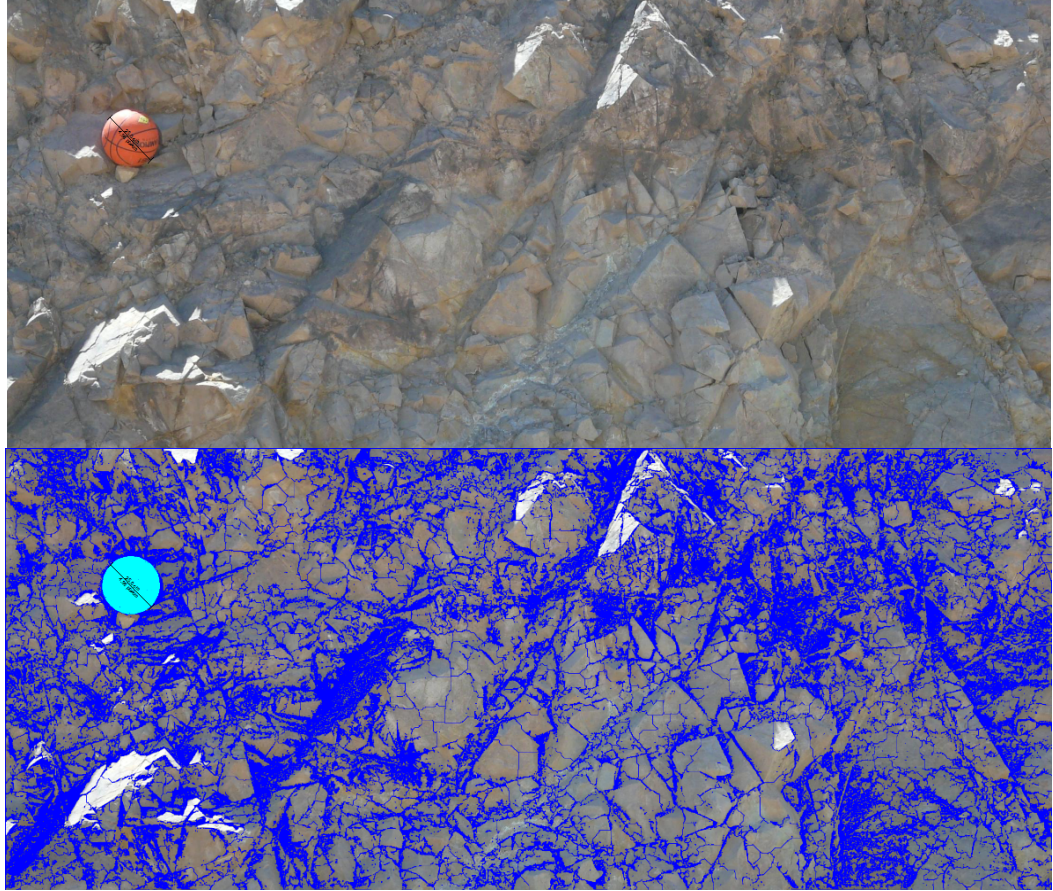


**Figure B3. The example of the analyzed image of the bench face by using Split-Desktop**

The image analysis program gives a complete size distribution of the rock blocks, and it was found that from the complete distribution, the F80 (80% passing size) is a good representation for the in-situ block size.

This method for determining the in-situ block size produces consistent and accurate results that are far less influenced by human bias than those produced by manual methods. Also, results can be obtained in a timely fashion compared with manual

scanline surveying, and results can be obtained from parts of the slope that would be inaccessible to manual measurements.

## B2.2 Schmidt Hammer Hardness (Q) and Tensile Strength ( $T_o$ )

A Schmidt hammer is used to estimate the intact tensile strength. A SilverSchmidt Schmidt hammer is used that gives the Q rebound coefficient for the Schmidt Hammer Hardness (SHH) rather than the traditional rebound value I, which is an index of surface hardness. Studies have shown that Q is less dependent on the impact direction and the internal friction (Demirdag, 2008; SilverSchmidt Operation Instruction, 2007). The relationship between SHH and tensile strength is determined by conducting Schmidt hammer tests along with laboratory Brazilian tests, as described below.

The use of the Schmidt hammer to estimate rock properties has been problematic and inaccurate in the past. A major reason for this has been universal conversion tables or charts that are used across all rock types. In this study it has been found that the use of a conversion formula between Q and tensile strength can be very accurate within a given rock type in the Mission mine but not accurate when used across many rock types.

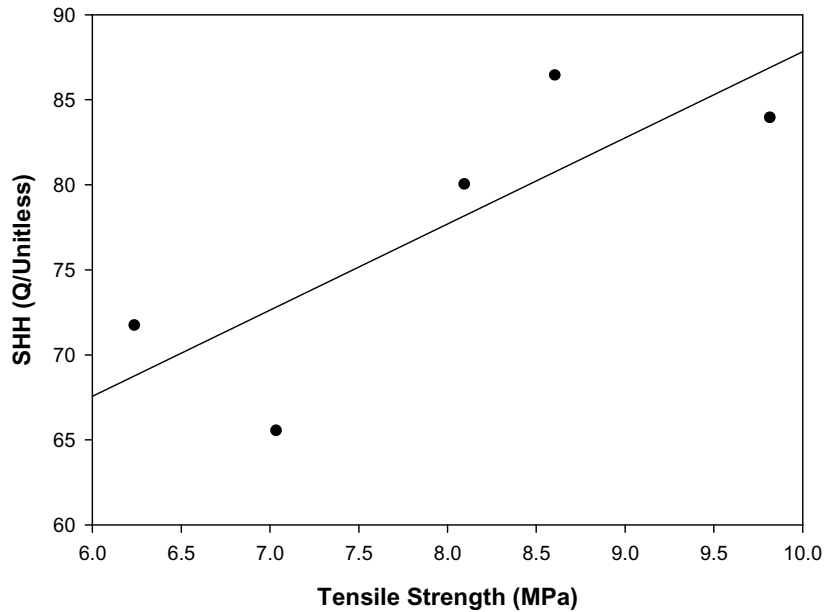


**Figure B4. Schmidt hammer hardness (Q) and the tensile strength for Argillite**

Most of the rock (90%) in the Super Pit in the Mission mine is Argillite, and Brazilian Disc tests have been conducted with about 60 disc samples from five blocks of Argillite from the mine. Fig. B4 shows the relationship between Q and tensile strength, and the following empirical model is derived.

$$T_o = 0.2 \times Q - 7.33 \quad (1)$$

Where,

$T_o$  is the tensile strength (Mpa).

Q is the Schmidt Hammer Hardness (unitless)

The model in Equation (1) is used in this paper and additional tests will be conducted to refine the model in the future.

In addition, tests on three additional rock types have been conducted to determine relationships between SHH and tensile strength for those rock types. Fig. B5 shows the relationship in these three rock types. For the three rock types in Fig. B5, a total of 45 Brazilian Disc tests were conducted, with about 15 Disc tests conducted on each rock type.

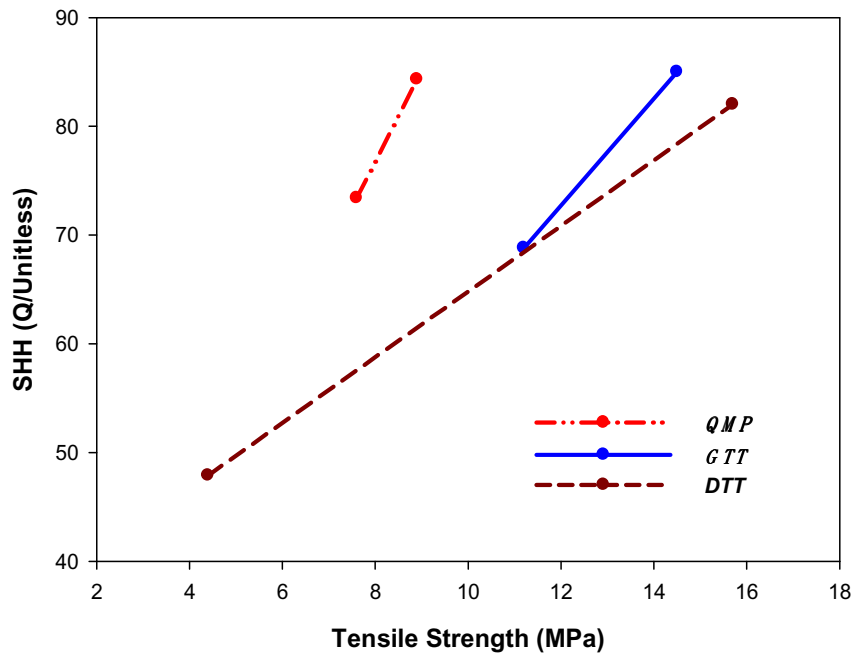


**Figure B5. Schmidt hammer hardness (Q) and the tensile strength for Mission rock types**

Where,

QMP is Quartz Monzonite Porphyry.

GTT is Garnet Tactite.

DTT is Diopside Tactite.

Looking at the results in Figs. B4 and B5, it is very apparent that good relationships between SHH and To exist for the individual rock types but no universal relationship exists across all four rock types.

### B2.3 Specific Explosive Energy ( $E_{SE}$ )

To fragment a unit volume or mass of rock, the needed blast energy is the specific explosive energy ( $E_{SE}$ ) with the unit of KJ/t (Kcal/t) (Rustan, 1998). It is noted that “t” is the metric ton. The specific explosive energy is affected by the blasting pattern (explosives amount, hole length and explosive distribution along the hole, bench height, burden, spacing, hole diameter, rock specific gravity, and the type of explosives), and consequently,  $E_{SE}$  can be assumed to represent the blasting pattern as given by Equation 2 below:

$$E_{SE} = \frac{\text{Ave. Explosive Energy per hole KJ (Kcal)}}{\text{Height (H)} \times \text{Burden (B)} \times \text{Spacing (S)} \times \text{S.G. (ton)}} \quad (2)$$

$E_{SE}$  considers the most important aspects of the explosive, the average blast energy and the average volume affected by this energy. In the next section, Equation (2) is used to calculate  $E_{SE}$  for 5 test shots that are used to calibrate the site-specific blasting model. Once calibrated, the site-specific blasting model can be used to determine an optimal  $E_{SE}$ , and thus optimal values for burden, spacing and energy per hole, to achieve a desired fragmentation.

## B2.4 Data Collection and Analysis

The post-blast fragmentation is determined from special cameras on the shovels and using image processing software (Split, 2010). The 80% passing size, P80, is used as the representative index of the post-blast fragmentation in this study.

Data on post-blast fragmentation (P80), in-situ block size (F80), tensile strength (To) and blast energy ( $E_{SE}$ ) were collected from five shots in the Super Pit in the Mission mine, as shown in Table B1. The site-specific blasting model is developed based on this data. Due to the relatively homogeneous rock type (90% of rock is Argillite) in that pit, the tensile strength did not vary significantly between the five shots. Based on this, it was decided that an initial model would be developed without tensile strength being a variable, and the average tensile strength of  $7.86 \pm 0.34$  MPa, was used.

**Table B1. Data collection from five shots in the Super Pit**

Blastings	Ese, KJ/t (Kcal/t)	F80, cm (inches)	P80, cm (inches)
#1	1063 (254)	32.6 (12.8)	16.8 (6.6)
#2	653(156)	19.7 (7.8)	16.8 (6.6)
#3	603(144)	32.6 (12.8)	20.3 (8.0)
#4	1645(393)	32.6 (12.8)	11.9 (4.7)
#5	1210(289)	19.7 (7.8)	11.3 (4.5)

A second simplification was made with regards to the in-situ block size (F80). For a given area, the bench face is classified as either “blocky” or “jointed”, and the average values for blocky and jointed of 32.6cm (12.8 inches) and 19.7cm (7.8 inches) respectively, were used, as shown in Table B1.

Based on the data in Table B1, following empirical site-specific blast model has been derived.

$$E_{SE} = 8147.1 F_{80}^{0.768} P_{80}^{-1.718} \quad (3)$$

Where,

$E_{SE}$  is the specific blast energy in KJ per 90one.

$F_{80}$  and  $P_{80}$  are 80% passing size from the muckpile and the bench face in centimeters.

This empirical formula is similar to the formula used by Kim (2006) for crusher specific energy. The formula in Kim (2006) used the reduction ratio between the 80% passing crusher feed size and the 80% passing crusher product size. Here the pre-blast block size and the post blast fragmentation are considered separately to allow for increased adjustability in the resulting regression. Excel regression was used to determine the three constants in the model, and the effect of tensile strength was not determined due to relatively constant tensile strength in the test area. In the future, additional tests will be conducted in different rock types and the following model will be used:

$$E_{SE} = A F_{80}^B P_{80}^C T_o^D \quad (4)$$

Where A, B, C and D are fitting constants.

There are four factors which should be considered for the assessment of rock blasting (Cunningham, 1987; JKMRC, 1996; Kim, 2006). Those are rock density, mechanical

strength, elastic properties, and structure. In the usual blast model, Uniaxial Compressive Strength (UCS) and Young's Modulus (E) are used to represent mechanical strength and elastic modulus, respectively. In the suggested model, the tensile strength measured by the Schmidt test is used as the basic rock strength property. We note that there are many other blasting and rock parameters not considered in the model such as discontinuity orientation, discontinuity fill, blast delay between holes, and many other variables. The approach here is to focus on what is considered to be the most important variables and develop a sound approach based on these variables.

When Equation 2 is combined with Equation 4, the following equation for the burden and spacing is produced:

$$B \times S = \left( \frac{P_{80}^C}{A \times F_{80}^B \times T_o^D} \right) \times \left( \frac{Ex.}{S.G. \times H} \right) \quad (5)$$

The burden and spacing are two of the most important factors because other factors in the blast pattern are either difficult to change or fixed for a given bench height and hole diameter at a specific blast site. Eq. 5 is used to calculate the optimal burden and spacing to obtain a desired post-blast fragmentation distribution (P80).

### B3. Estimating the Complete Size Distribution Curve

In addition to estimating the burden and spacing to produce a desired 80% passing size (P80), it is sometimes of interest to estimate the entire size distribution curve for a given

P80 value. Here it is assumed that the complete size distribution will follow the Rosin-Rammler distribution, which is a common distribution function for muck pile fragmentation (Chung, 2000; Kuznetsov, 1973; Lilly, 1986; Spathis, 2004). The Rosin-Rammler cumulative distribution function is given by:

$$\Phi_{(X)} = 1 - R_{(x)} = 1 - \exp\left[-\left(\frac{x}{x_c}\right)^N\right] \quad (6)$$

$$R_{(x)} = \exp\left[-\left(\frac{x}{x_c}\right)^N\right]$$

Where,

$\Phi_{(X)}$  is the distribution function.

(The total relative volume fraction not larger than x)

$X_c$  is the Characteristic Size.

N is the Uniformity Index.

$R_{(x)}$  is the fraction of material retained on screen.

There are two unknown parameters in the Rossin-Rammler distribution,  $X_c$  and N, and once these parameters are known, then the complete size distribution can be estimated. Given a desired fragmentation P80, the two parameters  $X_c$  and N cannot be determined without making an additional assumption. The additional assumption is made about N based on the observed relationship between P50 and P80.

The Rosin-Rammler model predicts a certain relationship between P50 and P80 as shown in Equation 7 below:

$$\frac{P50}{P80} = \left(\frac{\ln 0.5}{\ln 0.2}\right)^{1/N} \quad (7)$$

Where P50 and P80 are the 50% and 80% passing sizes, respectively. Data from both a quarry and the Mission copper mine indicate that the ratio P50/P80 falls within a narrow range and based on this value, N can be estimated from Equation 7.

**Table B2. P50 and P80 in the Super Pit in ASARCO Mission**

P50, cm (inches)	F80, cm (inches)
7.9 (3.1)	16.8 (6.6)
7.1 (2.8)	15.5 (6.1)
8.9 (3.5)	17.5 (6.9)
7.4 (2.9)	16.8 (6.6)
8.4 (3.3)	16.8 (6.6)
5.3 (2.1)	13.0 (5.1)
6.1 (2.4)	13.7 (5.4)
5.8 (2.3)	13.5 (5.3)

Table B2 shows the P50 and P80 data from the ASARCO Mission copper mine. The data in Table B2 gives an average P50/P80 value of 0.46, which gives an N value of 1.084. Additional P50 and P80 data from quarry blasts (Kim, 2006) is shown in Table B3. The data in Table B3 gives an average P50/P80 value of 0.53, which gives an N value of 1.33.

**Table B3. P50 and P80 in quarries (Kim, 2006)**

P50, cm (inches)	P80, cm (inches)
25.4 (10.0)	49.3 (19.4)
21.3 (8.4)	42.9 (16.9)
22.6 (8.9)	43.2 (17.0)
20.8 (8.2)	33.5 (13.2)
8.1 (3.2)	16.3 (6.4)
14.5 (5.7)	26.4 (10.4)

The uniformity index N can also be determined from the formula given by Cunningham (1983, 1987):

$$N = \left( 2.2 - 14 \frac{B}{D} \right) \left( 1 + \frac{S/B}{2} \right)^{0.5} \left( 1 - \frac{W}{B} \right) \left( \frac{|L_B - L_C|}{L_B + L_C} + 0.1 \right)^{0.1} \frac{L}{H} \times (1.1 \text{ or } 1.0) \quad (8)$$

Where,

D is the hole diameter in mm,

B is the burden in meters,

W is the standard deviation of drilling accuracy in meters,

S is the spacing in meters,

$L_B$  is the bottom charge length in meters,

$L_C$  is the column charge length in meters,

L is the total charge length in meters,

H is the Bench height in meters.

(1.1 or 1.0) means the uniformity index is increased by 10% if the staggered pattern is employed.

By using Equation 7 and 8, N is found to be in the range of 1.05 to 1.41 due to (+/-) 3 meters of change in the burden and spacing (and fixing bench height and hole diameter in the blasting pattern). This is consistent with the actual data in Tables B2 and B 3.

Based on the discussion above, we make the assumption for the Asarco Mission mine that  $N = 1.084$ . Using this, and given a desired post-blast fragmentation P80, Equation 7 can be rearranged to give the following formula for the parameter  $X_C$ :

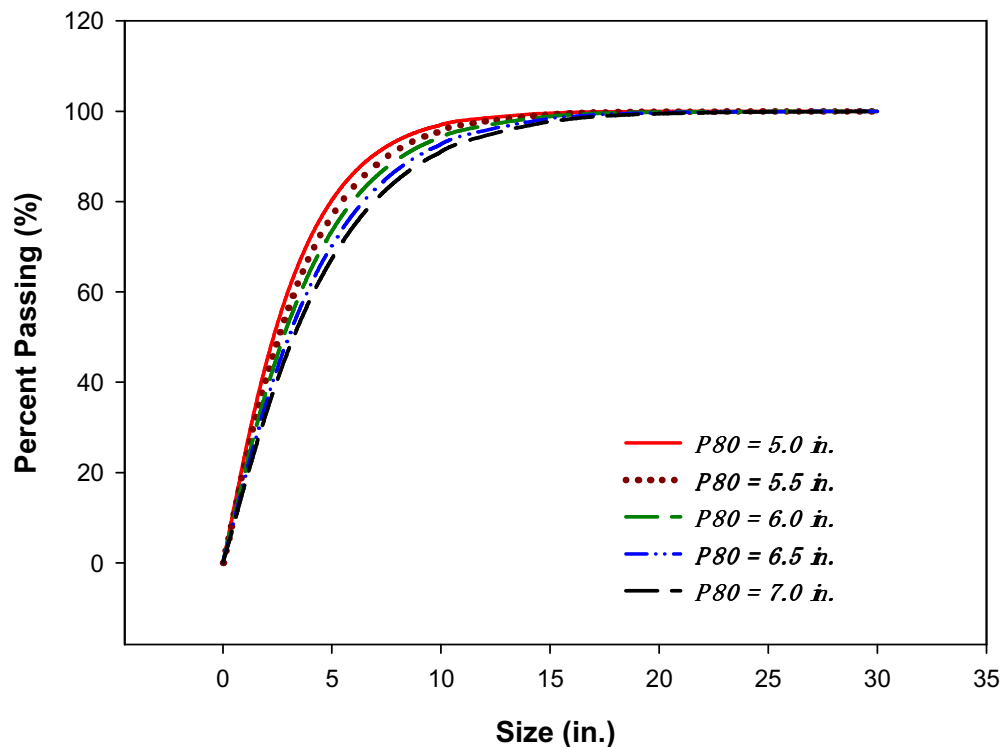
$$X_C = 10^{\log(P80) - 0.1905} \quad (9)$$

Some example results of calculating  $X_C$  for P80 values ranging from 12.7cm (5.0 inches) to 17.8cm (7.0 inches) are shown in Table B4.

**Table B4. Xc calculation by using predicted P80**

Case number	P80, cm (inches)	Xc, cm (inches)
1	12.7 (5.0)	8.2 (3.2)
2	14.0 (5.5)	9.0 (3.6)
3	15.2 (6.0)	9.8 (3.9)
4	16.5 (6.5)	10.6 (4.2)
5	17.8 (7.0)	11.5 (4.5)

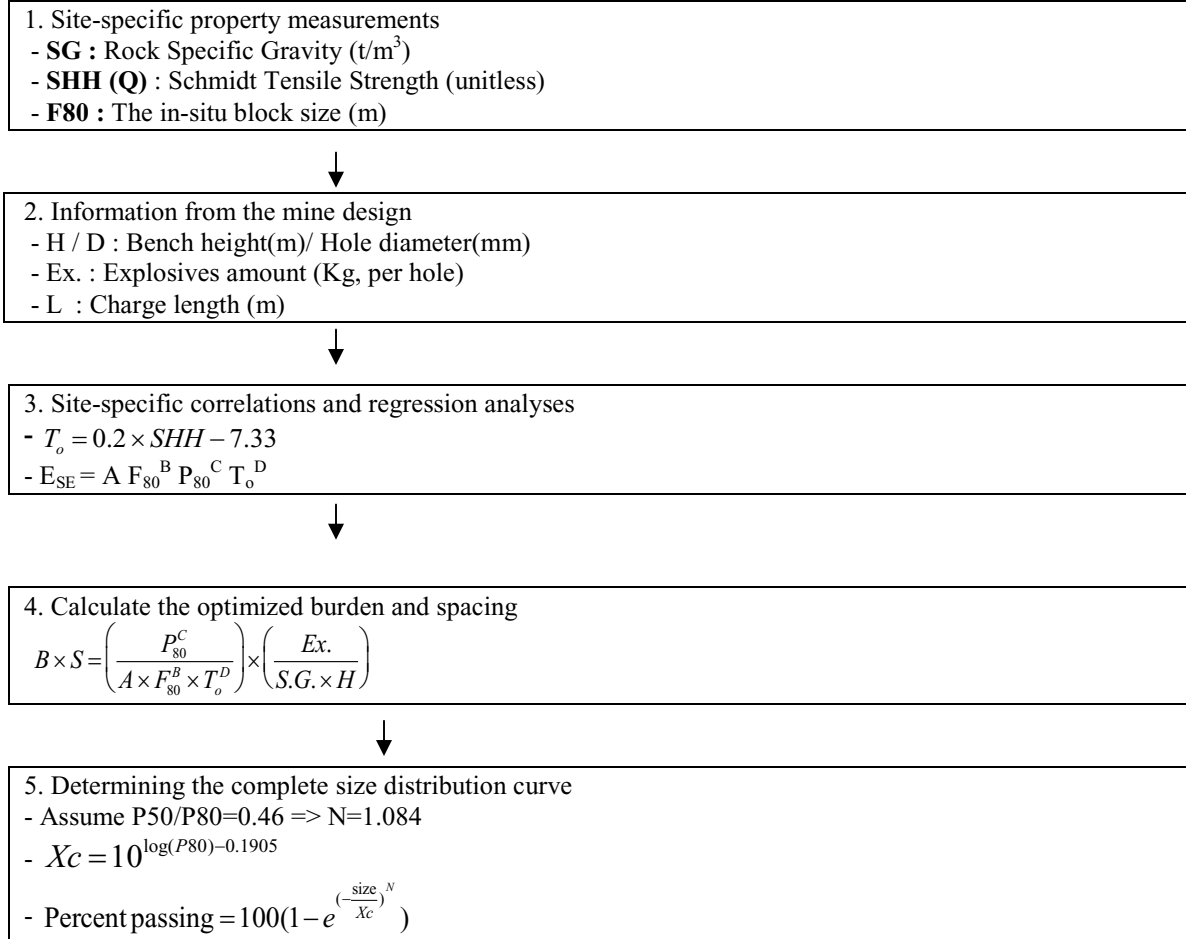
A plot of the resulting size distribution curves using the Rosin-Rammler distribution is shown in Fig. B6.

**Figure B6. Predicted size distribution curves as increasing P80**

### ***Flow Chart***

The results developed in this paper so far are summarized in the flow chart shown below.

Start with a section of rock where the goal is to achieve a certain post-blast fragmentation, P80. Given P80, calculate the following:



#### B4. Applications of the Site-Specific Blast Model

The purpose of the site-specific blasting model is to optimize blasting for total cost or total energy, including downstream comminution and mineral extraction. In general, increased explosive energy will result in finer fragmentation and increased rock damage (microcracking). Thus, even though the drilling and blasting costs may increase, the total mine-through-mill costs will decrease. There is a limit, however, and there is a point at

which further increases in drilling and blasting costs will increase rather than decrease the total cost. The site-specific blasting model developed in this paper can be used to find that optimum point.

An analysis of total cost savings vs. explosive energy has been conducted using the site-specific blast model. Details will be the subject of a future paper, but a few results are presented here. A general flow chart of the approach is given below.

1. At a site where the site-specific model has been calibrated, calculate P80 values for a range of blast energies,  $E_{SE}$ :

Input:

- **SG** : Rock Specific Gravity ( $t/m^3$ )
- **SHH (Q)** : Schmidt Hammer Hardness
- **F80** : The in-situ block size (m)
- **Ese** : Specific Explosive Energy (KJ (Kcal) per 97one)

Output:

- P80



2. Calculate power consumption at each comminution stage as a function of P80. For each P80:  
- Total energy = blast  $E_{SE}$  + comminution energy



3. Compare the energy consumption as a function of changing blast energy



4. Calculate the relative saving cost percentage based on a relative energy cost % at each stage.

The comminution energy at each comminution stage is calculated using Bond's law:

$$W = 10W_i \left[ \frac{1}{\sqrt{Product80}} - \frac{1}{\sqrt{Feed80}} \right]$$

Where:

W is the energy consumption in kWh/ 97one.

$W_i$  is the Bond's Work Index in kWh/97one.

Product 80 is the 80% product passing size in  $\mu\text{m}$ .

Feed 80 is the 80% feed passing size in  $\mu\text{m}$ .

Also, the effect of decreases in the Bond Work Index due to microcracking is included, following the work of Nielsen and Lownds (1997) and Nielsen and Malvik (1999).

An initial set of simulations was conducted for the Asarco Mission mine for a “hard” and “soft” rock. The percent of total energy going into the various rock breaking activities were assumed to be 3%, 16%, and 81% for blasting, crushing, and grinding respectively. These numbers are considered reasonable based on the expense related with energy consumption at Mission. The Bond Work Index values were assumed to be 20 kWh/98one for the hard rock such as Argillite and Epidote Skarn that is found at Mission mine, and 10 kWh/98one for the soft rock such as Marble and Siltstone at Mission. Also it was assumed that the fine grinding stage is the primary bottleneck for production (Elias, 2009; Nielsen and Lownds, 1997 and Nielsen and Malvik, 1999). Based on these assumptions, plots of total productivity improvement (%) and total cost savings (%) vs. blast energy are shown in Fig. B7.

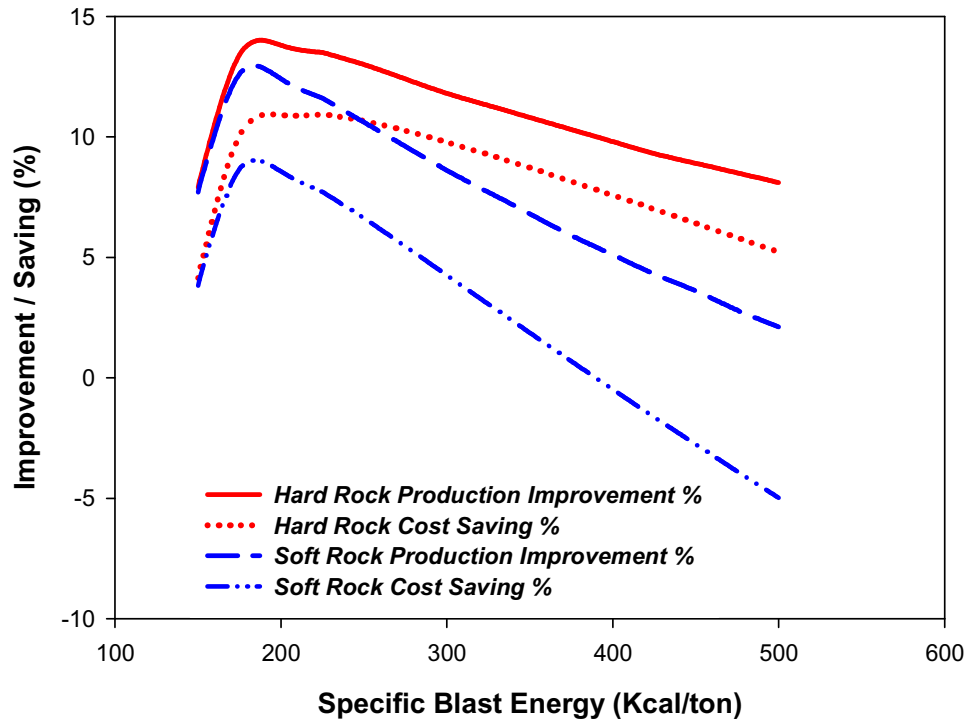


**Figure B7. Total production improvement (%) and total cost saving (%) vs. blast energy**

The results clearly show optimal (peak) values of blast energy for both the hard and soft rock. The hard rocks show a more gradual decrease past the optimal value compared with the soft rock. Also, the results predict that a negative cost savings will occur in the soft rock when the blast energy is more than 1675 KJ/t (400 Kcal/t). Fig. B7 indicates optimum blast energies of 942 (225) and 733 (175) KJ/t (Kcal/t) for hard rock and soft rock, respectively.

Based on the results in Fig. B7, the cost savings associated with some hypothetical increases in blast energy can be calculated, as shown in Table B5.

**Table B5. Predicted P80, total cost saving, and production increase as increasing the blast energy**

Rock Type	Bond's Work Index (Kwh/t)	Blast Energy Increase KJ/t (Kcal/t)	Predicted P80, cm (inches)	Total Cost Saving, %	Production Increase, %
Hard Rock	20	603 (144) → 1047 (250)	16.5 (6.5)	10.66%	13.00%
Hard Rock	20	603 (144) → 1675 (400)	12.4 (4.9)	7.57%	9.88%
Soft Rock	10	603 (144) → 1047 (250)	14.0 (5.5)	6.62%	10.60%
Soft Rock	10	603 (144) → 1675 (400)	10.7 (4.2)	-0.49%	5.10%

Here we consider increasing the blast energy from 603 KJ/t (144 Kcal/t) to either 1047 (250) or 1675 (400) KJ/t (Kcal/t). The highest cost savings is associated with increasing the blast energy to 1047 KJ/t (250 Kcal/t) in the hard rock, and a negative cost savings occurs when for an increase to 1675 KJ/t (400 Kcal/t) in the soft rock.

Even though these results are preliminary, they show the importance of having an accurate blast fragmentation prediction model. Also, there are other factors to be considered besides cost savings and increases in productivity. Higher blasting energies are often associated with higher blast vibrations, which can damage slopes and structures.

## B5. Conclusions

A site-specific blasting model has been developed for the Asarco Mission mine. The main inputs to the model are the in-situ block size (F80), the post-blast fragmentation (P80) and the intact tensile strength (To). The output from the model is the specific blast energy ( $E_{SE}$ ). Modern techniques are being used to obtain the input parameters for the site-specific blast fragmentation model. In particular, image processing software is used to obtain both the in-situ block size and the post-blast fragmentation, and the Schmidt

hammer (calibrated separately for each rock type) is used to obtain the tensile strength at numerous locations throughout the rock mass.

An initial model was developed using five test shots in one area of the mine that contains Argillite and is relatively homogeneous. This also included calibrating Schmidt hammer readings against actual Brazilian tensile measurements. The model for Argillite will be updated as more tests are conducted, and the model will be extended to the other four primary rock types at the Asarco Mission mine.

An important application of the model is to optimize the blasting for mine-through-mill cost savings and productivity. A preliminary study was conducted to look at total cost savings vs. blast energy for a hard and soft rock, and indicated optimum blast energies of 942 (225) and 733 (175) KJ/t (Kcal/t) for hard rock and soft rock, respectively.

#### ***Acknowledgement***

The authors wish to express their gratitude to the fragmentation team in ASARCO Mission for supporting us to be able to perform this study. Especially, the authors are grateful to the mine manager (Hal Galbraith) and mine technician (Rob Davenport) for their support and help.

## References

- [1] Chung, S. H. & Katsabanis, P.D. (2000) Fragmentation prediction using improved engineering formulae. *Fragblast, vol. 4, No. 3-4, pp 198-207.*
- [2] Cunningham, C. (1983) The Kuz-Ram Model for the Prediction of Fragmentation from Blasting, *Proceedings of the international Symposium on Rock Fragmentation and Blasting, Lulea, Sweden.*
- [3] Cunningham, C. (1987) Fragmentation Estimations and the Kuz-Ram Model – Four years on, *Proceedings of the second international Symposium on Rock Fragmentation and Blasting, Keystone, Colorado.*
- [4] Demirdag, S., Yavuz, H., Altindag, R., 2008, The effect of sample size on Schmidt rebound hardness value of rocks, *Int. J. Rock Mech. Min. Sci., Vol 46, pp 725-730*
- [5] Donovan, J. G., 2006, Fracture toughness based models for the prediction of power consumption, product size, and capacity of jaw crushers, *Doctor of Philosophy dissertation, Mining and Mineral Engineering, Virginia Tech, Blacksburg.*
- [6] Elias S., Olga P., Evangelos P. 2009, Surface area production during grinding, *Minerals engineering, Vol. 22, pp 587-592*
- [7] JKMR (1996) Open Pit Blast Design: analysis and optimization *The University of Queensland.*
- [8] Kim, K. M., 2006, Blasting design using fracture toughness and image analysis of the bench face and muckpile, *Master of Science thesis, Mining and Mineral Engineering, Virginia Tech, Blacksburg*

- [9] Kuznetsov, V.M., 1973, The mean Diameter of the Fragments Formed by Blasting Rock, *Soviet Min. Sci. Vol.9*, pp 144-148.
- [10] Lilly, P.A. (1986) An empirical method of assessing rock mass blastability *Proceeding Large Open Pit Mining Conference*, pp. 89~92.
- [11] Nielsen, K., Lownds, 1997, Enhancement of Taconite Crushing and Grinding Through Primary Blasting, *Int. J. Rock Mech. Min. Sci., Vol 34:3-4*, paper No. 226
- [12] Nielsen, K., Malvik, T., 1999, Grindability enhancement by blast-induced microcracks, *Powder Technology 105*, pp 52-56.
- [13] Rustan, Agne, 1998, Rock Blasting Terms and Symbols *A.A. Balkema, Rotterdam, Brookfield*
- [14] SilverSchmidt Operating Instructions, 2007, *Proceq SA*
- [15] Spathis, A.T., 2004, A Correction relating to the Analysis of the Original Kuz-Ram Model, *Fragblast, Vol.8, No 4*, pp 201-205
- [16] Split Engineering. 2010. [www.spliteng.com](http://www.spliteng.com)
- [17] Whittaker, B. N., Singh, R. N., Sun, G., 1992, Rock Fracture Mechanics – Principal, design, and application, *Elsevier Science Publishers B. V.*
- [18] Zhang, Z.X., 2002, An empirical relation between mode I fracture toughness and the tensile strength of rock, *Int. J. Rock Mech. Min. Sci., Vol 39*, pp 401-406

## **APPENDIX C: APPLYING RECENT IMAGING TECHNOLOGIES TO ROCK MASS CLASSIFICATION**

Kwangmin Kim and John Kemeny  
*The University of Arizona, Tucson, AZ, U.S.A.*

WILL BE SUBMITTED TO INTERNATIONAL JOURNAL OF ROCK  
MECHANICS AND MINING SCIENCE (2012).

## APPLYING RECENT IMAGING TECHNOLOGIES TO ROCK MASS CLASSIFICATION

Kwangmin Kim and John Kemeny  
*The University of Arizona, Tucson, AZ, U.S.A.*

### **Abstract**

Traditional techniques for rock mass characterization include cell mapping and scanline surveying. In an effort to address issues of safety, access, human bias and timeliness, traditional cell mapping was compared with rock mass characterization utilizing two new technologies, digital image processing and ground-based LIDAR. A case study was conducted at an open-pit copper mine in Arizona, where eight 10 m x 10 m cells were characterized using both using the traditional and the new technologies. Using both methods, the GSI rock mass classification number was estimated in each cell, as well as a stereonet pole plot of joint orientations. The modified GSI technique of Cai et al. [1] was used, which uses four pieces of information: average block size ( $F_{50}$ ), joint alteration ( $J_a$ ), joint smoothness ( $J_s$ ) and joint waviness ( $J_w$ ). The average block size was estimated by processing digital images of the bench faces using digital image processing software. The joint waviness was estimated by processing LIDAR point clouds of the bench faces using point cloud processing software. In this study joint alteration and joint smoothness were not estimated using the new technologies even though this will be the subject of future studies. The results show a fair correlation between the traditional and the new

techniques for estimating GSI and joint orientations. This is to be expected, since manual cell mapping is a technique for quickly obtaining data in the field, and only very limited measurements are made, and with limited access. The new technologies generate a large database of information on each cell, which will result in increased accuracy as well as the ability to process the data in many different ways. The amount of time spent in the field is about the same between the traditional cell mapping and the collection of data using digital images and ground-based LIDAR (20-30 minutes per cell). Processing the data from the new technologies requires several additional hours of analysis per cell. Overall it is shown that given the importance of rock mass characterization in slope stability design, it is worthwhile to consider the new technologies of digital image processing and ground-based LIDAR.

## C1. Introduction

Estimating rock mass strength in hard rock mines is one of the main considerations in reducing slope stability problems and optimizing stripping ratios. However, it is always challenging because of the heterogeneity and complexity of rock masses. The size and difficulty in sampling rock masses in hard rock mines is another major problem that must be dealt with. Because of these issues, estimating rock mass strength in hard rock mines will always be difficult and challenging, and new technologies for assisting with the estimation of rock mass strength are expected play a bigger and bigger role in the future.

There are four principal ways to measure rock mass strength: (1) numerical modeling, (2) large scale testing, (3) back analysis of measured deformation and failure, and (4) empirical formulations based on rock mass classification [2,3]. This paper will focus on empirical formulations based on rock mass classification, and in particular focus on new field technologies to assist with the estimation rock mass classification. There are a number of rock mass classification systems, including RMR [4], RMS [5], Rmi [6], GSI [7], Q [8], MRMR [9], and others. In this paper we focus on GSI (Geological Strength Index), since the GSI is appropriate for large open pit hard rock mines and recent formulations are available for estimating rock mass strength from GSI, as well as taking into account human bias and other issues [1]. The focus of this paper is on utilizing two new technologies, 2D image processing of digital images and ground-based LIDAR scanning, to increase the accuracy and efficiency of GSI estimation.

Rock mass classification is a subset of rock mass characterization, and in general rock mass classification is determined by first collecting rock mass characterization information, which includes discontinuity orientation, spacing, length, roughness, aperture, etc. Rock mass characterization information can be obtained by geologic mapping (scannline and cell mapping) in hard rock mines. However, traditional rock mass characterization of large open-pit mines requires significant data collection, which is time-consuming and involves safety hazards and human bias. Therefore, this paper focuses on replacing or supplementing standard cell mapping with new technologies. In particular, this paper focuses on using two new imaging technologies to estimate GSI: 1)

2D image processing of digital images of bench faces to obtain block size information, and (2) 3D ground-based LIDAR scanning to extract joint topographies and determine various large-scale joint roughness parameters.

These new technologies are applied to an adjusted GSI system based on the work of Cai et al. [1]. The original GSI system proposed by Hoek [7] is qualitative rather than quantitative and thus more difficult to adopt with new technologies for data collection. The adjusted version of GSI requires two main pieces of information concerning rock mass classification: bench block size (or block volume) and the joint condition factor ( $J_c$ ). The adjusted GSI chart is shown in Figure C1 [1].

# GSI

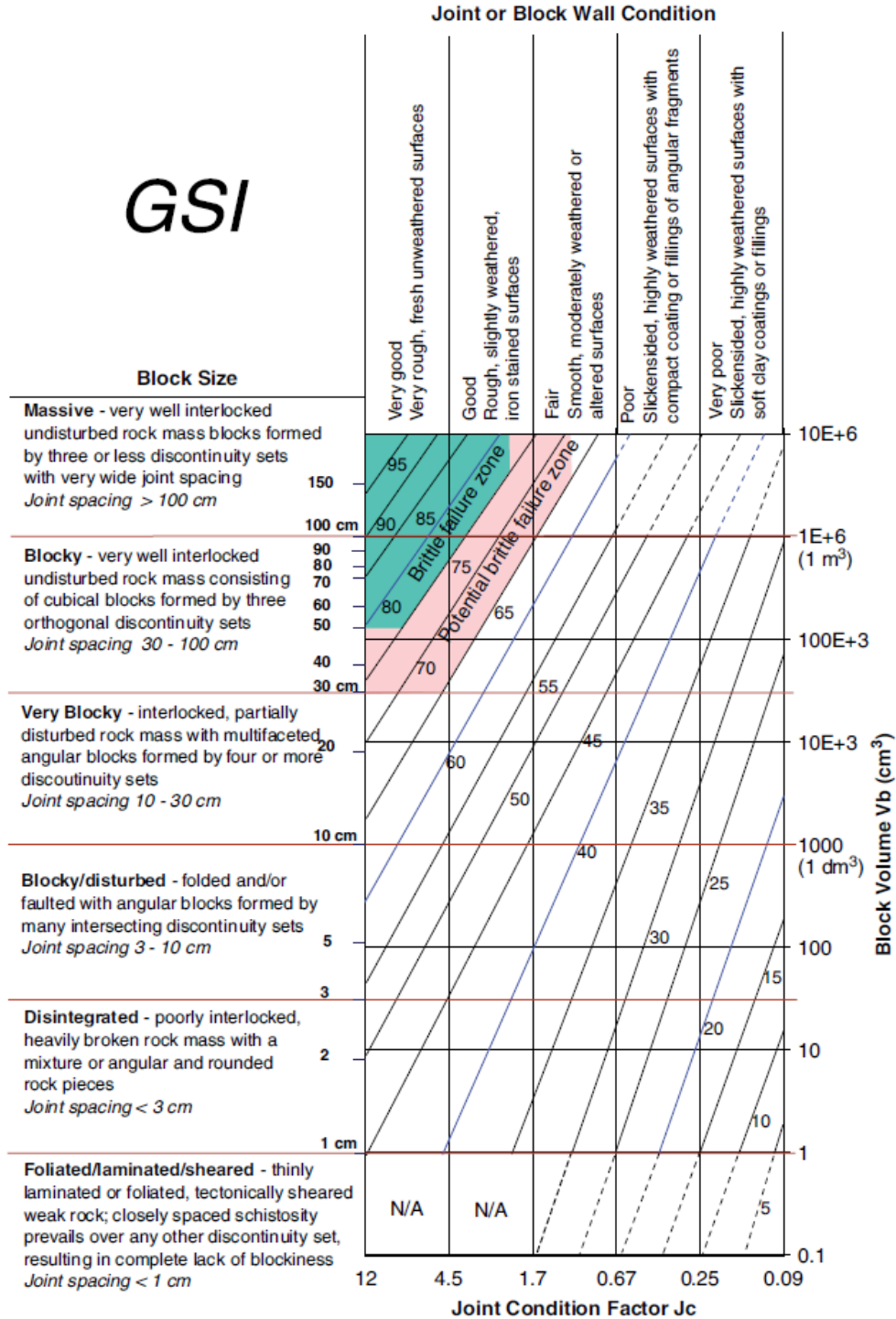


Figure C1. Quantification of GSI chart [1]

Image processing software, Split-desktop, is used for measuring the bench face block size quickly and safely from digital images taken of the bench faces [10,11]. The joint condition factor consists of three parameters: joint alteration ( $J_a$ ), joint smoothness ( $J_s$ ) and joint waviness ( $J_w$ ). Ground-based LIDAR scanning and the processing of point clouds using and the Split-FX software, are used to determine joint waviness, which is hard to measure and time-consuming in manual cell mapping. To validate this approach, results of GSI estimation from the new technologies are compared with results obtained from a professional geological engineer. In addition to GSI, joint orientation measurements and stereonet plotting are important rock mass characterization information obtained from cell mapping. In this study, joint orientations and stereonet plots are obtained from the LIDAR point clouds using the Split-FX software [12], and these are compared with the cell mapping data of a professional geological engineer to validate the approach.

## C2. Bench Block Size using Digital Image Processing

Digital image processing involves the processing of high-resolution digital images for information extraction or pattern recognition [13]. In recent studies [10,11], digital image processing has been used to obtain the bench face block size (in-situ block size) in blasting optimization studies. These studies have found that this approach is efficient and cost-effective compared with manual methods, which are time-consuming and subject to human bias. In this section, digital image processing is used to determine the block volume for use in the adjusted GSI system proposed by Cai et al. [1]. The use of digital

image processing provides information across the entire bench where access with manual methods would be difficult. It is also an automated approach and thus reduces human bias, and increases safety by processing digital images that are taken from a safe distance.

#### *Digital Image Processing Software*

There are a number of digital image processing programs available that could be used to process digital images from open-pit mining benches. Some of these programs are designed specifically for processing images of rock fragments, including IPACS [14], TUCIPS [15], FRAGSCAN [16], WipFrag [17] and SPLIT-Desktop [12]. There are also more generic image processing programs that could be used, such as ImageJ [18] and Matlab [19]. Because the authors have experience with the Split program, it is used in this study.

Image processing programs have many potential advantages over manual methods for estimating rock block size, as has been discussed. These advantages include automated processing, minimal human bias, access advantages, and increased safety. However, there are also some important limitations and possible inaccuracies associated with image processing programs. First of all, image processing programs can only analyze what can be seen in digital images of rock masses. The block size that is estimated, therefore, is based on the apparent block size distribution on the surface of the rock outcrop. Secondly, the delineation of individual blocks by image processing programs is imperfect, resulting in large blocks that are often over-divided and small blocks that are mistakenly

combined. Thirdly, very small blocks or “fines” are often underestimated in image processing programs because they are not properly represented on the surface.

In general, a digital image of a rock outcrop is analyzed as follows to estimate the block size for use in the adjusted GSI system:

- A delineation algorithm is used to break up the image into discrete blocks
- An optional step to edit the delineation to correct errors
- The volume and size (average spacing) for each block is estimated based on the area and aspect ratio of the block
- The additional volume of fines that cannot be seen is estimated
- The volume distribution of the blocks is calculated (%volume passing vs. block size)
- The average block size (50% passing size) or some other statistical measure (such as the 80% passing size) is used as the block size in the adjusted GSI system

The quality and accuracy of results from digital image processing depends on the quality of the digital images that are obtained and the consistency in the way in which images are taken. Therefore, the following guidelines should be kept in mind: (1) keep a consistent distance (about 40 ft. was used in this study) between the face and the camera, (2) the lighting should be as optimal as possible, and (3) any fines and editing settings should be consistent (no editing and 0% fines used in this study).

### C2.1 Average bench block size and 50% passing size (F50)

In previous studies [10,11], it was found that the image processing software, Split-Desktop, did a good job of delineating rock blocks on the bench face. The program gives a complete size distribution of the rock blocks, and it was found that the 50% passing size (F50) from the size distribution is a good measure of the average block size (joint spacing) that would be measured using manual mapping. It is noted that F50 is used instead of P50 in this study to differentiate 50% passing size from the bench face (F50) and 50% passing size from the muckpile (P50). Also, in [11], F80 was assumed as a representative bench block size in the blast fragmentation model, but in this study, we were not looking for the representative size, but for the average block size that can be used in the adjusted GSI scheme. Therefore, F50 was used as the applicable block size in the adjusted GSI chart as given in Cai et al. [1].

Figure C2a shows a highway rock slope image. Three horizontal and three vertical lines have been drawn through the rock blocks and are used for estimating the joint spacing. Figure C2b shows the delineation of the rock blocks using the Split-Desktop program. Note that the delineation of the rock blocks is good except for areas where shadows occur. The image processing program has blackened these areas. These areas are used in the calculation of fines, but since 0% fines was assumed, these areas are ignored in the calculation of the size distribution.

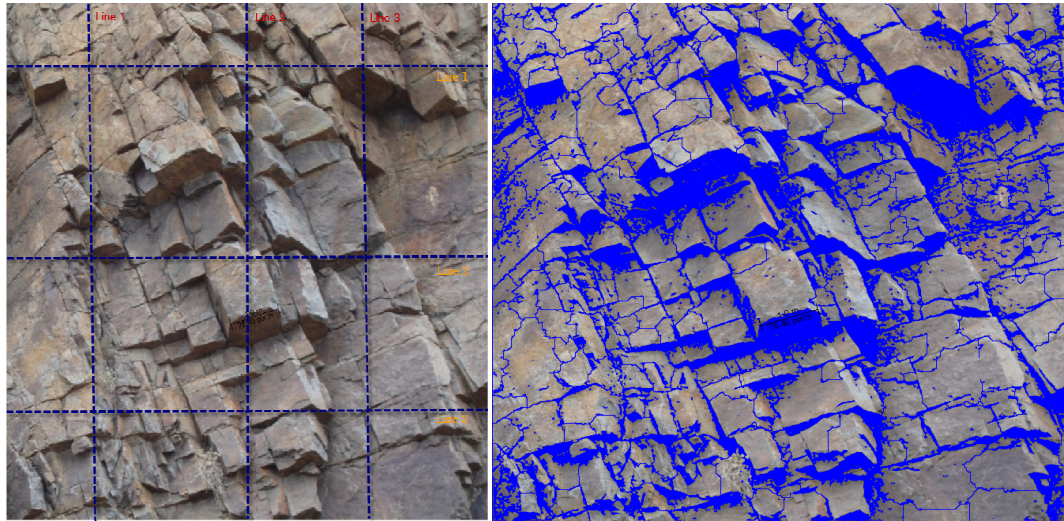


**Figure C2. (a) Highway rock slope image for counting the joints (left) and (b) the delineated image (right)**

The average joint spacing is measured by counting the number of joints vertically and horizontally and dividing by the length of the lines, as shown in Table C1. To compare the obtained bench block size with the F50 from the image processing software, the shape of the blocks are assumed to be circular blocks, and the average circular block size is measured as shown in Table C1.

**Table C1. Measuring the bench block size by counting the joints**

Line Number	Joint counts #	Average joint counts #	The whole distance (cm)	Block size (cm)	Circular block size (cm)
Vertical 1	23	<b>20.33</b>	<b>940</b>	<b>46.23</b>	<b>53.30</b>
Vertical 2	24				
Vertical 3	14				
Horizontal 1	23	<b>20.00</b>	<b>965</b>	<b>48.25</b>	
Horizontal 2	17				
Horizontal 3	20				

The highway rock slope image delineated by the image processing program is shown in Figure C2b, giving an F50 of 62.98 cm. It shows a relatively big variance, 9.68cm, with

the bench block size (53.30cm) determined from the vertical and horizontal lines as shown in Table C1. In this case, we believe that the variance is mainly from errors due to the many shaded areas in the image of the highway rock slope, as well as some delineation errors.

Another trial with the bench face image from a hard rock surface mine in Arizona is shown in Figure C3.

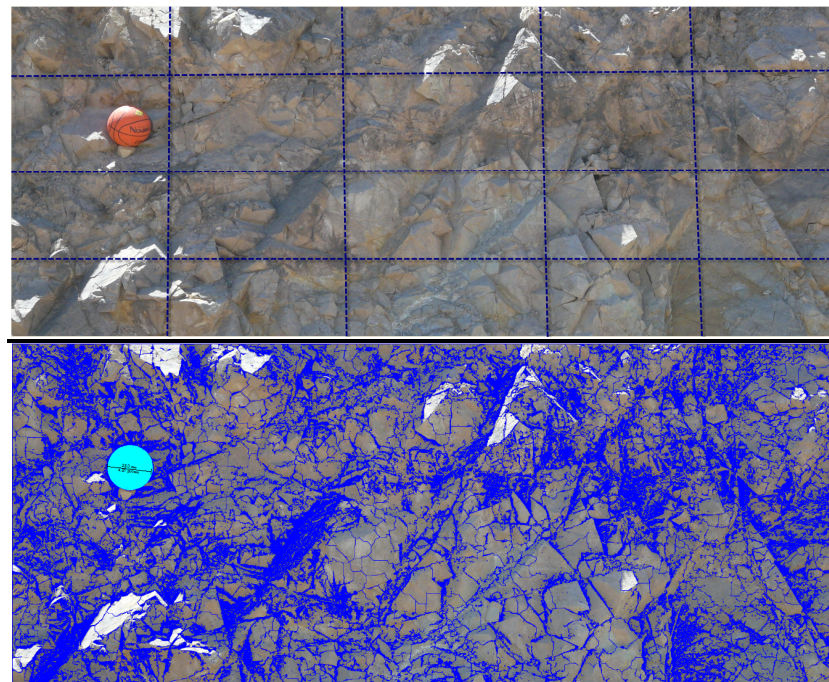


**Figure C3. Images for counting the joints and the delineated image from a mine**

As before, a number of lines have been drawn through the rock blocks for the calculation of joint spacing, and a circular block shape is assumed when comparing with the image processing results. The calculated average block size is shown in Table C2.

**Table C2. Calculating the average block size**

Line	number	Joint Num.	Average	Distance (meters)	Block Size (cm)	Circular size (cm)
Vertical	1	33	<b>28.75</b>	<b>1.98</b>	<b>6.87</b>	<b>8.29</b>
Vertical	2	30				
Vertical	3	30				
Vertical	4	22				
Horizontal	1	69	<b>60.00</b>	<b>4.71</b>	<b>7.86</b>	
Horizontal	2	56				
Horizontal	3	55				

In this trial, the F50 from the image processing size distribution curve is 8.52cm which is similar to the measured circular size of block, 8.29cm. The variance is just 0.23cm. It is noted that the 50% passing size in the cumulative size distribution is not same as the average size, even though empirically it has been found that they are usually very close.

We conclude that most of the variance in the first trial is from the shadows and delineation errors. Thus, if we keep the constant distance between the camera and the face and there is good light, as shown in the second trial, then image analysis method might provide a consistent block size of the bench, a method that is quick and safe and reduces human bias. In addition, the applicability of image processing technology for the bench block size was shown in the previous studies [10,11]. Thus, we accept F50 and use it as the average block size in this study.

### C3. Measuring Joint Waviness and Joint Orientation by Using Ground-Based LIDAR

LIDAR (Light Detection and Ranging) is an instrument that scans a scene and generates a detailed three-dimensional point cloud [20]. The point cloud is comprised of x,y,z coordinates and intensity. A color point cloud can be produced by draping a high resolution digital image onto the point cloud. Ground-based LIDAR refers to a compact instrument that is mounted on a tripod. Ground-based LIDAR is particularly useful for steeply dipping topography such as mining and highway slopes, and for problems where a high-density and high-resolution point cloud is needed. A typical ground-based LIDAR scan of a highway slope, for example, can produce a point cloud with a resolution of 5 mm and a point spacing of 2 cm [20]. Ground-based LIDAR is being utilized in a number of areas in rock engineering, including rock mass characterization, slope and underground stability design, and rockfall monitoring [21]. This includes applications in highways, surface mines, underground mines, and bridge and dam foundations. Point cloud processing software refers to software specifically designed to edit and process point clouds. In this study the Split-FX point cloud processing software was used [12]. This software is specifically designed for geotechnical analysis, including rock discontinuity delineation and stereonet plotting, cross sections, and change detection.

There are many rock mass classification schemes, as discussed previously. Here we use the Geologic Strength Index (GSI), and in particular the modifications by Cai et al. [1,6]. The GSI has the advantage that it can be related to rock mass strength, and the

modifications by Cai et al. have the advantage that it is more quantitative than the original GSI and easily adopted to the new technologies of image processing and ground-based LIDAR. There are four main factors for the rock mass classification in the adjusted GSI: bench block size (block volume or size), joint waviness ( $J_w$ ), joint smoothness ( $J_s$ ), and joint alteration ( $J_a$ ).

Ground-based LIDAR scans have been taken of a number of bench faces. The point clouds from these scans were then processed to determine joint orientations, and to determine the joint waviness parameter ( $J_w$ ) in the adjusted GSI system. The joint orientation information was compared with manually measured data, which was obtained by an experienced geological engineer.

### C3.1 Joint Surface Condition (Joint Condition Factor, $J_c$ )

The friction angle of a clean rock surface consists of the base friction angle  $\phi$  plus the additional dilation angle due to irregularities or roughness,  $i$ . In an altered joint surface, a high degree of alteration can reduce the friction angle and override the effects of joint roughness and base friction angle. The roughness of a fracture can be quantified either by direct measurement or by standard profiles, and in general joint roughness is scale dependent. To take into account the scale dependence, it is common to consider large-scale and small-scale components to joint roughness [22]. For example, joint roughness ( $J_r$ ) in the Q-system is made up of joint waviness ( $J_w$ , *large-scale feature*) and joint smoothness ( $J_s$ , *small-scale feature*) [1,6].

In the modified GSI proposed by Cai et al. [1], both large scale and small scale roughness and joint alteration are included in the Joint Surface Condition factor,  $J_c$ , which is estimated by the following equation:

$$J_c = \frac{J_w J_s}{J_a} \quad (\text{Equation 1})$$

Where:

- $J_c$  is a joint condition factor.
- $J_w$  is large-scale waviness (from 1 to 10 meters).
- $J_s$  is small-scale smoothness (from 1 to 20 centimeters).
- $J_a$  is the joint alteration factor.

Both the small scale smoothness  $J_s$  and the joint alteration  $J_a$  can be measured quickly in the field by examining joint surfaces at the small scale. To some degree these factors can also be estimated from digital images and ground-based LIDAR scans, and is the subject of future studies. The large scale waviness, on the other hand, is difficult to measure manually in the field due to its large scale nature. It is for this reason that research has been conducted on determining large scale waviness from ground-based LIDAR point clouds.

### C3.2 Joint Waviness ( $J_w$ )

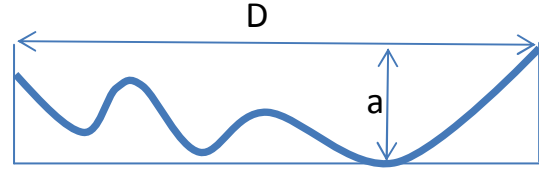
Joint waviness ( $J_w$ ) is estimated by making joint profiles from the LIDAR point clouds and comparing them with the  $J_w$  chart shown in Table C3. The general point cloud processing procedure consists of:

- Start with a point cloud and make a triangulated mesh. The size of the triangles should be larger than the resolution of the point cloud but small enough to see roughness in the fractures at the scale that is desired
- Isolate a specific fracture in the point cloud
- Rotate the fracture so it is perpendicular to the viewing angle
- Draw one or more cross sections through the fracture in different directions (it is actually making cross sections through the triangulated mesh)
- Plot the cross sections and calculate the undulation ( $a/D$  ratio, see Table C3)
- Determine  $J_w$  from Table C3
- Repeat for different fractures in the point cloud

Additional details on this procedure are described below. It is noted that “D” is the length between maximum amplitudes in the profile, and “a” is the amplitude of the asperities in the profile.

**Table C3. Joint Waviness Description [1,6]**

Waviness terms	Undulation	Rating for Waviness, $J_w$	
Interlocking		3	
Stepped		2.5	
Large Undulation	>3%	2	
Small to moderate undulation	0.3~3%	1.5	
Planar	<0.3%	1	



Undulation= $a/D$

As an example, ground-based LIDAR scanning of a bench face was conducted at a copper mine in Arizona as shown in Figure C4. Scanning was conducted using an Optec ILRIS 3D scanner with a distance accuracy of about 5 mm. An area of around  $10\text{ m} \times 10\text{ m}$  (Height  $\times$  Width) was scanned, and a point cloud was generated as shown in Figure C4a. The point cloud in Figure C4a consists of around 1.2 million points and has a point spacing of about 2 cm. The point cloud data was processed by Split-FX program, and a triangulated mesh was created, as shown in Figure C4b.

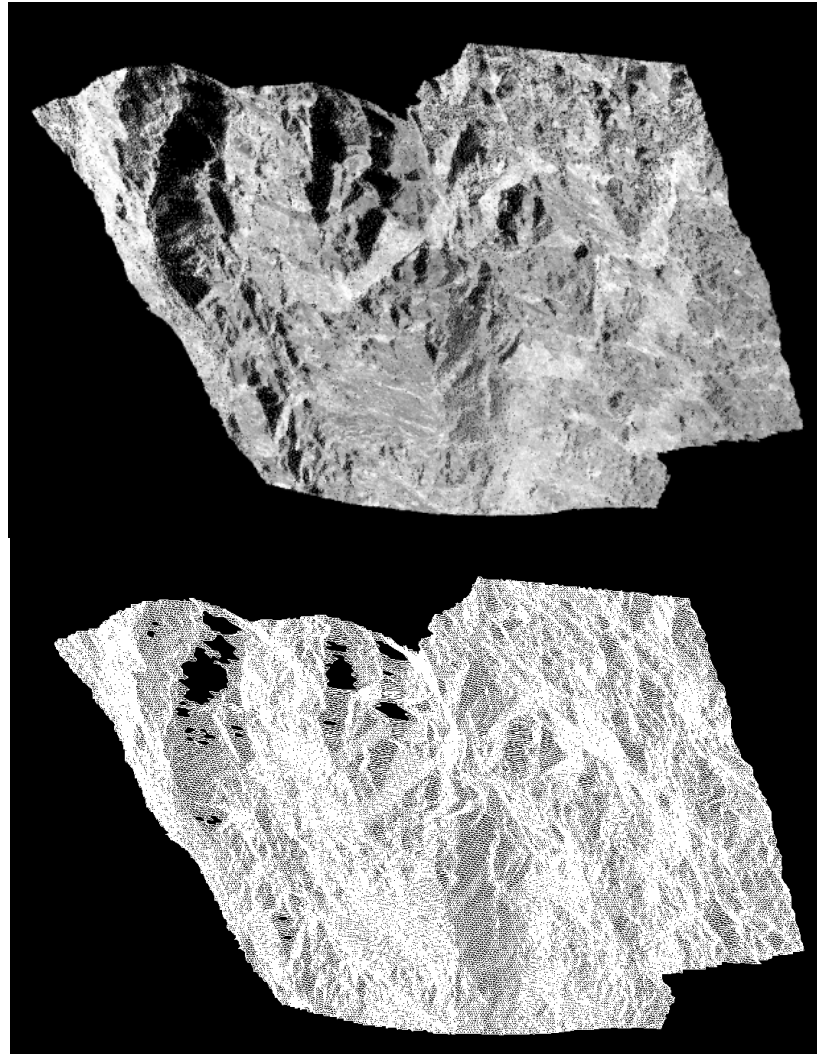


**Figure C4. (a) 3D laser image (upper) and (b) triangular mesh (lower)**

From the triangulated mesh, fracture surfaces were delineated automatically and a stereonet plot was generated. Figure C5a shows the delineated fractures, and Figure C5b shows a lower hemisphere stereonet plot of the fracture poles. Each point in the stereonet represents one fracture, and the size of the plot icon is weighted by fracture area, so major

fractures appear as larger circles. Several distinct joint sets are apparent in the stereonet plot, and these have been outlined in Figure C5b.

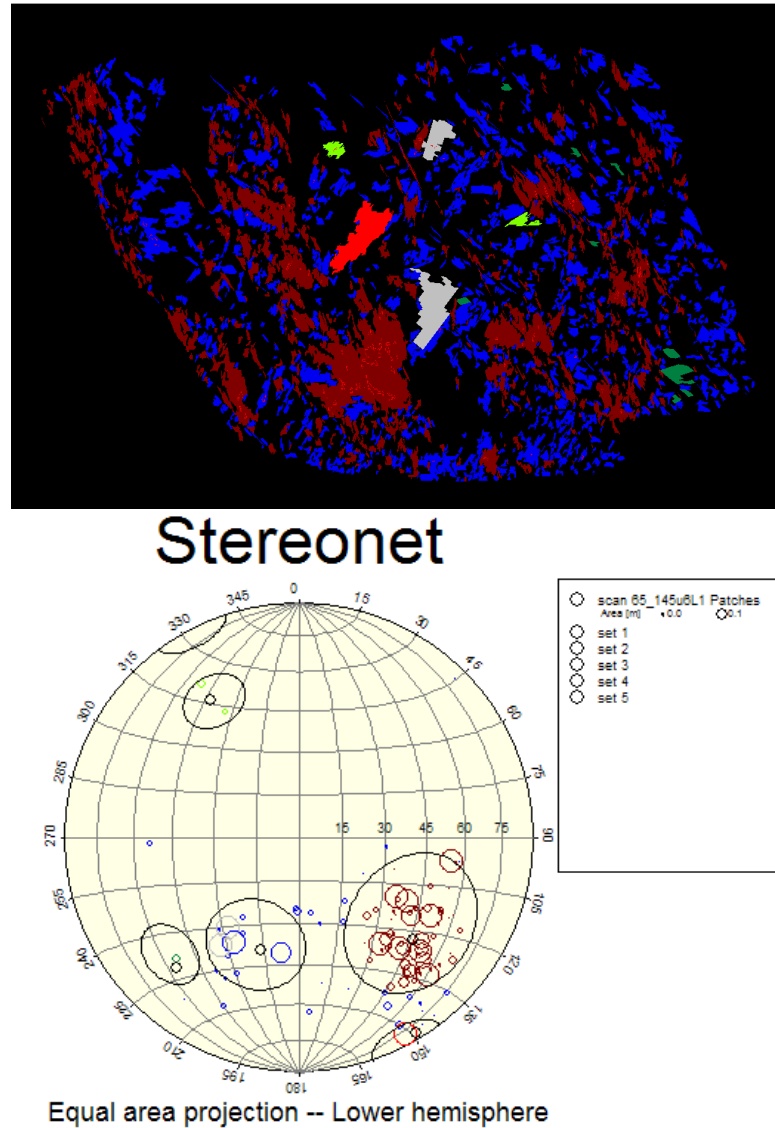


**Figure C5. (a)** The found patches in the point cloud (upper) and **(b)** a generated stereonet (lower)

Figure C5b shows that five joint sets are clearly apparent. In Figure C6a, joint set 1 (JS1) has been selected in the stereonet, and this results in the individual fractures in joint set 1 being highlighted in green in the point cloud, as shown in Figure C6b. Two relatively large fractures are then selected in JS1, as shown in Figure C7. The cross section of through these two fractures is shown in Figure C8.

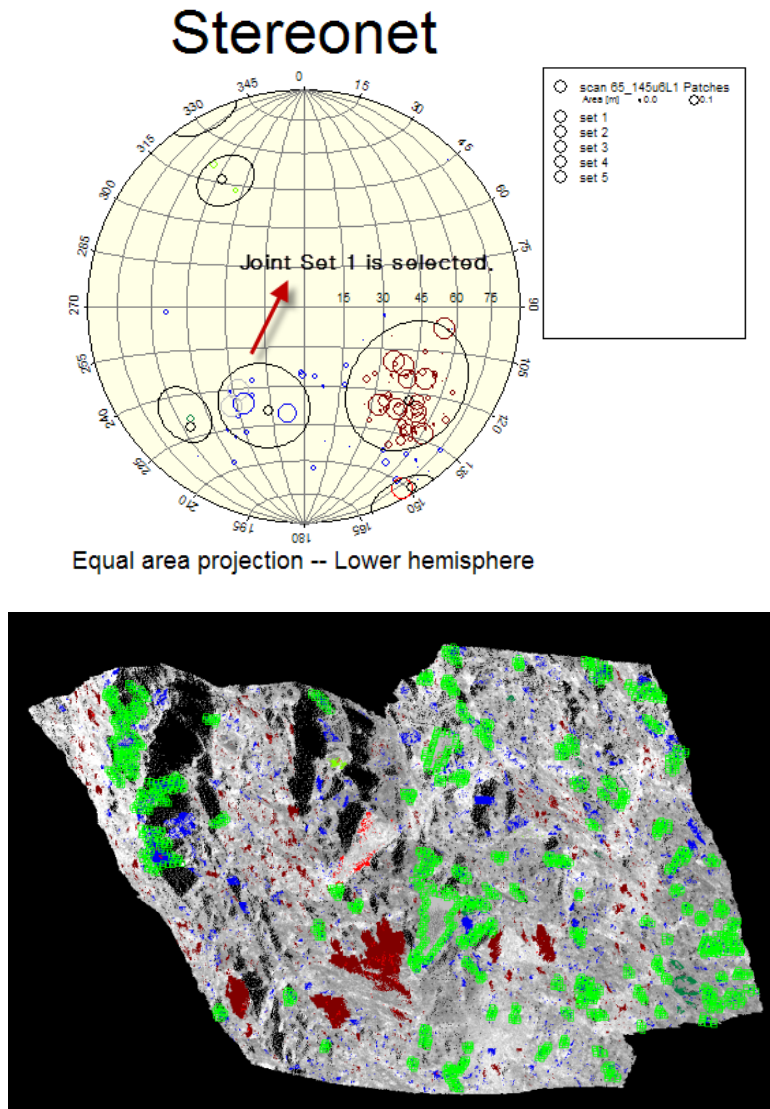


**Figure C6. (a)** The selected Joint Set 1 in the stereonet (upper) and **(b)** the point cloud image (lower).

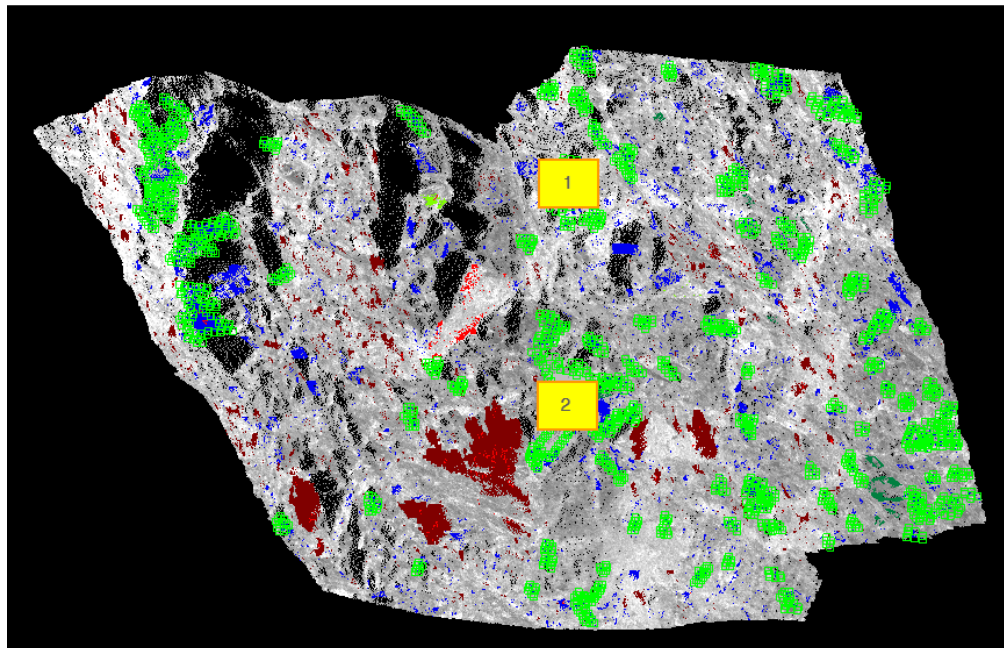


**Figure C7. Two selected patches in Joint Set 1**

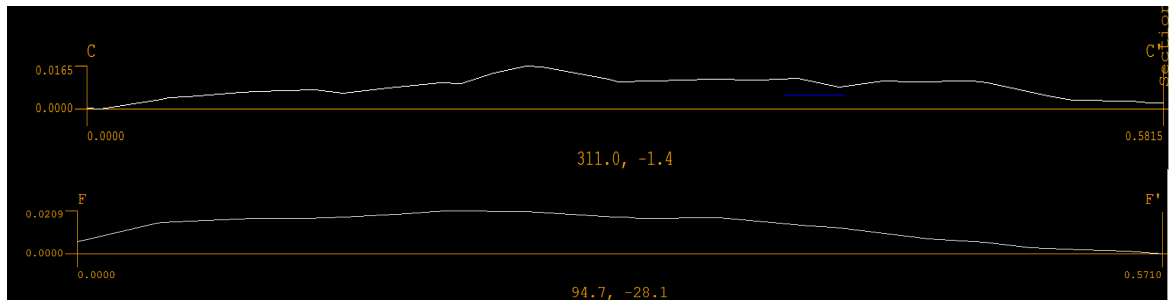


**Figure C8. Two cross-sections of the selected patches in Joint Set 1**

Figure C8 shows that each of these fractures has a length of about 0.6 meters. Based on the cross sections shown in Figure C8, the undulation (a/D ratio) has been calculated, giving an undulation of  $0.0165/0.452 \times 100 = 3.6\%$  for the top cross section, and an undulation of  $0.0209/0.732 \times 100 = 2.86\%$  for the bottom fracture. Using the Jw chart in

Table C3, this gives  $J_w$  values of 2.0 and 1.5 for the top and bottom fracture, respectively. Using this procedure, the joint waviness  $J_w$  values for Sets 1 through 5 are shown in Table C4, giving an average value for all 5 sets of about 2.0.

**Table C4. Joint Waviness Measurement by using LIDAR scan**

Set Number	Joint Waviness ( $J_w$ )
Set 1	2.0 (3.6, 2.86%)
Set 2	2.0 (4.43%)
Set 3	1.5 (2.17, 1.67%)
Set 4	2.0 (3.10, 3.5%)
Set 5	2.5 (12, 13.6%)
Average	2.0 (Ave. 5.21% / Min. 1.5~Max2.5)

As shown in Table C4, the important rock mass classification parameter  $J_w$  can be determined in a relatively straightforward fashion using ground-based LIDAR data. The time required to conduct the analysis is broken down as follows. The time required for fracture delineation and stereonet plotting is between 1~1.5 hours. The time required to isolate fractures and determine  $J_w$  is about one hour. Thus the total time spent to produce the above results from the raw point cloud data was about 2~2.5 hours.

Seven additional cells ( $10 \times 10$  meters) were scanned using ground based LIDAR, and the point clouds from these scans were investigated to get the fracture orientation and joint waviness information. Details on the processing and the results are shown in the Appendix. In one of the cells (number 6 in the appendix), the joint waviness of one joint set was not measured because that portion of the surface was in a difficult area from which to get the cross-section information.

### C3.3 Joint Orientation: LIDAR scan vs. Manual Measurement

By using ground-based LIDAR and point cloud processing software (Split-FX), fracture orientation and joint waviness information were obtained, as described in the previous section. In this section, the extracted joint orientation information obtained by LIDAR scanning was compared with the manually measured information compiled by an experienced engineer. In general the manual measurements were made as part of cell mapping. In the results shown in this section, each cell is about 10 m x 10 m, and cell measurement usually take 15-20 minutes, followed by moving on to the next cell. There are two primary steps in cell mapping. First of all, a few minutes are spent studying the geologic structure in the cell, and in particular identifying the primary structural sets. Secondly, one measurement of orientation is made for each structural set, as well as information for rock mass classification such as small and large scale joint roughness, joint spacing, and joint alteration. All measurements are generally made at the bottom of the cell where access to the fractures is possible. Even though only one set of measurements is made for each structural set, statistical information about each set is possible when combining information from a number of neighboring cells together.

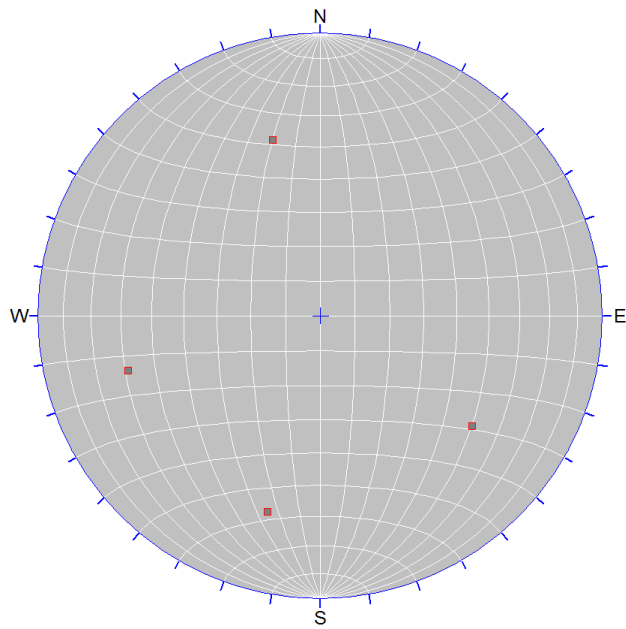
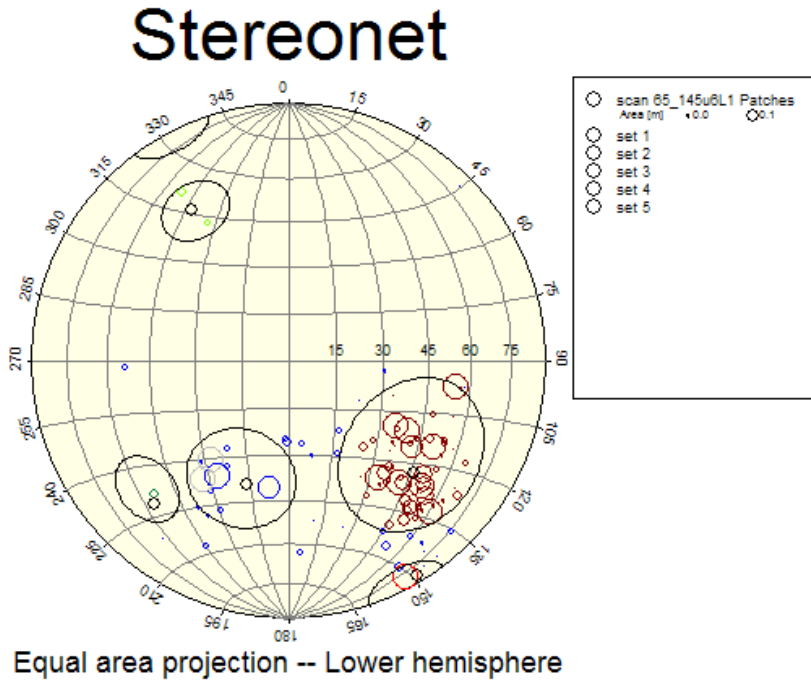


**Figure C9. LIDAR scan (upper) and manual measurement (lower)**

In Figure C9, the LIDAR results are compared with the manual measurements. It took about 20 minutes for both the laser scanning and the manual measurements in the field. Point cloud processing of the LIDAR data resulted in additional 1~1.5 hours of analysis.

During the manual cell mapping, four main joint sets were observed, resulting in four measurements of joint orientation. This can be compared with the LIDAR scan, where hundreds of fractures were delineated and these were grouped into five sets. For each of the five sets the mean orientation and the Fisher constant have been calculated. Table C5 compares the manual and LIDAR generated orientation data. Overall there is a weak correlation between the manual and LIDAR generated results. This is to be expected, since manual cell mapping is a technique for quickly obtaining data in the field, and only one measurement for each observed set is obtained. Human bias is involved in the decisions about which fractures to select for orientation measurement, and a set can be overlooked either because of time or because it is out of reach. Finally, manual orientation measurement is made with a compass that is placed on a small portion of the fracture being measured. Because of joint roughness, this location may not be representative of the average orientation of the fracture. In processing the LIDAR data, the average orientation of the entire fracture is determined, which is a more accurate measure of the fracture orientation.

**Table C5. Joint Sets Orientation Information**

LIDAR Scan			Manual measurement	
Set Name	Orientation (Strike, Dip)	Fisher K	Set Name	Orientation (Strike, Dip)
Set 1	289.1, 41.7	57	Set 1	216, 56
Set 2	57.4, 58.9	114	Set 2	344, 60
Set 3	238.9, 86.2	211	Set 3	285, 61
Set 4	313.4, 65.1	175	Set 4	75, 54
Set 5	221.9, 54.5	31		

So overall, the results of this one cell indicated that there are differences between manual cell mapping and LIDAR scanning. The time spent in the field is about the same, even though direct access to the rock face is not required in the case of LIDAR scanning, which increases safety. Extra time is required to process the LIDAR data, but this seems justified given the much more complete data set that results from point cloud processing. Seven additional cells ( $10 \times 10$  meters) were investigated both with ground based LIDAR and manual measurement. These results are presented in the Appendix.

#### **C4. Rock Mass Classification Using Ground-Based LIDAR and Point Cloud Processing**

As presented in the previous sections, block size and joint waviness parameters were determined by using two new field technologies at the bench face, image processing of digital images and point cloud processing of ground-based LIDAR scans. In this section, these results are applied to the estimation of GSI, which can then be used to estimate rock mass strength.

Manual measurements of rock mass classification have also been made based on cell mapping that was conducted in the same locations as where digital images and LIDAR scans were taken. However, the cell mapping that was conducted collected the information necessary to determine “Q” [7] rather than GSI. Q is a popular rock mass classification scheme, as described in [8]. It is difficult to use the raw cell mapping data to calculate GSI rather than Q, since the individual parameters that are measured in the field were designed specifically to calculate Q. The alternative is to convert the Q values to GSI using empirical relationships. Even though this is not ideal (and in general not recommended in practice), in this section, we compare manually generated GSI values (converted from Q values) to GSI values determined from digital imaging and LIDAR scanning of the rock faces.

#### C4.1 Manual Geological Cell Mapping (Manual GSI)

Manual cell mapping has been performed by an experienced geological engineer in a hard rock mine, and the data from the cell mapping have been used to determine Q values. In this study, the data from eight cells are used, and each cell has dimensions about 10 m × 10 m (Height × Width).

The Q system refers to the quality index developed by Barton [7]. It was originally developed for tunneling to determine tunnel stability as well as support requirements. It is now a popular rock mass classification scheme used worldwide for both underground and surface excavations. The Q system consists of the following six terms:

$$Q = \left( \frac{RQD}{J_n} \right) \times \left( \frac{J_r}{J_a} \right) \times \left( \frac{J_w}{SRF} \right) \quad (\text{Equation 1})$$

Where,

$RQD$  is rock quality designation.

$J_a$  is the joint set number.

$J_r$  is the joint roughness number.

$J_a$  is the joint alteration number.

$J_w$  is the joint water reduction factor.

$SRF$  is the stress reduction factor.

For each of the eight cells where manual cell mapping was conducted, Table C6 lists the values of the six parameters that were collected. Note that one of the parameters, RQD, is based on drill core and cannot be measured directly from cell mapping. The RQD values were determined using an empirical relationship between RQD and volumetric joint count [23,24].

**Table C6. Rock Mass Classification (Q-system) by manual cell mapping**

Cell Number	RQD	$J_n$	$J_r$	$J_a$	$J_w$	SRF	Q
1	45	9	1.5	1	1	2.5	3
2	40	12	1.5	1	1	1.5	3.3
3	35	12	1.5	1	1	5	0.9
4	55	9	1.5	2	1	2.5	1.8
5	50	12	1.5	1	1	5	1.3
6	70	9	1	1	1	2.5	3.1
7	50	9	1.5	1	1	2.5	3.3
8	45	9	1.5	1	1	2.5	3

These Q values are now converted to GSI values so they can be compared with the data from image processing and LIDAR scanning. A number of relationships between RMR

and Q have been developed [25], and Table C7 lists 10 of these relationships. Both the RMR and GSI are rock mass classification schemes based on a scale from 0 to 100, so the assumption is made that these same relationships can be used to convert Q to GSI (i.e., GSI approximately equal to RMR). We use the average of all 10 relationships to convert the manual Q measurements in the eight cells to GSI values. The results are presented in Table C7. Table C7 shows that for the eight cells, GSI values ranging from 46 to 57 have been estimated. These results will be compared with the GSI values determined from image processing and LIDAR scanning.

**Table C7. Various correlations among the rock mass classifications [25]**

Cell Number	#1	#2	#3	#4	#5	#6	#7	#8
"Q" Values Correlations (researchers)	3.0	3.3	0.9	1.8	1.3	3.1	3.3	3.0
RMR=9lnQ+44 (Bieniawski, 1976) [26]	53.9	54.7	43.1	49.3	46.4	54.2	54.7	53.9
RMR=5.9 ln Q+43 (Rutledge and Preston, 1978) [27]	49.5	50.0	42.4	46.5	44.5	49.7	50.0	49.5
RMR=5.4lnQ+55.2 (Moreno, 1980) [28]	61.1	61.6	54.6	58.4	56.6	61.3	61.6	61.1
RMR=5lnQ+60.8 (Cameron-clarke and Budavari, 1981) [29]	66.3	66.8	60.3	63.7	62.1	66.5	66.8	66.3
RMR=10.5lnQ+41.8 (Abad et al., 1984) [30]	53.3	54.3	40.7	48.0	44.6	53.7	54.3	53.3
RMR=8.7lnQ+38 (Kaiser and Gale, 1985) [31]	47.6	48.4	37.1	43.1	40.3	47.8	48.4	47.6
RMR=9lnQ+49 (Al-Harthi, 1993) [32]	58.9	59.7	48.1	54.3	51.4	59.2	59.7	58.9
RMR=15lnQ+50 (Barton, 1995) [33]	66.5	67.9	48.4	58.8	53.9	67.0	67.9	66.5
RMR=7lnQ+36 (Tuğrul, 1998) [34]	43.7	44.4	35.3	40.1	37.8	43.9	44.4	43.7
RMR=6.4lnQ+49.6 (Kumar et al., 2004) [35]	56.6	57.2	48.9	53.4	51.3	56.8	57.2	56.6
AVERAGE RMR (GSI)	55.7	56.5	45.9	51.6	48.9	56.0	56.5	55.7

#### C4.2 Automated geological cell mapping by using new technologies (Automated GSI)

Block size from the bench face was measured by using image processing software, as reported in the previous section, and the 50% passing size (F50) in the cumulative size distribution was used as a representative (average) size of the bench block sizes in this

study. The average bench block sizes (F50s) for the eight geological cells are shown in Table C8.

In addition, joint waviness for each joint set was measured using ground-based LIDAR, and the average joint waviness value Jw for each cell was calculated. The detailed joint waviness estimation data at each cell is given in the Appendix.

There are two parameters needed to estimate GSI that were not determined from image processing or LIDAR scanning. These are the joint smoothness ( $J_s$ ) and the joint alteration ( $J_a$ ). As it turned out, these parameters were measured as part of the manual cell mapping. In particular,  $J_s$  in the GSI is same as the joint roughness ( $J_r$ ) in the Q-system in Table C6 [1], and joint alteration ( $J_a$ ) in the GSI is the same as the joint alteration in the Q system as given in Table C6. There still remains the question of how these parameters would be estimated in the absence of manual cell mapping data, and this is the subject of future studies. For this study, joint smoothness ( $J_s$ ) and joint alteration ( $J_a$ ) values in Table C8 are taken to be the same as those in Table 6.

**Table C8. GSI values by using 3D laser image and image processing software**

<b>Cell Number</b>	<b>F50 (cm)</b>	<b><math>J_s</math></b>	<b>Jw (minimum)</b>	<b><math>J_a</math></b>	<b><math>J_c</math> (minimum)</b>	<b>GSI (minimum)</b>
<b>1</b>	22	1.5	2.00 (1.50)	1	3.0 (2.3)	<b>55.0 (52.5)</b>
<b>2</b>	26	1.5	1.92 (1.50)	1	2.9 (2.3)	<b>57.0 (54.0)</b>
<b>3</b>	20	1.5	1.80 (1.50)	1	2.7 (2.3)	<b>52.5 (52.0)</b>
<b>4</b>	21	1.5	1.90 (1.50)	2	1.4 (1.1)	<b>47.0 (44.0)</b>
<b>5</b>	23	1.5	1.90 (1.50)	1	2.9 (2.3)	<b>55.0 (53.0)</b>
<b>6</b>	28	1.0	2.00 (2.00)	1	2.0 (2.0)	<b>54.0 (54.0)</b>
<b>7</b>	27	1.5	1.92 (1.50)	1	2.9 (2.3)	<b>58.0 (55.0)</b>
<b>8</b>	23	1.5	2.00 (2.00)	1	3.0 (3.0)	<b>56.0 (56.0)</b>

Table C8 shows the estimated GSI values determined using the modified GSI as given by Cai et al. [1]. The four parameters needed, F50, Js, Jw and Ja, were determined from image processing (F50), ground-based LIDAR (Jw) and from the manual cell mapping (Js and Ja), as described in previous sections.

GSI values were calculated two ways, using the average joint waviness for each cell, or using the minimum joint waviness for each cell. Recall that using the LIDAR data, joint waviness is determined for each joint set in each cell. It is not clear which approach should be used, and each approach (using average or using minimum) has some logic behind it. As sliding usually occurs along the smoothest joint face (least shear strength), it makes sense to utilize the minimum GSI values when analyzing the data in terms of slope stability.

The average “minimum GSI” is 52.6, compared with the average “average GSI” of 54.3. Even though this difference is small, it can be important in deciding the slope angle in a hard rock mine. In general slopes are made as steep as possible to optimize stripping ratios and waste extraction. Thus, ground-based LIDAR allows the collection of a complete set of data in a cell, and the minimum GSI values can then be chosen for slope design. Due to time and access constraints, this approach would not be possible using conventional techniques, and is one of the benefits of using new technologies like ground-based LIDAR for rock mass characterization.

#### C4.3 Comparison between the manual GSI and the automated GSI

A comparison between the automated GSI and the manual GSI was made using manual GSI values shown in Table C7, and automated GSI values in Table C8. This comparison is shown in Figure C10.

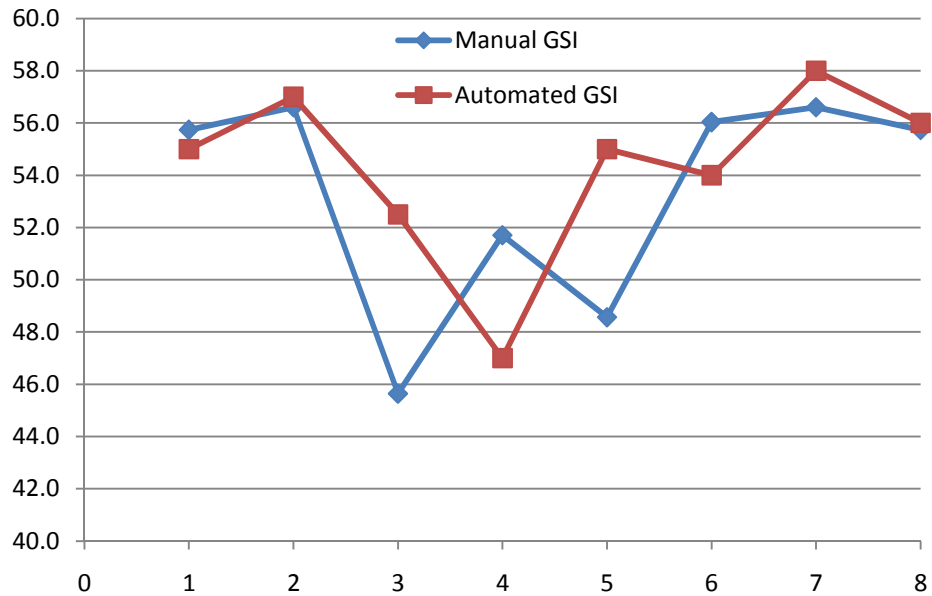


**Figure C10. Manual GSI and automated GSI**

Figure C10 shows a fair correlation between manual and automated GSI. The range of GSI in both methods is similar, as well as the averages of 53.3 ( $\pm 4.2$ ) and 54.3 ( $\pm 3.4$ ) for the manual GSI and automated GSI, respectively. In several cases, trends in the manual GSI do not correlate with trends in the automated GSI. For example, in comparing the rock mass strength of cell 3 and 4, in the manual GSI, cell 4 shows stronger rock mass strength (51.7) than cell 3 (45.6), whereas, in the automated GSI, cell 4 shows weaker rock mass strength (47.0) than cell 3 (52.5). Therefore, the relative strength of both

methods is reversed for cells 3 and 4. This reversion is shown at cells 4 & 5 and cells 5 & 6. In addition, the variance range between the manual GSIs and the automated GSIs is from 0.3 to 6.9 and the difference is not negligible in the applications of rock mass classification, such as in deciding slope angle and in analyzing slope stability.

## C5. Conclusion and Discussion

In this study, standard cell mapping was compared with an automated method based on two new technologies for field data collection, image processing of digital images and point cloud processing of ground-based LIDAR scans.

To obtain the average block size, which is one of the parameters used to estimate the GSI rock mass classification number, digital images from a bench face in a surface mine and a highway rock slope image were investigated. Because of shadows in the image and resolution, the average block size (F50) from the highway rock slope image showed a relatively large variance compared with the manually measured average block size, whereas the variance of F50 from the bench face image was small. Therefore, if some issues in the capture of digital images are avoided, then utilizing digital image processing will provide a consistent block size of the bench face quickly and safely, and more importantly, it will mitigate human bias. It should be emphasized that users need to be cautious and make sure of the condition of the bench face before capturing and processing digital images. If the bench face surface conditions are insufficient, then the results will be erroneous as the image analysis software can only process what is seen.

Also the digital images should be taken at a scale that is appropriate to clearly see the geologic structure.

For generating 3D point clouds there are two main technologies: LIDAR and photogrammetry. In this study, the ground-based LIDAR technology was used for the 3D imaging even though photogrammetry could also be appropriate for this type of problem. In both cases the results can be analyzed using point cloud processing software. The field equipment for photogrammetry can be less expensive, but in general the processing of photogrammetry data requires additional time and expertise. This study found that an accurate and complete measurement of joint waviness is one of the benefits of using LIDAR. Joint waviness is one of the four parameters in the modified GSI of Cai et al. [1], and therefore very important in the analysis of rock mass strength and slope stability. Like joint orientation, joint waviness varies from location to location and from joint set to joint set, and this study showed that it may be more appropriate to consider the minimum rather than the average joint waviness when considering the application to slope stability. This emphasizes the importance of gathering sufficient data on large-scale roughness from new technologies such as LIDAR, rather than just quickly gathering a few pieces of information as is the case in manual cell mapping.

In this study, manual GSI was determined based on manual cell mapping conducted by an experienced geological engineer, and the automated GSI was measured using the new technologies of image processing and 3D laser imaging. Both GSI values, manual GSI

and the automated GSI, were compared, and there was a fair correlation between the two. This is to be expected, since manual cell mapping is a technique for quickly obtaining data in the field, and only very limited measurements are made, and with limited access. The eight cells where the GSI were compared had a variation in GSI from about 46-57. In the future, it would be useful to compare automated and manual GSI over a larger range of GSI.

The optimum slope angle is one of the key factors in increasing economic efficiency in a hard rock mine; the goal of geological analysis is not to increase the allowable slope angle, but to optimize the slope angle. If the actual slope angle is greater than the optimum angle, it can decrease mine production by causing many mine safety issues. Furthermore, if the angle is lower than the optimum one, then it increases the expense of mine production as the waste extraction is increased. We believe that the new technologies can produce more reliable geological raw data, and optimization of the slope angle is possible only if reliable raw data are obtained from the field. Thus, applying the recent technologies to rock mass classification can be very beneficial economically. More study is needed on this as well since rock mass classification is still a challenging research area.

Mapping data from eight cells were used for comparison between the manual cell mapping and the automated cell mapping (that used 3D laser imaging and the processing program). The geometry of each cell is roughly  $10 \times 10$  (meters). Time consumption is

less than 30 minutes in the field for both manual cell mapping and LIDAR scanning, but additional hours are required for 3D laser image data processing (the additional time for processing the data varies depending on the application the user wants to utilize). In this study, the total time spent for 3D laser imaging and analysis was about 2~2.5 hours for various applications: delineating fractures, creating stereo nets, measuring joint waviness, and obtaining joint set information, which includes average strike, dip, and the Fisher constant K (a measure of scatter). We believe that the new technology (3D laser imaging) produces reliable, objective, and consistent data, although this takes additional processing time. If some errors result from 3D laser imaging, most of these errors occur because of steps in the user's point cloud processing, and these can be fixed by processing the data again with the existing point clouds. Similarly if a new type of analysis is to be conducted at a field site, the existing point clouds from that site can be reprocessed to generate new types of results. This points out the importance of collecting LIDAR scanning data with as much accuracy as possible. Recommendations on best practices for field LIDAR scanning are given in Kemeny and Turner (2008) [36].

In conclusion, applying the latest technologies of geological mapping of hard rock mining sites can contribute significantly to mine safety and economics, and increasing the efficiency of collecting geological data.

## References

- [1] Cai, M.; Kaiser, P.K.; Uno, H.; Tasaka, Y.; Minami M. (2004) Estimation of rock mass deformation modulus and strength of jointed hard rock masses using the GSI system, *Int. J Rock Mech Min Sci* 41:3-19
- [2] Edelbro, Cartin (2003) Rock mass strength (a review), *Technical Report, Division of Rock Mechanics, Department of Civil Engineering, LULEÅ University of Technology*
- [3] Krauland, N.; Söder, P.; Agmalm, G. (1989) Determination of rock mass strength by rock mass classification-some experience and questions from Boliden mines, *Int. J Rock Mech. Min. Sci* 26(1):115-123
- [4] Bieniawski, Z. T. (1976) Engineering classification in rock engineering. In: *Proceedings of the Symposium on Exploration for Rock Engineering, Johannesburg*, 97-106
- [5] Stille, H. Groth, T. and Fredriksson, A. (1982). FEM- analysis of rock mechanical problems with JOBFEM, *stiftelsen Bergteknisk Forskning- BeFo, Stockholm*, 307:1/82.
- [6] Palmström, A. (1996) Characterizing rock masses by the *RMi* for Use in Practical Rock Engineering, *Tunnelling and Underground Space Technology*, Vol.11 No.2 pp. 176-188.
- [7] Hoek, E. and Brown, E. T. (1997) Practical estimates of rock mass strength. *Int. J. Rock. Mech. Min.*, 34 (8), 1165-1186
- [8] Barton N, Lien NR, Lunde J (1974) Engineering classification of rock masses for the design of tunnel support. *Rock Mech* 6(4): 189-236

- [9] Laubscher, D. H. (1984) Design aspects and effectiveness of support systems in different mining conditions, *T. I. Min. Metall. A.* 93, A70-A81.
- [10] Kim, K.M. and Kemeny, John (2011) Site Specific Blasting Model Using Schmidt Tensile Strength and Image Analysis, *International Society of Explosives Engineer (ISEE), San Diego*
- [11] Kim, K.M. and Kemeny, John (2011) Site Specific Blasting Model for Mine-to-Mill Optimization, *Transactions of the Society for Mining, Metallurgy and Engineering*, Vol.330. PP. 543-548
- [12] Split Engineering LLC., [www.spliteng.com](http://www.spliteng.com)
- [13] Kim, K.M., 2006, Blasting design using fracture toughness and image analysis of the bench face and muckpile, *Master of Science thesis, Mining and Mineral Engineering, Virginia Tech, Blacksburg, USA*
- [14] Dahlhielm, S. (1996) Industrial applications of image analysis – The IPACS system *Proceeding Measurement of Blast Fragmentation, Balkema, Rotterdam*
- [15] Havermann, T., Vogt W. (1996) TUCIPS- A system for the estimation of fragmentation after production blasts *Proceeding Measurement of Blast Fragmentation, Balkema, Rotterdam*
- [16] Schleifer, J., Tessier, B. (1996) FRAGSCAN: A tool to measure fragmentation of blasted rock *Proceeding Measurement of Blast Fragmentation, Balkema, Rotterdam*
- [17] Maerz, N. H., Palangio, T. C., Franklin, J. A. (1996) WipFrag image based granulometry system *Proceeding Measurement of Blast Fragmentation, Balkema, Rotterdam*

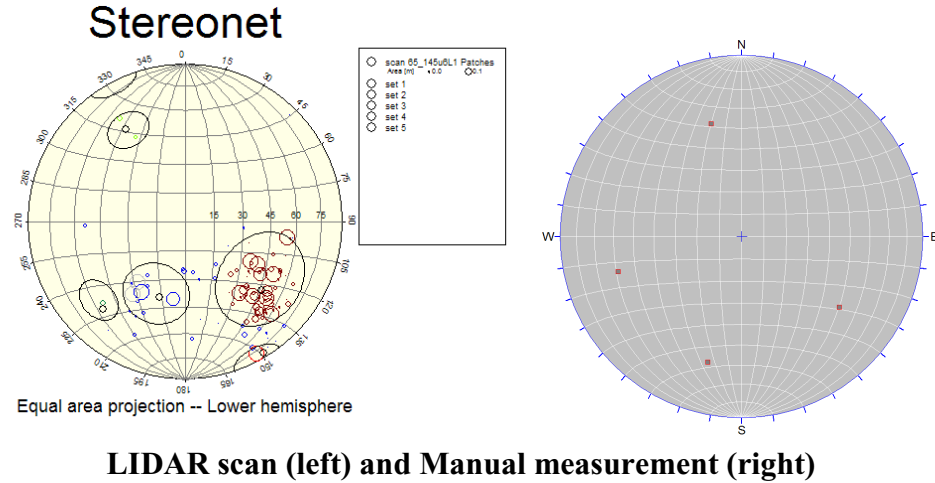
- [18] Rasband, Wayne. (2004). Image J
- [19] Gonzalez, R. C.; Woods, R. E.; Eddin, S. L. (2003) Digital image processing using MATLAB, *Pearson Prentice Hall*
- [20] Kemeny, John; Turner, Keith; Norton, Brian (2006) LIDAR for rock mass characterization: Hardware, Software, Accuracy and Best-Practices, *In: Proc. Of American Rock Mechanics Association conference, Golden, Colorado*
- [21] Prokop, A., Panholzer, H. (2009) Assessing the capability of terrestrial laser scanning for monitoring slow moving landslides, *Nat. Hazards Earth Syst. Sci.*, 9, 1921-1928
- [22] Hoek, E., Bray, J. D. (1981) Rock slope engineering (3<sup>rd</sup> edition), *CRC Press*
- [23] Deere, D. U. (1968) Geological consideration. *In: Rock mechanics in engineering practice, Division of Civil Engineering, School of Engineering, University of Wales, Swansea, John Wiley& sons, New York, 1-20*
- [24] Deere, D. U. and Deere, D. W. (1998) The rock quality designation (RQD) index in Practice. *In: Rock Classification System for Engineering Purposes*
- [25] Hashemi, M., Moghaddas, Sh., Ajalloeian, R. (2010) Application of rock mass characterization for determining the mechanical properties of rock mass: a comparative study. *Rock Mech Rock Eng.* 43:305-320
- [26] Bieniawski ZT (1973) Engineering classification of jointed rock masses. *Trans S Afr Inst Civil Eng.* 15(12): 335-344
- [27] Rutledge JC, Preston RL (1978) Experience with engineering classifications of rock. *In: Proc. Int. Tunnelling Symp. Tokyo, A3.1-A3.7*

- [28] TE, Moreno (1980) Application de las clasificaciones geomecánicas a los túneles de parajes. *11 Cursode Sostenimientos Activos en Galerías y Túneles. Foundation Gomez Parto, Madrid*
- [29] IS, Cameron-Clarke, S., Budavari (1981) Correlation of rock mass classification parameters obtained from borecore and in situ observations. *Eng Geol* 17:19–53
- [30] J., Abad, B., Caleda, E., Chacon, V., Gutierrez, E., Hidlgo (1984) Application of geomechanical classification to predict the convergence of coal mine galleries and to design their supports. *In: 5th Inter. Cong. Rock Mech., Melbourne*, pp 15–19
- [31] TK., Kaiser, AD., Gale (1985) Evaluation of Cost and Empirical Support Design at B.C. Rail Tumbler Ridge Tunnels. Canadian Tunnelling, *Tunnelling Association of Canada, Wiley, New York*, pp 77–106
- [32] AA., Al-Harthi (1993) Application of CSIR and NGI classification systems along tunnel no. 3 at Al-Dela Descant, Asir Province, Saudi Arabia. *In: Cripps JC, Coulthard JM, Culshaw MG, Forster A, Hencher SR, Moon CF (eds) The Engineering geology of weak rock. Balkema, Rotterdam*, pp 323–328
- [33] N., Barton (1995) The influence of joint properties in modelling jointed rock masses. Keynote Lecture. *In: 8th Cong. ISRM, Tokyo*
- [34] A., Tuğrul (1998) The application of rock mass classification systems to underground excavation in weak limestone, Ataturk dam. *Turkey Eng Geol* 50:337–345
- [35] N., Kumar, NK., Samadhiya, R., Anbalagan (2004) Application of rock mass classification system for tunneling in Himalaya, *India Paper 3B 14, SINOROCK2004 Symposium. Int J Rock Mech Min Sci* 41(3):531

[36] Kemeny, J. and K., Turner. (2008). Ground-Based LiDAR: Rock Slope Mapping and Assessment, *Report FHWA-CFL/TD-08-006, Federal Highway Administration Central Federal Lands Highway Division, Lakewood, CO*

## Appendix

### Cell Mapping 1



### Joint Orientation analysis by using LIDAR and Manual measurement

LIDAR Scan			Manual measurement	
Set Name	Orientation (Strike, Dip)	Fisher K	Set Name	Orientation (Strike, Dip)
Set 1	289.1, 41.7	57	Set 1	216, 56
Set 2	57.4, 58.9	114	Set 2	344, 60
Set 3	238.9, 86.2	211	Set 3	285, 61
Set 4	313.4, 65.1	175	Set 4	75, 54
Set 5	221.9, 54.5	31		

### Joint Waviness measurement by using LIDAR scan

Set Number	Joint Waviness (Jw)
Set 1	2.0 (3.6, 2.86%)
Set 2	2.0 (4.43%)
Set 3	1.5 (2.17, 1.67%)
Set 4	2.0 (3.10, 3.5%)
Set 5	2.5 (12, 13.6%)
Average	2.0 (Min. 1.5 ~ Max. 2.5)

## Cell Mapping 2

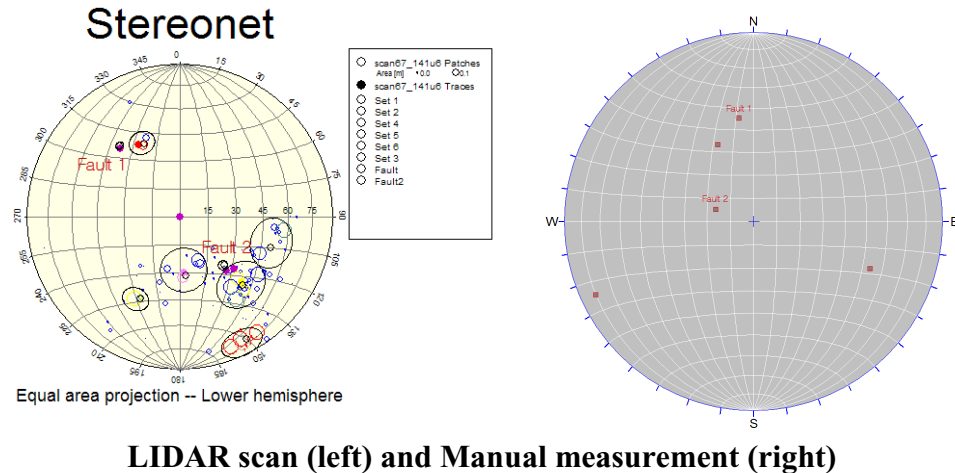


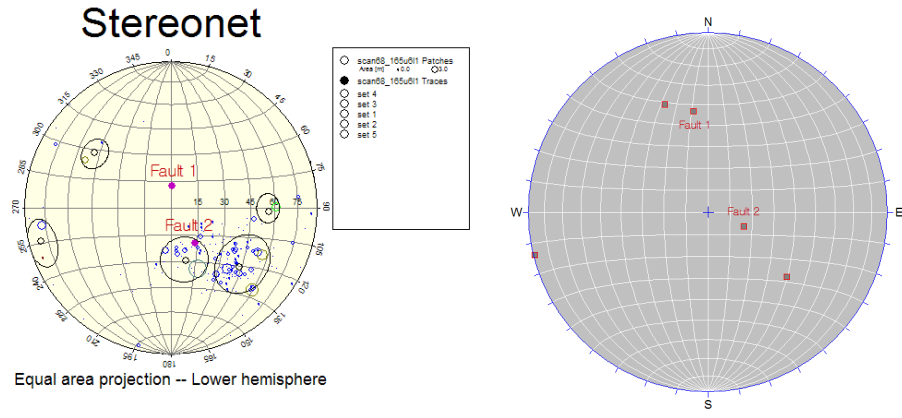
**Table. Joint Orientation analysis by using LIDAR and Manual measurement**

LIDAR Scan			Manual measurement	
Set Name	Orientation (Strike, Dip)	Fisher K	Set Name	Orientation (Strike, Dip)
Set 1	64.3, 44.3	290	Set 1	335, 81
Set 2	227.4, 50.8	89	Set 2	202, 56
Set 3	198.5, 52.5	95	Set 3	65, 37
Set 4	295.9, 50.0	557	Fault 1	82, 46
Set 5	264.2, 31.5	109	Fault 2	18, 17
Set 6	241.4, 79.8	209		
Fault 1	49.8, 51.2			
Fault 2	227.7, 35.1			

### Joint Waviness measurement by using LIDAR scan

Set Number	Joint Waviness (Jw)
Set 1	1.5 (1.6%)
Set 2	2.0 (7.6, 7.1, 2.1%)
Set 3	2.0 (5.4, 8.8%)
Set 4	2.0 (2.4, 6.1%)
Set 5	2.0 (3.4, 6.25%)
Set 6	2.0 (3.9, 5.02%)
Average	1.92 (Min. 1.5 ~ Max. 2.0)

### Cell Mapping 3



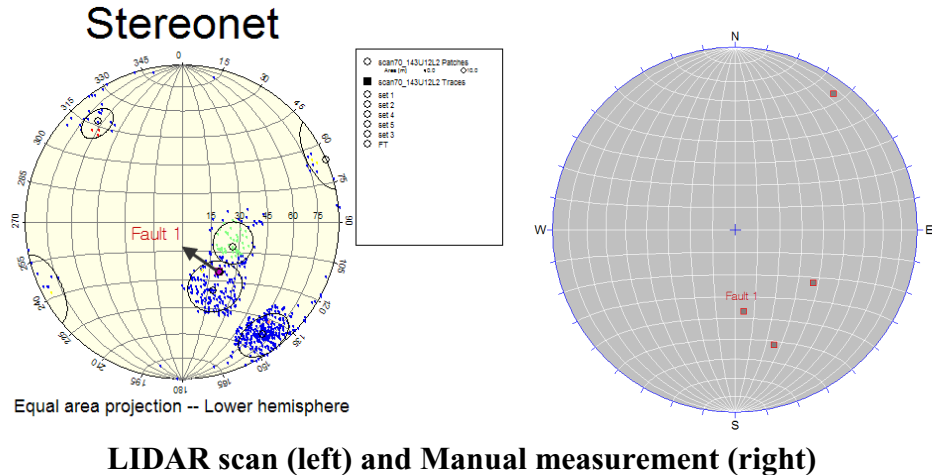
#### Joint Orientation analysis by using LIDAR and Manual measurement

LIDAR Scan			Manual measurement	
Set Name	Orientation (Strike, Dip)	Fisher K	Set Name	Orientation (Strike, Dip)
Set 1	345.7, 80.8	62	Set 1	219, 47
Set 2	182.4, 56.2	296	Set 2	346, 87
Set 3	254.0, 30.7	82	Set 3	69, 53
Set 4	220.7, 51.3	62	Fault 1	82, 46
Set 5	36.1, 54.1	229	Fault 2	201, 17
Fault 1	84.4, 13.9			
Fault 2	236.5, 25.7			

#### Joint Waviness measurement by using LIDAR scan

Set Number	Joint Waviness (Jw)
Set 1	1.5 (2.98, 2.38, 2.81%)
Set2	2.0 (4.0, 6.2%)
Set 3	2.0 (2.43, 3.75, 3.93%)
Set 4	2.0 (6.19, 4.78%)
Set 5	1.5 (1.72, 3.26, 2.11%)
Average	1.80 (Min. 1.5 ~ Max. 2.0)

## Cell Mapping 4



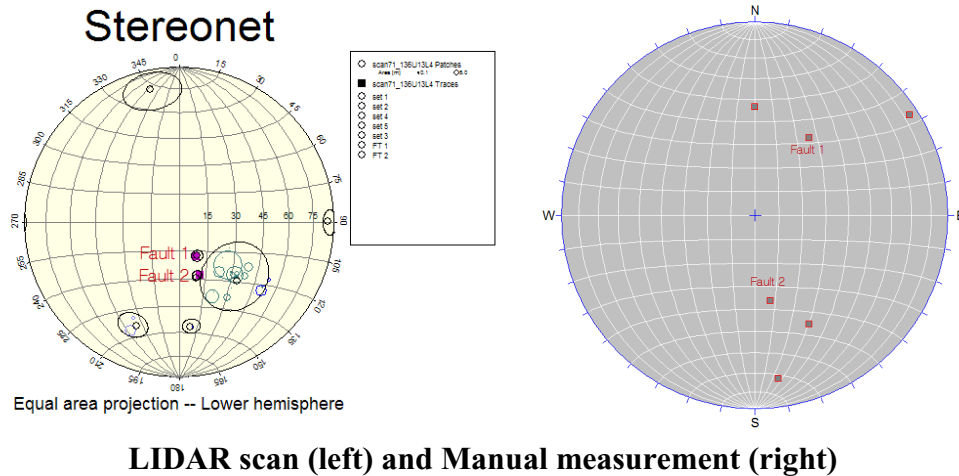
### Joint Orientation analysis by using LIDAR and Manual measurement

LIDAR Scan			Manual measurement	
Set Name	Orientation (Strike, Dip)	Fisher K	Set Name	Orientation (Strike, Dip)
Set 1	156.6, 89.1	74	Set 1	214, 43
Set 2	245.7, 39.1	76	Set 2	251, 56
Set 3	234.4, 76.7	132	Set 3	126, 81
Set 4	50.0, 72.4	200	Fault 1	264, 37
Set 5	206.2, 29.0	135		
Fault 1	233.7, 32.1			

### Joint Waviness measurement by using LIDAR scan

Set Number	Joint Waviness (Jw)
Set 1	1.5 (3.18, 2.67, 2.13%)
Set 2	2.0 (10.61, 2.38, 8.68%)
Set 3	2.0 (9.20, 3.47, 2.84%)
Set 4	2.0 (2.13, 4.44, 3.02%)
Set 5	2.0 (5.17, 5.56, 7.18%)
Average	1.90 (Min. 1.5 ~ Max. 2.0)

## Cell Mapping 5



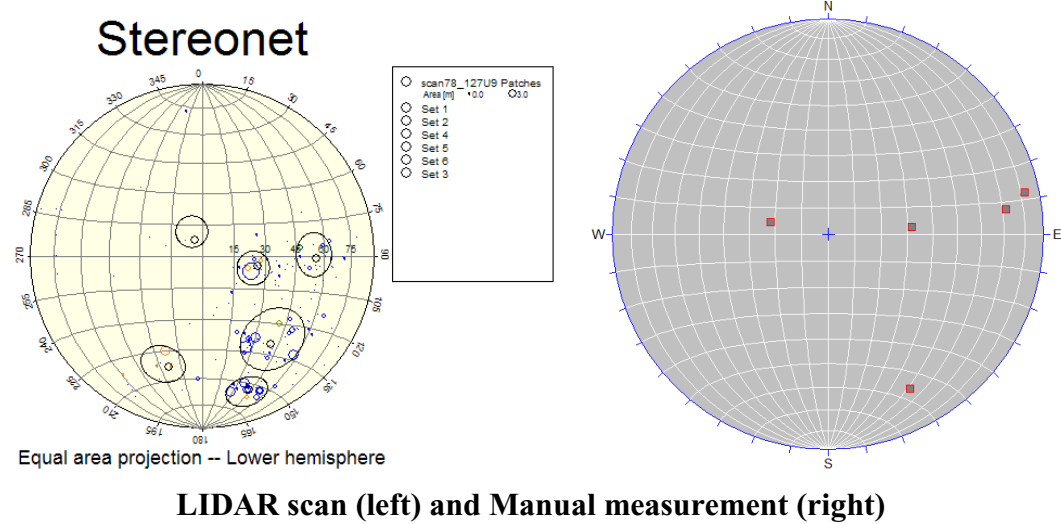
### Joint Orientation analysis by using LIDAR and Manual measurement

LIDAR Scan			Manual measurement	
Set Name	Orientation (Strike, Dip)	Fisher K	Set Name	Orientation (Strike, Dip)
Set 1	225.7, 43.9	47	Set 1	242, 53
Set 2	292.7, 61.5	255	Set 2	263, 73
Set 3	264.0, 57.3	803	Set 3	91, 46
Set 4	77.7, 76.5	77	Set 4	146, 89
Set 5	179.5, 85.4	677	Fault 1	126, 42
Fault 1	242.1, 19.7		Fault 2	258, 36
Fault 2	253.0, 30.6			

### Joint Waviness measurement by using LIDAR scan

Set Number	Joint Waviness (Jw)
Set 1	2.0 (7.09, 19.09, 7.87%)
Set 2	2.0 (6.30, 7.26%)
Set 3	2.0 (3.63, 2.90, 2.63%)
Set 4	2.0 (3.77, 3.97%)
Set 5	1.5 (2.85%)
Average	1.90 (Min. 1.5 ~ Max. 2.0)

## Cell Mapping 6



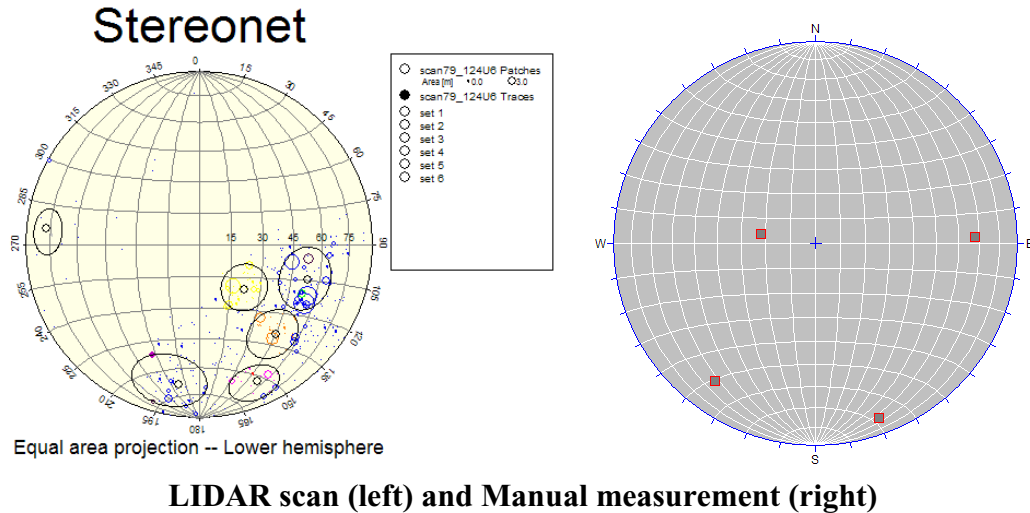
### Joint Orientation analysis by using LIDAR and Manual measurement

LIDAR Scan			Manual measurement	
Set Name	Orientation (Strike, Dip)	Fisher K	Set Name	Orientation (Strike, Dip)
Set 1	190.3, 26.6	286	Set 1	242, 70
Set 2	250.5, 70.8	286	Set 2	168, 82
Set 3	231.9, 54.3	70	Set 3	12, 22
Set 4	287.1, 56.5	187	Set 4	175, 32
Set 5	180.8, 55.4	174	Set 5	172, 72
Set 6	62.7, 8.3	185		

### Joint Waviness measurement by using LIDAR scan

Set Number	Joint Waviness (Jw)
Set 1	2.0 (5.29, 3.00, 4.33%)
Set2	2.0 (7.74, 4.13, 7.30%)
Set 3	2.0 (4.52, 4.50, 2.68%)
Set 4	2.0 (4.30, 2.63, 4.93%)
Set 5	2.0 (6.00, 6.63, 3.67%)
Average	2.0 (Min. 2.0 ~ Max. 2.0)

## Cell Mapping 7



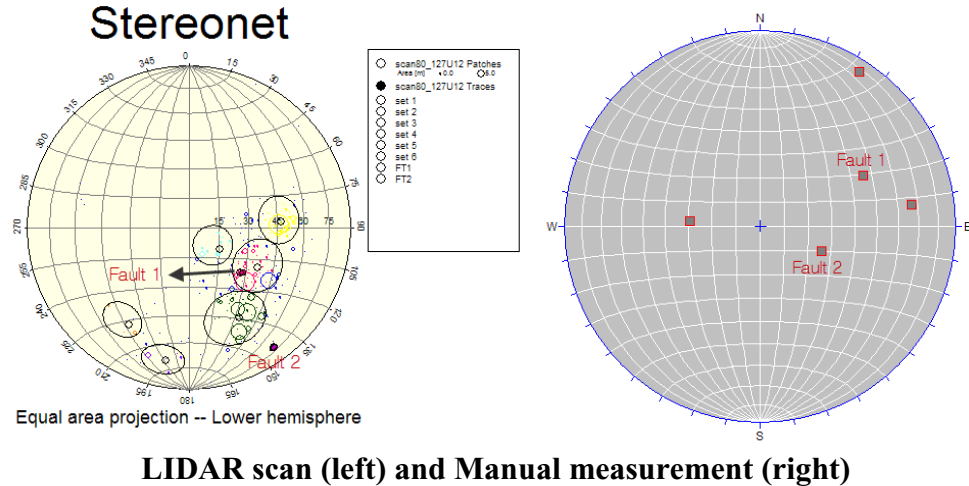
### Joint Orientation analysis by using LIDAR and Manual measurement

LIDAR Scan			Manual measurement	
Set Name	Orientation (Strike, Dip)	Fisher K	Set Name	Orientation (Strike, Dip)
Set 1	278.7, 70.1	84	Set 1	250, 81
Set 2	198.0, 55.4	71	Set 2	306, 73
Set 3	225.3, 29.9	126	Set 3	178, 68
Set 4	229.5, 56.9	110	Set 4	10, 22
Set 5	6.0, 77.2	275		
Set 6	247.2, 74.2	134		

### Joint Waviness measurement by using LIDAR scan

Set Number	Joint Waviness (Jw)
Set 1	1.5 (2.55, 3.59, 1.69%)
Set2	2.0 (2.65, 8.64, 8.75%)
Set 3	2.0 (7.77, 5.54, 4.52%)
Set 4	2.0 (2.67, 5.83, 6.86%)
Set 5	2.0 (8.80, 8.46%)
Set 6	2.0 (4.29, 7.81, 6.41%)
Average	1.92 (Min. 1.5 ~ Max. 2.0)

## Cell Mapping 8



### Joint Orientation analysis by using LIDAR and Manual measurement

LIDAR Scan			Manual measurement	
Set Name	Orientation (Strike, Dip)	Fisher K	Set Name	Orientation (Strike, Dip)
Set 1	241.0, 53.0	62	Set 1	123, 83
Set 2	301.8, 59.9	131	Set 2	172, 67
Set 3	176.1, 47.3	125	Set 3	004, 29
Set 4	210.1, 40.6	77	Fault 1	202, 28
Set 5	215.3, 18.6	175	Fault 2	154, 49
Set 6	280.0, 71.6	169		
Fault 1	221.3, 34.7			
Fault 2	234.7, 79.4			

### Joint Waviness measurement by using LIDAR scan

Set Number	Joint Waviness (Jw)
Set 1	2.0 (10.6, 7.75, 5.72%)
Set 2	2.0 (5.15%)
Set 3	2.0 (4.11, 2.43, 8.33%)
Set 4	2.0 (4.39, 9.90, 3.89%)
Set 5	2.0 (2.90, 1.92, 5.55%)
Set 6	2.0 (1.27, 3.98, 4.73%)
Average	2.0 (Min 2.0 ~ Max. 2.0)

**APPENDIX D: BLENDING EFFECT OF MINERAL ORES ON  
FLOTATION RECOVERY IN HARD ROCK MINES**

Kim, K. M., Zhang, Jinhong and Kemeny, John  
*The University of Arizona, Tucson, AZ, U.S.A.*

SUBMITTED TO MINERALS ENGINEERING (2012)

## **BLENDING EFFECT ON MINERAL ORES ON FLOTATION RECOVERY IN HARD ROCK MINES**

Kim, K. M., Zhang, J. and Kemeny, J.  
*The University of Arizona, Tucson, AZ, U.S.A.*

### **Abstract**

As the part of the study of finding the target blast fragmentation in Mine-to-Mill Optimization, the effect of blending ores is investigated. At first, the grinding time effect on the flotation recovery of the mixture of two different ores is investigated and it is found that the “incomplete liberation” has a more pronounced impact on metal recovery than “overgrinding” does because and the metal recovery increases with the grinding time. Therefore, for a better recovery, “incomplete liberation” of the hard ores in the grinding of the blended ores should be avoided.

The “blending effect” and the optimum harmony of ores are studied further. The average recovery of six ores before blending is 79%, one after blending is 84.7%, and one with utilizing the best blending harmony is 91.3%. Therefore, the possible average increase is 5.7% after blending, and the maximum increase could be 12.3% from mixing ores by considering the best harmony of two ores. In particular, all the recoveries of actually blending two ores are higher than all the arithmetic mean recoveries. It is therefore concluded that the “blending effect” has a positive impact on the flotation recovery.

## D1. Introduction

The Mine-to-Mill optimization in mining industry can be accomplished through optimizing blast fragmentation, crusher settings, mill throughput, flotation and so on. For example, in some recent studies [1,2], it has been shown that increasing the powder factor can decrease the consumption of both crushing energy and grinding energy and the Bond's Work Index (BWI) of ore, by the precondition of rock. In addition, the ore size for the feed of flotation in a mill is one of the most important factors for the flotation recovery [3, 4, 5]. Therefore, blasting has a significant effect on the consecutive processes such as loading, hauling, crushing, grinding and flotation, and the optimized blast fragmentation can result in increasing productivity, saving energy consumption and reducing the total expense significantly. Thus, blast fragmentation needs to be optimized not only for material haulage but for comminution and mineral processing as well.

Recently, Kim and Kemeny [6, 7, 8] studied Mine-to-Mill optimization by controlling and improving the blast fragmentation and considering all downstream processes. A blast fragmentation prediction model was also proposed [6]. Generally, two main topics for the optimization of blast fragmentation have been focused upon. One is the blast control for blast fragmentation (Blast Control) and the other is finding the target fragmentation (Blast Target) at each rock type. However, in hard rock mining, rock types from different areas are often blended to provide a consistent ore grade for the mill. Thus, the effect of blending rock types needs to be investigated as the part of the study of finding the target

blast fragmentation at each rock type since blasting can be helpful to reduce the effect of mineral hardness on the combined mineral grinding, based on other researchers studies [1, 2, 9].

Yusupov (2007) studied the effect of ore hardness on the combined mineral grinding and suggested that splitting grinding circuits can mitigate the overgrinding problem of sulfide minerals, which reduces the flotation recovery [9]. At the beginning, a blending strategy was proposed to improve flotation by classifying the ore into two types, i.e. the hard ores and the soft ores, according to the difference in ore hardness. The strategy was expected to be able to decrease or even totally eliminate the problems of sliming (overgrinding of soft ores) and incomplete liberation usually observed in the grinding circuits. However, the actual test results showed that an unexpected "blending effect", instead of the ore hardness, has a predominant effect on the flotation recovery. The mechanism responsible for the "blending effect" is not completely understood. It is therefore interesting to blend ores not for the purpose of providing a consistent grade but for providing a mix that improves mineral recovery (blending effect) and optimizes energy utilization. Two topics are investigated in this study: (1) the effect of grinding time, which involves changing the feed size of flotation and (2) the effect of blending minerals on flotation recovery.

## Experimental

### D2. Sample Preparation

Six different types of ore samples are collected from a copper mine located in Arizona and labeled as ore 1 to ore 6. Each of the samples is one of six different rock types: argillite, siltstone, garnet tactite (GTT), diopside tactite (DTT), marble and green garnet.

Figure D1 shows the six collected block samples of the different rock types.

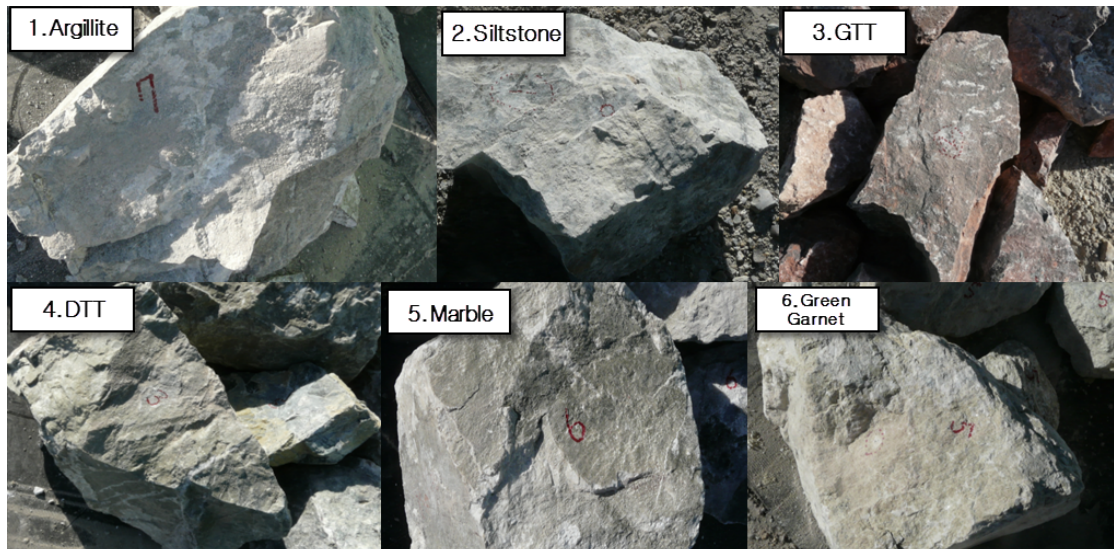


Figure D1. Six different ore samples

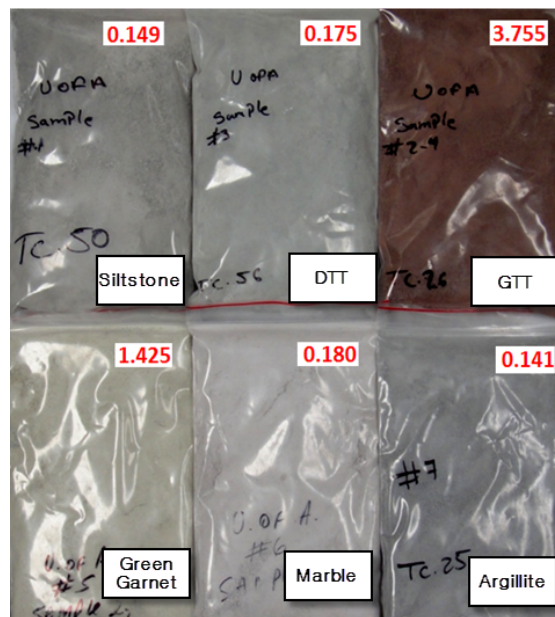
Each sample is crushed down to finer than 10 mesh, mixed uniformly and prepared as 1 kg per bag for further laboratory flotation tests. The head grade of copper and molybdenum for each sample is analyzed and the results are listed as Table D1.

**Table D1. Metal analysis of six ore samples from a copper mine**

Samples	Rock type	Cu (%)	Mo (%)
1	argillite	0.141	0.0011
2	siltstone	0.149	0.0038
3	garnet Tactite (GTT)	3.775	0.0065
4	diopside Tactite (DTT)	0.175	0.0047
5	marble	0.180	0.0002
6	green garnet	1.425	0.0003

Table D1 shows that the molybdenum grade of all the six ore samples is very low and the value is close to that of typical flotation tailings. In practice, it is not profitable to recover molybdenum from these ores and therefore the recovery of molybdenum is not considered in this study.

Figure D2 shows the prepared samples in the 1kg bag with the respective copper grade being marked on the top right of each bag.

**Figure D2. The prepared ore samples in 1 kg bag for laboratory flotation tests.**

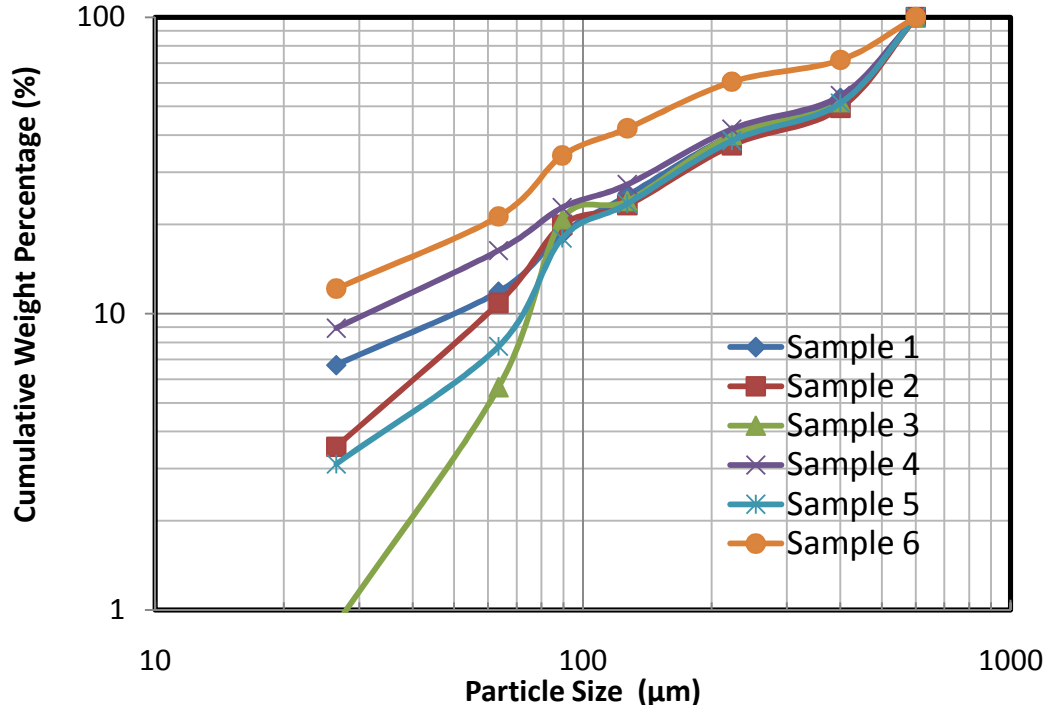
### D2.1 Flotation test

The crushed ore sample was put into a lab ball mill filled with water and further ground for a specific time, which was determined beforehand through a grinding test to make a flotation feed with 65% (in weight) finer than 100 mesh. After grinding, the pulp was transferred to a Denver D12 lab flotation cell and  $\text{Ca}(\text{OH})_2$  was added to bring the pulp pH back to 11. Preparation time was one minute with impeller string after a specific amount of frother was added into the flotation cell. The air valve was then turned on and flotation began. Flotation time in the present study was set at 6 minutes. After flotation, the concentrate and tailings were collected, filtered and dried overnight. Products were further sent out for metal analysis. Every flotation test was repeated three times and an arithmetic average metal recovery was reported. The experiment error is usually less than  $\pm 1\%$  in metal recovery.

## Experiment results and Discussion

### D3. Characterization of Ore Grindability

Before flotation, the grindability tests of six rock types are carried out to characterize the hardness of samples and determine the grinding time for flotation. At the beginning, the particle size distribution of the six ore samples is characterized by a laboratory sieving analysis test. The cumulative weight percentage of the undersize is plotted as a function of particle size and the results are shown as Figure D3.



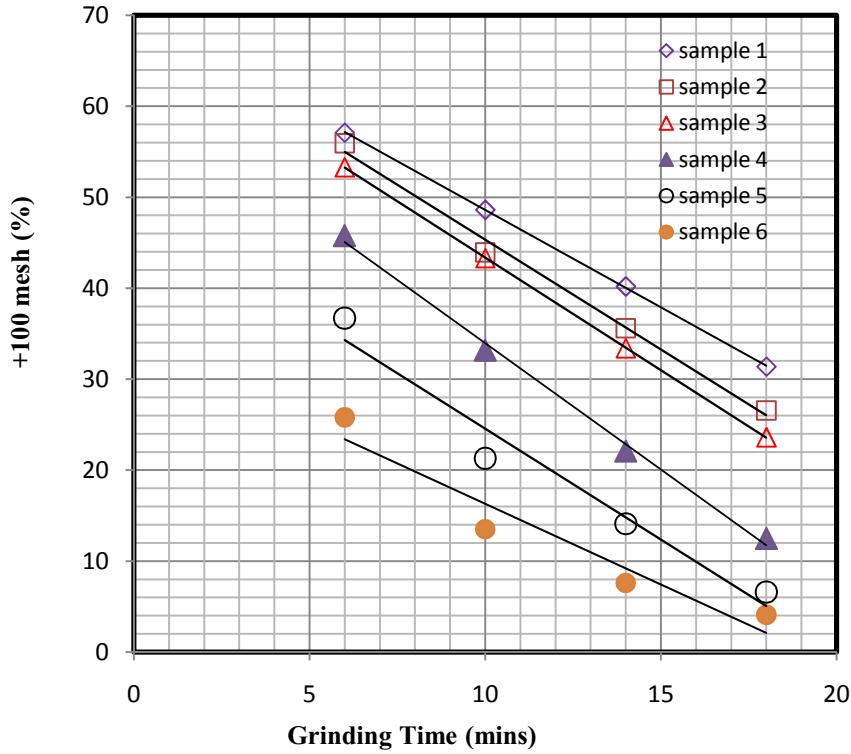
**Figure D3. Cumulative size distribution of six ore samples.**

Figure D3 shows that five samples, i.e., sample 1, 2, 3, 4 and 5, have a similar size distribution. In particular, the P80s (80% passing size at which the cumulative undersize particles is 80% in weight) and the distribution curves above the 100 microns for each of these five samples is similar. It is verified that the feed size distribution for the grindability test is consistent and the difference in the produced size distribution after grinding is mostly due to the difference in ore grindability.

It is also noted that the P80 of sample 6 is much smaller. It means that sample 6 is significantly softer than other five ore samples because the crushing processes are set with same parameters. This conclusion that sample 6 is weaker in hardness compared

with other ores and more fines will be produced in the blasting and crushing process is further confirmed by the grindability test results shown as Figure D4.

Grindability tests are conducted to investigate grindability at each rock type and to decide the proper grinding times for laboratory flotation tests. For each grinding test, one bag (1 kg) of a specific ore sample is put into an 8"x8" ball mill filled with water beforehand. The mill is then turned on and the grinding test is carried out for a specific time, e.g. 6, 10, 14 and 18 minutes. The ball mill is then removed from the mill roller. A screen with large apertures is used to separate the grinding balls from the pulp, which is further thoroughly wet-screened by a 100 mesh sieve. The oversize material is collected in a pan, further dried at 80°C in an oven and then screened for 5 minutes using a 100 mesh sieve to remove any finer particles attached on coarse particles. The total oversize material is weighed and the weight percentage of the oversize is recorded and finally plotted as Figure D4.



**Figure D4. Grindability tests at each ore type**

Figure D4 shows that the grindability of the six ores is in the following order: sample (soft) 6>5>4>3>2>1 (hard). Based on the obtained grindability, sample 1 (argillite), sample 2 (siltstone) and sample 3 (GTT) are classified as the relatively ‘hard’ ores; while sample 4 (DTT), sample 5 (marble) and sample 6 (green garnet) are classified as the relatively ‘soft’ ores. It is noted that sample 6 (green garnet) is significantly softer for grinding than other rock types, which is already shown in Figure D3.

The grinding time for each rock type is determined at 35% (in weight) being retained on 100 mesh screen for the feed of flotation and the results are as shown as Table D2.

The flotation recovery of copper for each ore type is firstly investigated as the base line for the study of the blending effect. Table D2 shows the copper recovery (%) of each ore type before blending, the ore grade and the grinding time for the flotation test obtained from Figure D4.

**Table D2. Base line flotation test results**

Ore Type	1. Argillite	2. Siltstone	3. GTT	4. DTT	5. Marble	6. Green Garnet
Cu Recovery (%)	86.9	72.2	69.9	68.2	87.0	89.8
Ore Grade (%)	0.141	0.149	3.755	0.175	0.180	1.425
Grinding Time (min)	16.5	14	13	9.5	6.5	4.5

It is noted that the copper recovery of DTT is significantly low, and it is believed that it is because DTT has a serious clay problem. More investigation is needed to determine the reason conclusively. Actually, in the mine where the samples were taken from, it is also confirmed that DTT is one of the problematic ore types with a significantly low flotation recovery.

It is therefore concluded that as the grindability of the six ores changes greatly from one to another ore type and the grinding of the mixture of both hard and soft rocks will result in either “overgrinding” of soft ore or “incomplete liberation” of hard ore, both of which may impact the flotation recovery. Therefore, a grinding process after the classification of ore type based on the ore grindability may be beneficial for a high flotation recovery, as the adverse effect of the both impacts may be mitigated by the ore classification. Thus, it was initially expected that less flotation recovery would be achieved by mixing the soft

and the hard ores compared to the classification of the blends, i.e., “soft and soft” or “hard and hard,” due to either “incomplete liberation” or “overgrinding.” However, the actual experiment shows a different result and it will be discussed further in the following section.

### D3.1 Grinding Time Effect on Flotation Recovery

As seen in the previous section, the six ore samples can be classified based on the hardness as two categories, i.e. the hard ore and the soft ore. When a hard ore is mixed with a soft ore, three different grinding times, i.e., the grinding time based on hard ores, the grinding time based on soft ores and the average grinding time, are applied in the present study. For example, if #2 siltstone (hard ore) and #4 DTT (soft ore) are mixed, the grinding time for each ore sample is 14 and 9.5 minutes respectively as shown from Figure D4. Thus, in the present blending effect study, the three grinding time are set as 14 minutes (based on hard ores), 9.5 minutes (based on soft ores) and 11.75 minutes (the average grinding time).

For the mixture of the classified ores, i.e., Hard/Hard and Soft/Soft ores, the average grinding time is used, as there is a relatively small difference between the optimum grinding time for each ore. In order to study the effect of grinding time and the blending strategy on the flotation recovery, the laboratory flotation test results with various ore grinding time are shown as Table D3 and D4.

**Table D3. Flotation recovery of the blend of the hard and the soft ores at different grinding time**

Hard ore (1,2,3)/Soft ore (4,5,6)		Recovery (%) (Grinding Time based on hard ore)	Recovery (%) (Grinding Time based on soft ore)	Recovery (%) (Grinding Time based on the average)
1. Argillite (H)	4. DTT (S)	79.0	76.3	65.4
2. Siltstone (H)	4. DTT (S)	78.9	70.1	63.0
3. GTT (H)	4. DTT (S)	81.5	77.0	63.7
1. Argillite (H)	6. Green Garnet (S)	95.3	84.3	94.0
2. Siltstone (H)	6. Green Garnet (S)	95.4	83.6	92.7
3. GTT (H)	6. Green Garnet (S)	84.9	68.8	80.1
1. Argillite (H)	5. Marble (S)	88.2	73.8	75.9
2. Siltstone (H)	5. Marble (S)	85.6	58.8	73.0
3. GTT (H)	5. Marble (S)	86.4	75.2	79.1
<i>Average recovery(%)</i>		<b>86.1</b>	<b>74.2</b>	<b>76.3</b>

In Table D3, the recovery change of blended ores in accordance with changing ore grinding time is investigated. It is shown that the average recovery increases with increasing grinding time. It means that 'incomplete liberation' rather than 'overgrinding' has a more pronounced impact on the flotation recovery. This is quite true because coarse grinding is usually preferred when the ore grade is low in order to achieve a high throughput. In the present study, the criterion of 35% above 100 mesh for the determination of grinding time actually results in a coarse grinding.

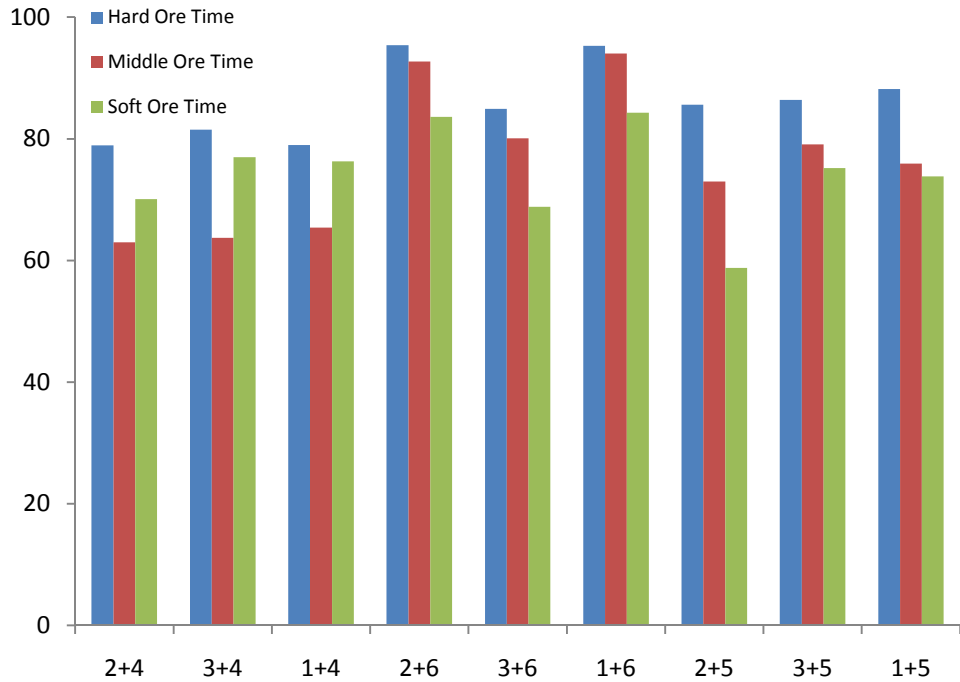


**Figure D5. The flotation recovery as changing grinding time and ore blending mixture**

In Figure D5, except the first three mixtures with the problematic ore #4 (DTT), the grinding time increases with the flotation recovery. Therefore, it clearly shows that when hard and soft ores are mixed, applying the grinding time based on the hard ore is more beneficial on increasing flotation recovery than other grinding time options due to the predominant impact of “incomplete liberation” of hard ores.

In addition, blending the classified rock samples, “Hard/Hard ores” and “Soft/Soft ores,” is conducted and flotation recovery with average grinding time is investigated as shown in Table D4. The average grinding time is used here since it is assumed as the proper

grinding time for this classified ore mixture due to the relatively small change from ore to ore after classification.

**Table D4. Blending effect of classified ores on the flotation recovery**

(Hard + Hard) & (Soft + Soft)	Recovery % (using the average grinding time)
2. Siltstone (H) + 3. GTT (H)	82.6
2. Siltstone (H) + 1. Argillite (H)	77.8
3. GTT (H) + 1. Argillite (H)	84.4
4. DTT (S) + 6. Green Garnet (S)	87.0
4. DTT (S) + 5. Marble (S)	75.2
6. Green Garnet (S) + 5. Marble (S)	87.4
<i>Average recovery(%)</i>	<b>82.4</b>

In Table D4, the average recovery is 82.4% and the value is smaller than 86.1%, which is obtained with the unclassified blending with the hard ores grinding time as shown in Table D3. The results show that the classified rock blending based on the ore hardness actually does not improve the recovery significantly due to the relatively coarse grinding applied in the present study.

### D3.2 Blending Effect of Minerals

Further investigation is conducted to study the “blending effect” and the harmony of ores. It is noted that, from the above experiment results, hard ores grinding time is used for the mixture of hard and soft ores, and the average grinding time is used for classified rock blends, 'Hard/Hard' and 'Soft/Soft' ores. Table D5 shows the test results of blending two out of six ores without applying the strategy considering blending effect or the harmony of ores.

**Table D5. Blending two of six ores without considering hardness and grindability.**

Ore Types	(1)Argillite	(2)Siltstone	(3)GTT	(4)DTT	(5)Marble	(6)Green Garnet	Average
(1)Argillite		77.8	84.4	79.0	88.2	95.3	<b>84.9</b>
(2)Siltstone	77.8		82.6	78.9	85.6	95.4	<b>84.1</b>
(3)GTT	84.4	82.6		81.5	86.4	84.9	<b>84.0</b>
(4)DTT	79.0	78.9	81.5		75.2	87.0	<b>80.3</b>
(5)Marble	88.2	85.6	86.4	75.2		87.4	<b>84.6</b>
(6)Green Garnet	95.3	95.4	84.9	87.0	87.4		<b>90.0</b>

In addition, three kinds of blending effects on the recovery are investigated and compared with each other in Table D6: recovery before blending, recovery of blends without strategy, and recovery of blends with strategy of harmony. The recovery of blending without strategy, the average recovery (%) of each rock type, is obtained from Table D5.

**Table D6. Recovery changes without blending, with blending and with blending strategically**

Rock Types	Classification	Recovery % (without blending)	Recovery % (Blending without strategy)	Recovery % (Blending with strategy)
(1) Argillite	hard ore	86.9	84.9	95.3 (with #6 Sample)
(2) Siltstone		72.2	84.1	95.4 (with #6 Sample)
(3) GTT		69.9	84.0	86.4 (with #5 Sample)
(4) DTT	soft ore	68.2	80.3	87.0 (with #6 Sample)
(5) Marble		87.0	84.6	88.2 (with #1 Sample)
(6) Green Garnet		89.8	90.0	95.4 (with #2 Sample)
<b>Average</b>		<b>79.0</b>	<b>84.7</b>	<b>91.3</b>

The fifth column in Table D6 shows the best possible recovery if there is a chance to use the best harmony of ores, which is blended by considering the testing results in Table D5. For example, for #1 (Argillite), the best recovery can be obtained with blending with #6 Green Garnet as shown in Table D5. Thus, the recovery of the best recovery for #1 Argillite is 95.3% and the number is listed in Table D6.

It is clearly shown that 95.3% is significantly higher than the arithmetical average recovery, 88.4%, for #1 Argillite (86.9%) and #6 Green Garnet (89.8%) without blending. Further explanation and comparison is shown in Table D7.

As shown in Table D6, the average recovery of six ores without blending is 79%. It is also noted that the proper grinding time at each rock type is applied in this case. Thus, there is not much effect of either “incomplete liberation” or “overgrinding.” On the other hand, although there might be the effects of incomplete liberation and overgrinding which decrease the recovery, except of argillite and marble, all recoveries of the four ores are increased after blending, and the average recovery is 84.7%, which is 5.7% higher than the recovery obtained without blending. Furthermore, by utilizing the optimized mixture of ores, the possible maximum average recovery, blending with strategy and considering the harmony, is 91.3%. Compared with the recovery before blending, the increase of 12.3% in metal recovery is quite high.

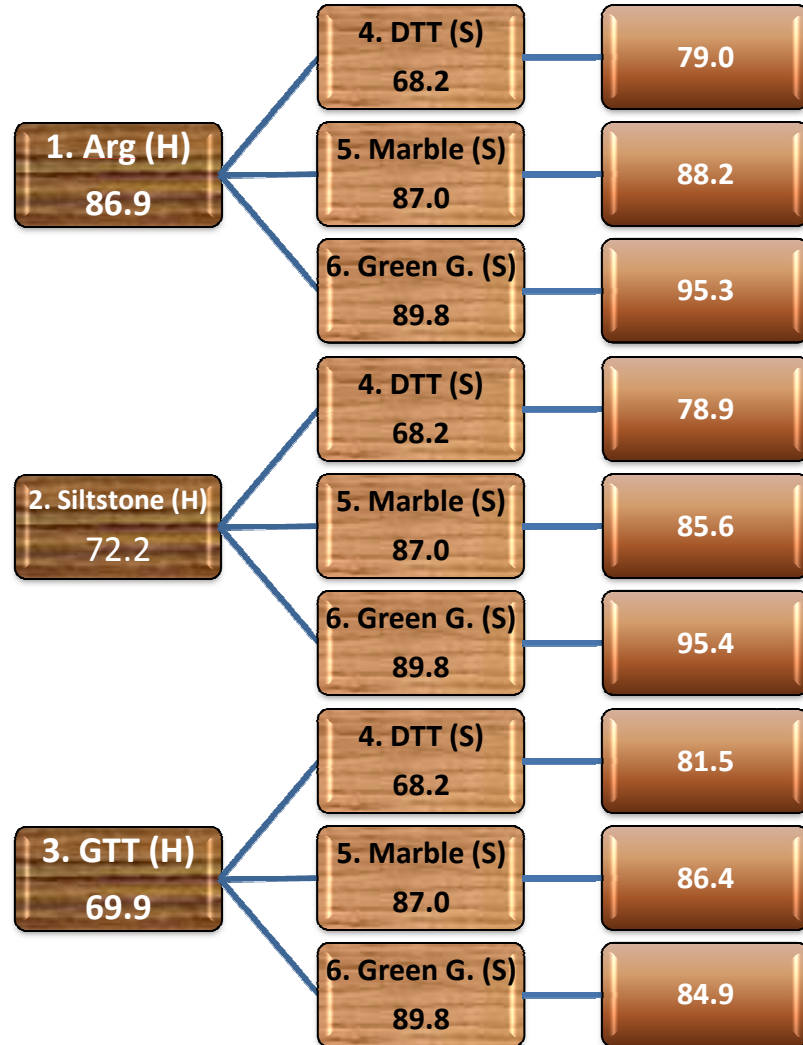


**Figure D6. The blends of hard and soft ores**

In order to study the harmony of ores blend in detail, Figure D6 shows the recovery percentage (%) of blending with hard (#1,2,3) and soft (#4,5,6) ores. In practice, if ores could be mixed with this detailed strategy, then the testing results in Figure D6 might be very useful and applicable, and a better recovery could be obtained. For instance, for the

problematic ore, #4 DTT (which has the lowest recovery before blending), #3 GTT can be the best harmony, highest recovery. As shown in Figure D6, the recovery of GTT and DTT is 69.9% and 68.2% at each, but the recovery is 81.5% after blending. That is a significant increase, 12.5% higher than the arithmetic mean, which is 69.1%. In addition, the best recovery, i.e., 95.3%, is obtained with blending #1 Argillite with #6 Green Garnet. Therefore, when one mix the ores in hard rock mines, blending with strategy can in fact increase the recovery.

Moreover, this harmony can increase the recovery of the problematic ore, such as DTT, instead of diluting it with water and decreasing the total throughput. Thus, this blending effect can be utilized when ores are blended for the target ore grade or for diluting the problematic ores using another ore instead of using water. That is, ores blending can be used in practice to dilute the problematic ores without decreasing the throughput.

Table D7 summarizes the arithmetical average recovery and the recovery of actual blending test result for comparison to show the blending effect. From the table, one can see that although ore blending is generally applied to keep the target ore grade constant, the strategy can actually increases the metal recovery, which is higher than the arithmetical average of both ores. That is, the actual blended ore recoveries are always higher than all the arithmetic mean recoveries. The difference ranges from 1.3% to 14.4%.

**Table D7. The recovery of arithmetic mean and the actual recovery using blending effect**

<b>Blending Ore Types</b>	<b>Recovery (%) Arithmetic Means</b>	<b>Recovery (%) With blending</b>	<b>Difference (%)</b>
<b>1+4</b>	77.6	79.0	+1.4
<b>1+5</b>	87.0	88.2	+1.3
<b>1+6</b>	88.4	95.3	+7.0
<b>2+4</b>	70.2	78.9	+8.7
<b>2+5</b>	79.6	85.6	+6.0
<b>2+6</b>	81.0	95.4	+14.4
<b>3+4</b>	69.1	81.5	+12.5
<b>3+5</b>	78.5	86.4	+8.0
<b>3+6</b>	79.9	84.9	+5.1
<b>Average</b>	<b>79.0</b>	<b>86.1</b>	<b>+7.1</b>

#### **D4. Discussion and Future Studies**

As the part of the study of finding the target blast fragmentation, the effect of blending ores is investigated. As in other researchers' studies [1, 2, 9], it is initially predicted that classifying rock types could be a solution to reduce the effect of both the overginding of soft ores and the incomplete liberation of hard ores, and this classification based on ore hardness might be helpful to increase the flotation recovery.

At first, the grinding time effect, i.e. product size effect from the grinding circuit, on the flotation recovery of the mixture of two different ores is investigated with three kinds of grinding times: (1) grinding time based on hard ores, (2) grinding time based on soft ores, and (3) average grinding time. In this study, it is concluded that the effect of "incomplete liberation" is predominant in the decrease of the recovery rather than "overgrinding" as the average recovery increases with increasing the grinding time. Therefore, "incomplete

“liberation” of the hard ores in grinding blended ores should be avoided for a better recovery especially in a coarse grinding. In addition, it is found that the classified rock blending does not in fact improve the recovery much.

The “blending effect” and the optimum harmony of ores are studied further. Various blending cases are tested and the average recoveries are compared. The average recovery of six ores before blending is 79%; the one after blending is 84.7%, and one with utilizing the best blending harmony is 91.3%. Therefore, the possible average increase is 5.7% after blending, and the maximum increase could be 12.3% from mixing ores by considering the best harmony of two ores. In particular, all the recoveries of actually blending two ores are higher than all the arithmetic mean recoveries. It is therefore concluded that this is the “Blending Effect” which has a positive impact on the flotation recovery.

Furthermore, instead of diluting the problematic ores with water in practice, the “blending effect” can be the solution of problematic ores such as DTT here. In this study, the recovery of GTT and DTT was 69.9% and 68.2% respectively, and the actual recovery after blending these two ores was 81.5%, which is significantly higher than the arithmetic mean, 69.1%.

Based on the studies here, in practice, the blending strategy considering the harmony can be utilized in a hard rock mine, and this strategy can increase the flotation recovery. For

instance, to improve the flotation recovery, building stockpiles separately by considering the rock hardness and grindability can be beneficial and blending with strategy has to make allowance for not only hardness but also the blending effect.

It is also concluded that blending harmony needs to be considered rather than just hardness when finding the target blast fragmentation (P80) at each rock type by considering the whole processes which includes blasting (blastability), loading, hauling, crushing, grinding and flotation. For example, for argillite, the best flotation recovery, 95.3%, can be obtained with green garnet. Nonetheless, grindability and proper grinding time for the grinding circuit are completely different. In this case, higher blast energy, the drill and blast cost increases, on argillite can be helpful and more efficient because as blasting energy is applied more on the hard ore, Bond Work Index can be reduced by inducing preconditioned micro-cracks. Thus, although more expense in blasting will increase the budget in the mine department, it will surely decrease the mill processing cost and increase productivity, throughput and flotation recovery.

There may be some difficulties in applying the blending effect into the actual mineral processing; however, it is realized that there could be a huge potential increase in metal recovery if we understand and utilize the blending effect correctly. In addition, the better flotation recovery of the problematic ore is expected by using the blending effect. Further studies are needed for this purpose in the future study.

## References

- [1] Kim, S. J., 2010, An Experimental Investigation of the Effect of Blasting on the Impact Breakage of Rocks, *Master of Applied Science thesis, The Robert M. Buchan Department of Mining, Queen's University, Kingston, Canada*
- [2] Nielsen, K., Malvik, T., 1999, Grindability enhancement by blast-induced microcracks, *Powder Technology 105, pp 52-56.*
- [3] Bustamante, H. and Warren, L.J., 1984. The Joint Effect of Rank and Grain Size on The Flotation of Australian Bituminous Coals, *Int. J. Miner. Process., Vol. 13, PP.13-28*
- [4] Trahar, W. J., 1981, A rational Interpretation of the Role of Particle Size in Flotation, *Int. J. Miner. Process., Vol. 8, PP.289-327*
- [5] Hernainz, F. and Calero, M., 2001. The Effect of the Degree of Grinding on the Flotation of Celestite Ore, *Advanced Powder Technol., Vol. 12, No. 4, PP. 481-491*
- [6] Kim, K.M., 2006, Blasting design using fracture toughness and image analysis of the bench face and muckpile, *Master of Science thesis, Mining and Mineral Engineering, Virginia Tech, Blacksburg, USA*
- [7] Kim, K.M. and Kemeny, John, 2011, “Site Specific Blasting Model Using Schmidt Tensile Strength and Image Analysis”, *International Society of Explosives Engineers (ISEE), San Diego*
- [8] Kim, K.M. and Kemeny, John, 2011 “Site Specific Blasting Model for Mine-to-Mill Optimization”, *Transactions of the Society for Mining, Metallurgy and Engineering, Vol.330.*

[9] Yusupov, T.S., Kirillova, E.A., and Shumskaya, 2007, Mineral Hardness Effect on The Combined Mineral Grinding, *Journal of Mining Science*, Vol. 43, No. 4